ON THE PROPAGATION OF FREE TOPOGRAPHIC ROSSBY WAVES NEAR CONTINENTAL MARGINS

by

HSIEN WANG OU

B.S., National Tsing Hua University in Taiwan (1971)

M.S., Florida State University (1975)

SUBMITTED IN PARTIAL FULFILLMENT OF THE

REQUIREMENTS FOR THE DEGREE OF

DOCTOR OF PHILOSOPHY

at the

MASSACHUSETTS INSTITUTE OF TECHNOLOGY

and the

WOODS HOLE OCEANOGRAPHIC INSTITUTION

April, 1979

Signature of Author ______________________________
Joint Program in Oceanography, Massachusetts Institute of Technology - Woods Hole Oceanographic Institution, and Department of Earth and Planetary Sciences, and Department of Meteorology, Massachusetts Institute of Technology, April, 1979.

Certified by ______________________________
Thesis Supervisor

Acccepted by ______________________________
Chairman, Joint Oceanography Committee in Earth Sciences, Massachusetts Institute of Technology - Woods Hole Oceanographic Institution.

ON THE PROPAGATION OF FREE TOPOGRAPHIC ROSSBY WAVES NEAR CONTINENTAL MARGINS

by

Hsien Wang Ou

Submitted to the Massachusetts Institute of Technology
Woods Hole Oceanographic Institution
Joint Program in Oceanography on April 29, 1979,
in partial fulfillment of the requirements for
the degree of Doctor of Philosophy

ABSTRACT

Observational work by Thompson (1977) and others has demonstrated that free topographic Rossby waves propagate northward up the continental rise south of New England. To study the dynamical implications of these waves as they approach the shelf, Beardsley, Vermersch, and Brown conducted an experiment in 1976 (called NESS76) in which some moored instruments were strategically placed across the New England continental margin to measure current, temperature, and bottom pressure for about six months.

An analytical model has been constructed to study the propagation of free topographic Rossby waves in an infinite wedge filled with a uniformly stratified fluid. The problem is found after some coordinate transformations to be identical to the corresponding surface gravity wave problem in a homogeneous fluid, but with the roles of the surface and bottom boundaries interchanged. Analytical solutions are thus available for both progressive and trapped waves, forming continuous and discrete spectra in the frequency space. The separation occurs at a nondimensional frequency $\sigma = S$, defined as $(N/f) \tan\theta^*$, where N and f are the Brunt-Väisälä and inertial frequencies, and $\tan\theta^*$ is the bottom slope. Since an infinite wedge has no intrinsic length scales, the only relevant nondimensional parameters are the frequency σ and the Burger number S. Thus, stratification and bottom slope play the same dynamical role, and the analysis is greatly simplified. Asymptotic solutions for the progressive waves have been obtained for both the far field and small S which enable us to examine the parameter dependence of some of the basic wave properties in the far field, and the spatial evolution of the wave amplitude and phase as they approach the apex when S is small. The general solution is then presented and discussed in some detail. The eigenfrequencies of the trapped modes decrease when S decreases and reduce to the short wave limit of Reid's (1958) second class, barotropic edge waves when S approaches zero. The modal structure broadens as S increases to some critical value above which no such coastally-trapped modes exist.

To simulate more closely the dynamical processes occurring near the continental margin, a numerical model incorporating a more realistic topography than an infinite wedge has been constructed. With stratification imposing an additional barrier, the model suggests that the maximum energy flux transmission coefficient obtained in Kroll and Niiler's barotropic model (1976) is likely an upper bound. Also in the presence of the finite slope changes, the baroclinic fringe waves generated near the slope-rise junction may form an amphidromic point at some mid-depth and locally reverse the direction of the phase propagation above it. These baroclinic fringe waves also cause an offshore heat flux over the continental rise which, combined with the onshore heat flux generated over the slope region in a frictionless model, induces, across the transect, a mean flow pattern of two counter-rotating gyres with downwelling occurring near the slope-rise junction. Bottom friction always generates an offshore heat flux and therefore modifies this mean flow pattern over the slope region. The induced longshore mean flow is approximately geostrophically balanced and generally points to the left facing the shoreline, but its direction can be reversed where the baroclinic fringe waves dominate. The mean thermal wind relation implies a generally denser slope water than that farther offshore.

Some of the model predictions are compared with the data taken from NESS76. The comparisons are generally consistent, suggesting that topographic Rossby wave dynamics may play an important role for the low frequency motions near continental margins.

Thesis Supervisor: Robert C. Beardsley

Title: Associate Scientist
Woods Hole Oceanographic Institution

ACKNOWLEDGMENTS

I would like to thank my thesis advisor, Robert C. Beardsley, for his support and guidance throughout this work, and the members of my thesis committee, Peter Rhines, Nelson Hogg, and Glenn Flierl for many helpful discussions. I would also like to thank Doris Haight for typing the manuscript.

This work is supported at Woods Hole Oceanographic Institution by the National Science Foundation under grant numbers OCE 76-01813 and OCE 78-19513.

TABLE OF CONTENTS

1. Introduction

There have been considerable efforts (e.g., Thompson, 1971; Rhines, 1971; Thompson and Luyten, 1976) looking for clues of bottom intensified topographic Rossby waves since they are first proposed in theory by Rhines (1970). Recently, after an extensive analysis of the data obtained near site D (39°10'N, 70°W), Thompson (1977) concluded that there is strong evidence that the low frequency motions below the thermocline over the continental rise north of the Gulf Stream are dominated by linear topographic Rossby wave dynamics. Furthermore, the observed offshore phase propagation is consistent with the assumption that these waves are generated offshore and radiate their energy shoreward onto the coast. Questions naturally arise: What's the behavior of these waves as they approach the coast, especially over the rapid transition region between the continental rise and the slope? Would they be able to penetrate through the topographic barriers and contribute significantly to the motions on the shelf? To answer the first question, Suarez (1971) studied the effect of small slope changes on the impinging Rossby waves. He found that in a stratified ocean, baroclinic fringe waves are excited near the slope discontinuity and impose an additional barrier to the transmission of the waves. The slope discontinuity, in his own words, "therefore acts like an elastic membrane yielding under the influence of the impinging Rossby waves but springing back with little energy lost". To answer the second question, Kroll and Niiler (1976) constructed an analytical model which considers the propagation of topographic Rossby waves in a barotropic ocean of exponentially varying bottoms. With reasonable friction included, they concluded that these waves are likely to be completely decayed when the bottom depth is less than 25 m. As the slope change is not small near continental margins and the ocean is not homogeneous, a numerical model incorporating both effects has been constructed here to give a more complete picture about the dynamical processes occurring near continental margins.

To help understand the numerical results, an analytical model is first presented in Chapter 2, which considers the propagation of topographic Rossby waves in a wedge filled with a uniformly stratified fluid. This is, in some sense, a generalization of Rhines' (1970) solution of a bottom-trapped edge wave in an infinitely deep ocean of finite bottom slope, and his solution of a quasi-geostrophic wave in a finite depth ocean but with an infinitesimal bottom slope. The problem is found after some coordinate transformations to be identical to the corresponding surface gravity wave problem in a homogeneous fluid, but with the roles of the surface and bottom boundaries interchanged. Analytical solutions by Peters (1952) and Ursell (1952) are therefore applicable to our problem for the progressive and trapped waves, forming respectively continuous and discrete spectra in frequency space. The separation occurs at a nondimensional frequency δ = S, defined as $(N/f)\tan\theta^*$, where N and f are the Brunt-Väisälä and inertial frequencies and $\tan\theta^*$ is the bottom slope. The wave frequency has been nondimensionalized by f. Asymptotic solutions for the progressive waves are first obtained for both the far field and small S which enable us to examine the parameter dependence of some of the basic wave properties in the far field and the spatial evolution of the wave amplitude and phase as these waves approach the apex when S is small. The general solutions for the progressive and the trapped waves are then presented and discussed in some detail. This is followed by a summary of the major results of the analytical model.

In Chapter 3, a numerical model incorporating a more realistic topography and the frictional effect is constructed to simulate more closely the dynamical processes occurring near continental margins. To simplify the interpretations of the results and for easier comparison with other existing models, the stratification is assumed uniform and the topography is assumed to be comprised of three sections of exponentially varying bottom, corresponding roughly to the continental rise, slope, and shelf. These restrictions can be easily relaxed in the model. The model is similar to that of Wang (1975, 1976), except radiation conditions are imposed at both the inshore and offshore boundaries of the transect and an Ekman suction velocity is included in the bottom boundary condition to simulate the effect of friction. With incoming waves specified at some offshore location on the continental rise, we can then study the evolution of these waves as they approach the coast. We will present the inviscid solution for a typical oceanic case and discuss its properties in some detail. Most of the results can be interpreted by the analytical solution in a wedge, but the replacement of the apex by a finite shelf and the rapid slope change across the slope-rise junction introduce some additional features that modify the wave properties considerably. Some simple results assuming quasi-geostrophy are derived to help explain these new features. A brief discussion on the parameter dependence of the solution as well as the frictional effect on these waves is then presented. The chapter concludes with a summary of the major predictions of the model.

In Chapter 4, some of the model predictions are compared with the observations taken from an experiment conducted by Beardsley, Vermersch, and Brown in 1976, called NESS76, in which some moored instruments were strategically placed across the New England continental margin to measure current, temperature, and bottom pressure for about six months. Detailed analysis of the data will be presented elsewhere (Beardsley, Ou, and Brown, in preparation) and only some relevant observations will be shown here to compare with the model. Based on this comparison, the validity of the model and its further applications are discussed briefly at the end of the chapter.

2. Analytical Model of Free Topographic Rossby Waves in a Wedge

2.1 The Formulation of the Model

Let's consider free topographic Rossby waves in a wedge filled with a uniformly stratified fluid, as shown in Fig. 2.1. The linearized equations for an inviscid, hydrostatic and Boussinesque fluid are given by,

$$
\begin{aligned}
u_t - fv &= -p_x, \\
v_t + fu &= -p_y, \\
0 &= -p_z - \rho g, \\
u_x + v_y + w_z &= 0, \\
\rho_t - \frac{N^2}{g} w &= 0,
\end{aligned}
\qquad (2.1)
$$

where all the notations have their conventional meanings. Boundary conditions for the rigid surface and impenetrable bottom are

$$w = 0 \qquad \text{at } z = 0,$$

and (2.2)

$$w = -v \tan\theta^* \qquad \text{at } z = -y \tan\theta^*.$$

Nondimsionalized by the following scalings,

$$
\begin{aligned}
(x,y,z) &\rightarrow L(x,y,z \tan\theta^*), \\
(u,v,w) &\rightarrow V(u,v,w \tan\theta^*), \\
t &\rightarrow f^{-1} t, \\
p &\rightarrow (fVL)p, \\
\rho &\rightarrow \left(\frac{fV}{g \tan\theta^*}\right)\rho,
\end{aligned}
\qquad (2.3)
$$

where V is the velocity scale and L can be any length scale, the governing equations become

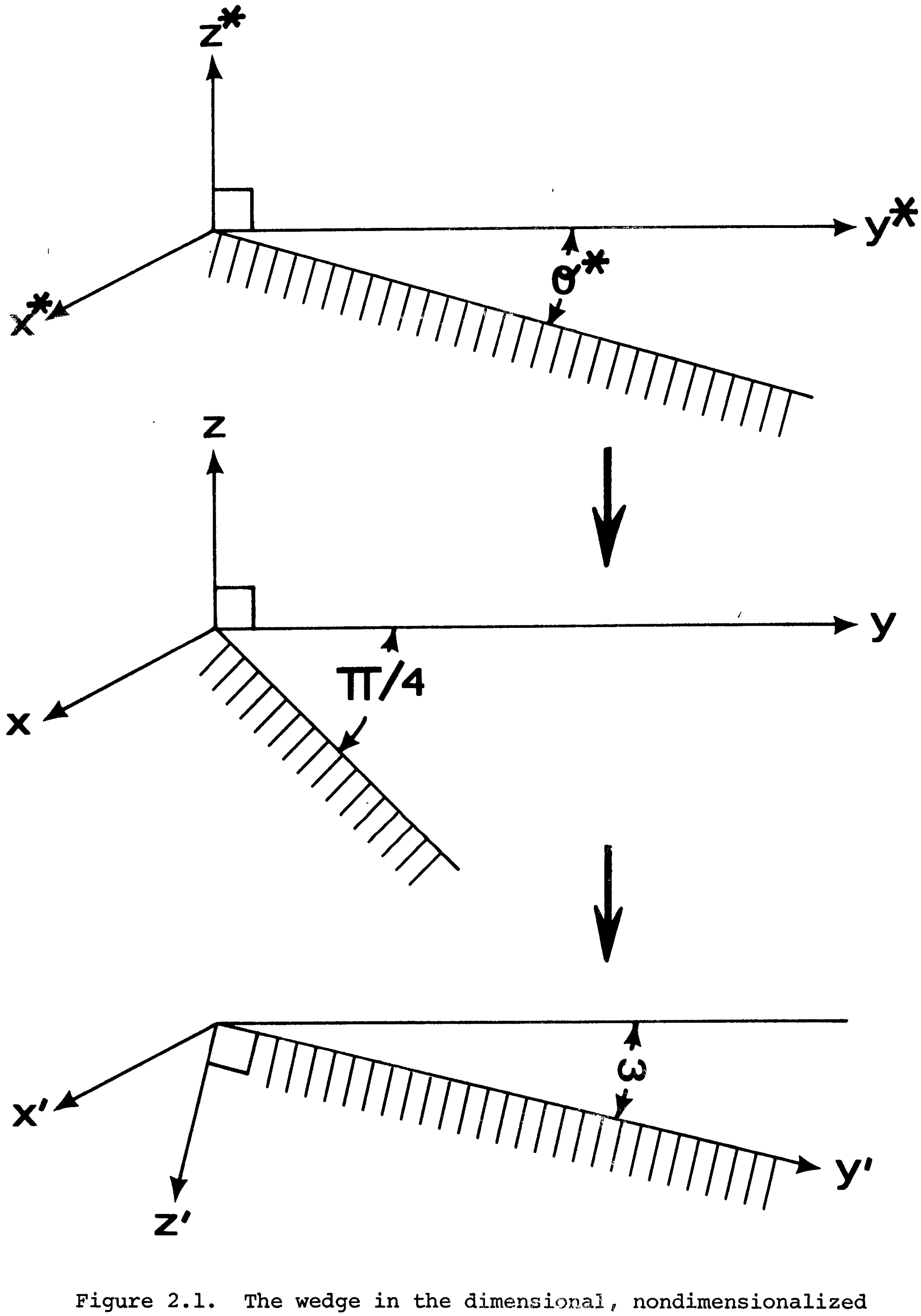

Figure 2.1. The wedge in the dimensional, nondimensionalized and the transformed space.

$$
\begin{aligned}
u_t - v &= -p_x,\\
v_t + u &= -p_y,\\
0 &= -p_z - \rho,\\
u_x + v_y + w_z &= 0,\\
\rho_t - S^2 w &= 0,
\end{aligned}
\tag{2.4}
$$

with the boundary conditions

$$w = 0 \qquad \text{at } z = 0,$$

and (2.5)

$$w = -v \qquad \text{at } z = -y,$$

where $S \equiv (N/f)\tan\theta^*$ is the Burger number. Notice that the bottom slope $\tan\theta^*$ has been scaled to unity, and its magnitude incorporated with the stratification into a single parameter S.

Solutions of the form

$$p \sim p(y,z)e^{i(kx-\sigma t)} \tag{2.6}$$

exist provided p satisfies the reduced equation

$$p_{yy} - k^2 p + \frac{1-\sigma^2}{S^2}p_{zz} = 0, \tag{2.7}$$

with the boundary conditions

$$p_z = 0 \qquad \text{at } z = 0, \tag{2.8}$$

$$p_z = -\frac{S^2}{1-\sigma^2}\left(p_y + \frac{k}{\sigma}p\right) \qquad \text{at } z = -y. \tag{2.9}$$

Since an infinite wedge has no intrinsic length scales, the only relevant parameters are the nondimensional wave frequency σ and the Burger number S. Hence, stratification and bottom slope play the same dynamical role and the analysis is greatly simplified.

By mapping this wedge of unit slope into a wedge of slope $\tan\omega$ through the transformations (Fig. 2.1)

$$x' = \frac{k}{k'}\, x,$$
$$y' = \frac{k\cos\omega}{k'}(y - z\tan\omega^2), \qquad (2.10)$$
$$z' = -\frac{k\sin\omega}{k'}(y + z),$$

where

$$k' = \sigma / \sin\omega, \qquad (2.11)$$

and

$$\tan\omega = \frac{\beta}{\sqrt{1-\sigma^2}}, \qquad (2.12)$$

the equations (2.7) through (2.9) can be further reduced to,

$$p_{y'y'} + p_{z'z'} - k'^2 p = 0, \qquad (2.13)$$
$$p_n = 0 \qquad \text{at } z' = -\, y' \tan\omega, \qquad (2.14)$$
$$p_{z'} = p \qquad \text{at } z' = 0, \qquad (2.15)$$

where the subscript n represents the normal derivative. These equations are identical in form to the equations satisfied by the velocity potential of an inviscid, irrotational surface gravity wave in a homogeneous fluid (e.g., Stoker, 1957), with the roles of the surface and bottom boundaries interchanged. The solutions by Peters (1952) and Ursell (1952) for the progressive and trapped waves are therefore applicable.

In Fig. 2.1, the x', y', and z'-axis are drawn for the case $k/k' > 0$. The case $k/k' < 0$ is excluded for the bottom-trapped waves since it is clear from (2.15) that z' must be negative in the wedge for these waves. Since $k/k' > 0$ implies a positive σ/k, these waves have their wave crests propagating to the left facing the apex.

Since in the far field, the solution is approximately given by

$$p = \overline{p}(y')e^{z'},$$

where $\overline{p}$ satisfies

$$\overline{p}_{y'y'} + (1 - k'^2)\overline{p} = 0,$$

these waves can propagate in y' only when

$$|k'| \leq 1,$$

which can be shown, from (2.11) and (2.12), to be equivalent to

$$|\sigma| \leq S. \tag{2.16}$$

Since the buoyancy force is the only restoring mechanism in the far field, this is similar to the short wave cut-off frequency Rhines (1970) found for the bottom-trapped edge waves in an infinitely deep ocean. This cut-off frequency divides the (S,σ) space into two regions (Fig. 2.2); one region in which waves are progressive in y' and the frequency takes on continuous values, and the other region in which waves are trapped in y' and the frequency is allowed to have only discrete values. Solutions for both regions will be presented but with more emphasis on the progressive waves as they can propagate into the shallower water from the deep ocean and hence are more pertinent to our study of the dynamical coupling of the motions across continental margins.

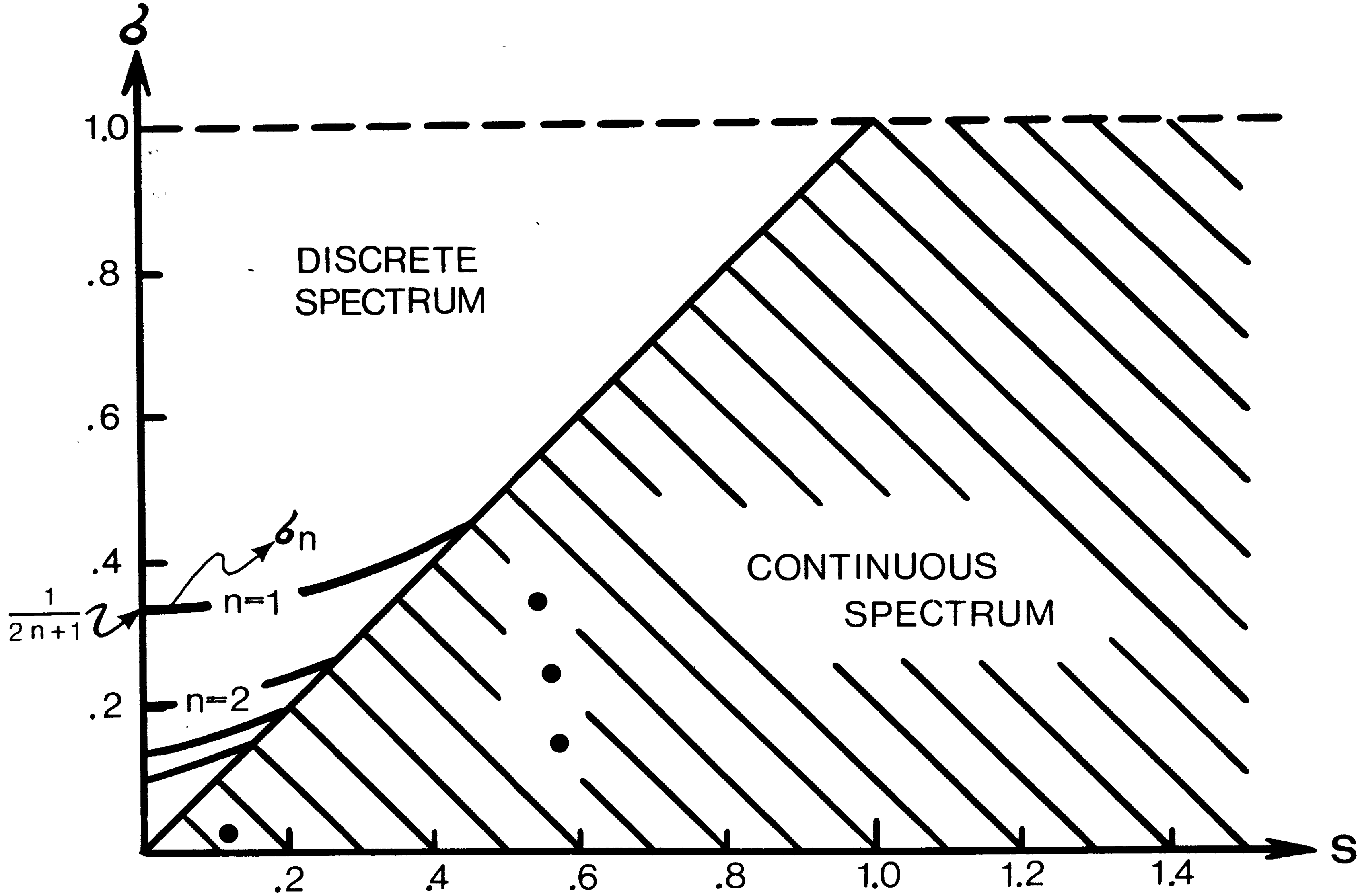

Figure 2.2. Separation of (S,σ) space into the regions of continuous and discrete spectrum by the short wave cut-off. Analytical solution has been evaluated for the cases shown by the solid dots and the eigenfrequencies of the first four trapped modes are shown by the solid curves.

2.2 Continuous Spectrum

The problem of progressive surface gravity waves impinging on a uniformly sloping beach at an arbitrary incidence angle has been solved by Peters (1952). Since we have shown that his problem is mathematically identical to the problem we are considering here, his solutions are directly applicable. The two independent standing wave solutions (corresponding to s = 1 and 2 in the following expressions) are given by some contour integrations on the complex ζ -plane,

$$\chi_s = (i)^s \int_{\Gamma_s} \frac{\zeta\, g(\zeta,\tau_1)\, g(\zeta,\tau_2) \exp(\eta\zeta + \tau_1\tau_2\bar{\eta}/\zeta)\, d\zeta}{(\zeta + i\tau_1)(\zeta + i\tau_2)}, \tag{2.17}$$

where

$$g(\zeta,\tau) = \exp\left\{-\frac{1}{\pi}\int_0^{\infty} \frac{\zeta}{v^2+\zeta^2} \ln\left(\frac{v^{\mu}-\tau^{\mu}}{v^{\mu}}\cdot\frac{v^2}{v^2-\tau^2}\right) dv\right\} \tag{2.18}$$

is defined in the sector $-\pi/2 - 2\omega < \arg\zeta < \pi/2 + 2\omega$ where it is analytic,

$$\begin{aligned} \eta, \bar{\eta} &= y' \pm i z', \\ \tau_1, \tau_2 &= \tfrac{1}{2}\left(1 \pm \sqrt{1-\kappa'^2}\right), \\ \mu &= \pi/\omega, \end{aligned} \tag{2.19}$$

and $\Gamma_1, \Gamma_2 = \Gamma^- \mp \Gamma^+$ are the contours shown in Fig. 2.3.

Since Peters has shown that these two solutions are sinusoidal in y' and $\pi/2$ radians out of phase with each other far away from the apex, they can be combined, with appropriate time and amplitude factors, to yield progressive waves in the far

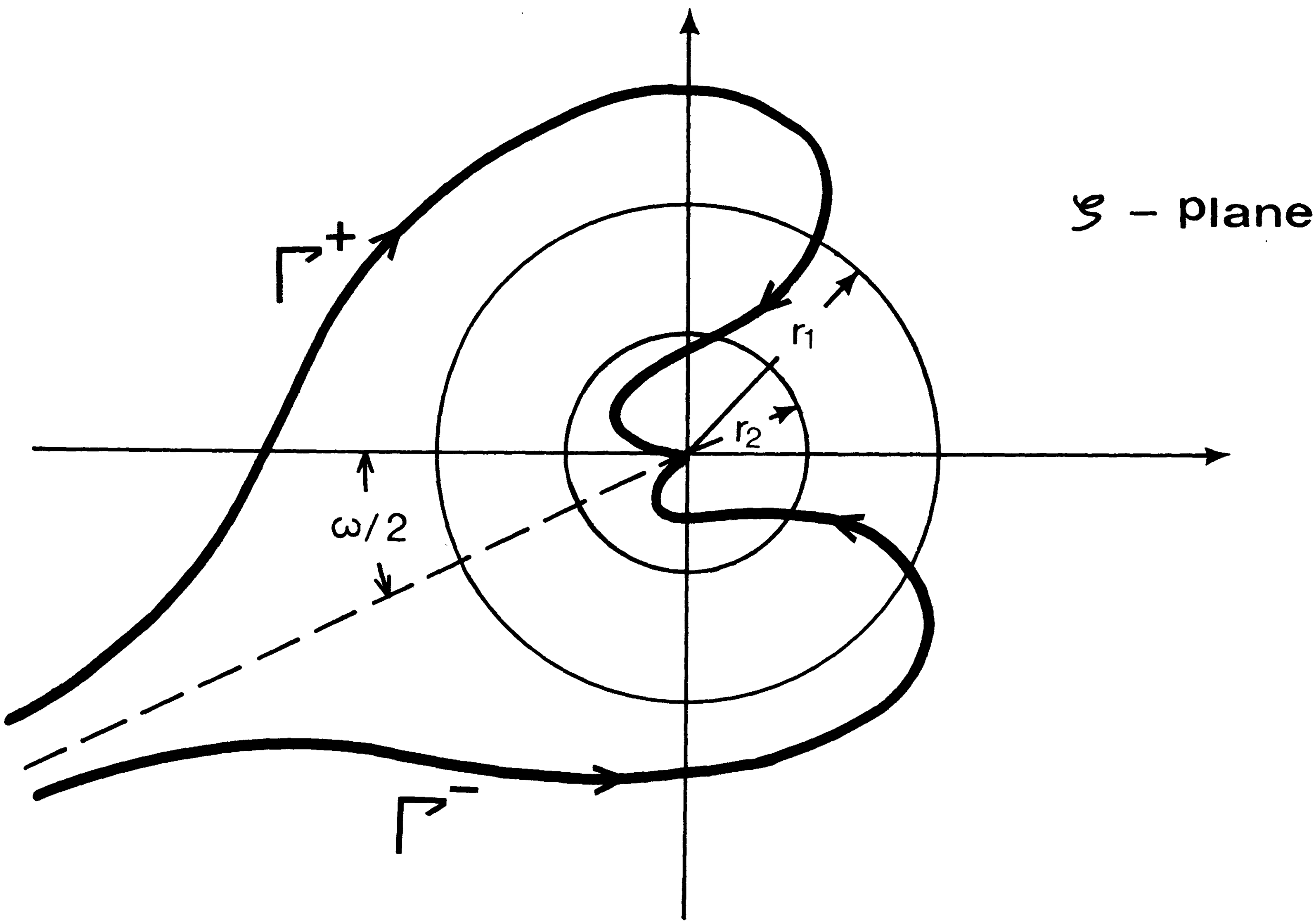

Figure 2.3. The contours of integration for the analytical solution of progressive waves.

field. At the apex, χ_1 remains regular but χ_2 becomes logarithmically singular. The physical basis for this logarithmic singularity has been discussed briefly by Stoker (1957). Basically, if no reflection occurs at the apex, all the incoming energy has to be absorbed there, producing a singular point. This is also where linear wave dynamics breaks down. If, however, total reflection is assumed, then χ_1 would be the solution for motions that are well-behaved at the apex. In a realistic application, the incoming waves are of course neither totally absorbed nor totally reflected at the apex, both solutions might be required for a complete description. There will be more discussion on this pertaining to the particular problem we are considering in the next chapter. Here, we shall only present the propagating wave solution since the behavior of the standing waves away from the apex can be fairly easily inferred from it, and also the phase properties can be more easily visualized.

To help understand the full solution (2.17), we will present next the asymptotic solutions for both the far field and the small S.

2.2.1 Asymptotic Solution in the Far Field

In the far field, where the wave amplitude is negligible near the upper surface, the approximate solution of (2.13) through (2.15) is given by,

$$p = e^{z' + i\sqrt{1-k'^2}\, y'}. \tag{2.20}$$

Transforming back to the (y,z) coordinates according to (2.10), we get

$$p = e^{-\frac{K\sin\omega}{K'}(y+z) + i\sqrt{1-K'^2}\,\frac{K\cos\omega}{K'}(y - z\tan\omega^2)} \tag{2.21}$$

This is a bottom-intensified wave that has amplitude contours parallel with the sloping bottom (i.e., $y + z =$ constant). The phase lines are tilted from the vertical axis and have a slope

$$\begin{aligned} \Gamma &= 1/\tan^2\omega \\ &= \frac{1-\sigma^2}{S^2}, \end{aligned} \tag{2.22}$$

the arctangent of which is plotted in Fig. 2.4. In the dimensional space, this slope is given by

$$\begin{aligned} \Gamma^* &= \Gamma \tan\theta^* \\ &= \frac{f^2\sigma^2}{N^2\tan\theta^*}. \end{aligned} \tag{2.23}$$

Therefore, the phase lines are more vertical for smaller σ, N or θ^*. To get a rough idea of the magnitude of this slope in a typical oceanic case, let's assume that $N = 10^{-3}$ sec^{-1}, $f = 10^{-4}$ sec^{-1}, and $\sigma \ll f$, then $\Gamma^* = 10^{-2}/\tan\theta^*$. When the bottom slope varies from about 10^{-3} on the continental rise to about 5×10^{-2} on the continental slope, the tilting of the phase lines for short waves then varies from about 5° from the vertical over the rise to about 11° from the horizontal plane over the slope.

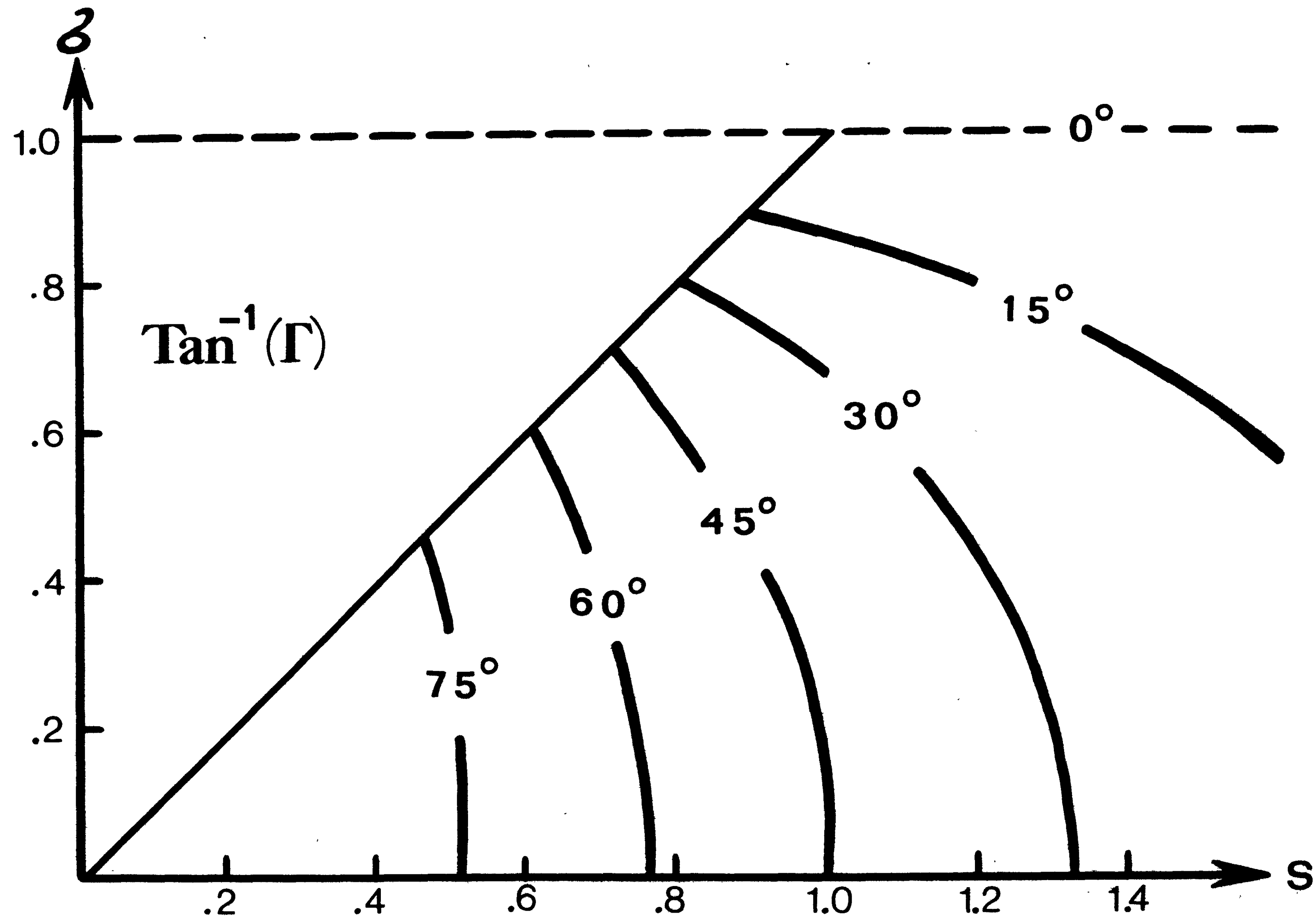

Figure 2.4. Contours of the arctangent of the nondimensionalized phase line slope in the far field.

A crude measure of the intensity of the bottom trapping can be given by the "penetration depth", defined as

$$D^* = \left[\left|\frac{\partial |p|}{\partial z^*}\right| \Big/ |p| \right]^{-1}_{\text{bottom}}, \qquad (2.24)$$

which in the far field leads to,

$$
\begin{aligned}
D^* &= \left[\left|\frac{\partial |p|}{\partial z^*}\right| \Big/ |p|\right]^{-1}_{\text{bottom}} \cdot L\tan\theta^* && \text{(from (2.3))} \\
&= \frac{k'}{k\sin\omega}\cdot L\tan\theta^* && \text{(from (2.21))} \\
&= \frac{\sigma(1+S^2-\sigma^2)}{S^2}\cdot\frac{\tan\theta^*}{k^*} && \text{(from (2.11) and (2.12))} \\
&\equiv D\cdot\frac{\tan\theta^*}{k^*},
\end{aligned}
$$

where

$$D \equiv \frac{\sigma(1+S^2-\sigma^2)}{S^2} \qquad (2.25)$$

is some dimensionless quantity that is plotted in Fig. 2.5. With fixed bottom slope and longshore wavelength, the motions are generally more bottom trapped for smaller σ or larger S. This is because both lowering σ and increasing S tend to increase the amplitude of the density fluctuations for a given onshore velocity or pressure amplitude along the bottom which, through the hydrostatic balance, implies a stronger bottom trapping.

Since in the far field, the frequency can only depend on the direction of the wave number vector but not the magnitude of it, the group velocity must be perpendicular to the phase

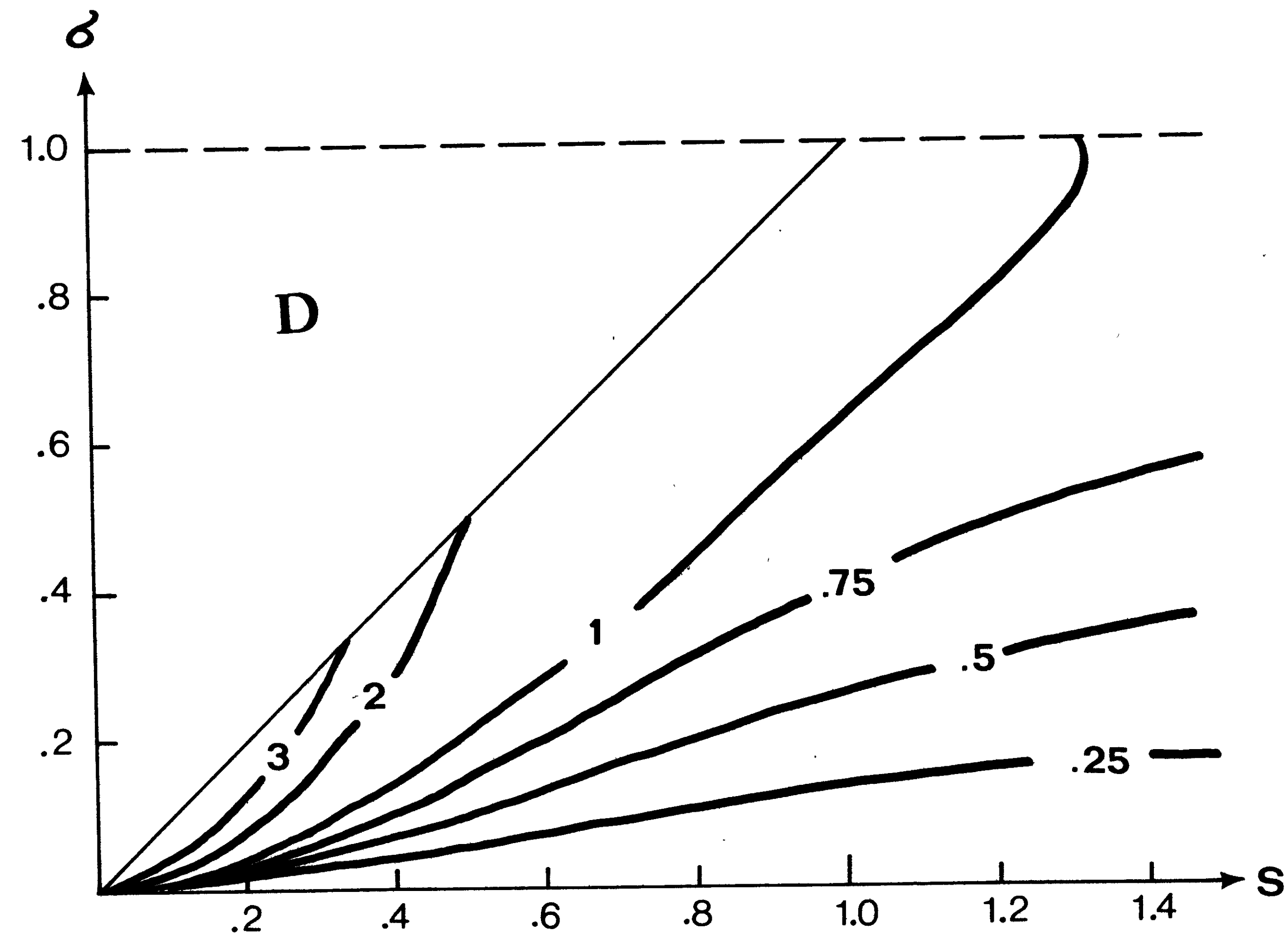

Figure 2.5. Contours of some nondimensionalized "penetration depth" in the far field.

velocity. Given the fact that these waves can only propagate to the left facing the apex as was shown earlier, the wave crests associated with the incident waves must propagate offshore.

Let ϕ be the projection on the horizontal plane, of the angle the wave number vector $\vec{k}$ makes with the shoreline (Fig. 2.6), then the dispersion relation can be easily derived from (2.21),

$$\begin{aligned} \phi &= \tan^{-1}\left\{\frac{K\,\mathrm{arw}}{K'}\cdot\frac{\sqrt{1-K^2}}{K}\right\} \\ &= \tan^{-1}\left\{\frac{\sqrt{S^2-\sigma^2}}{\sigma}\cdot\frac{1-\sigma^2}{1+S^2-\sigma^2}\right\}, \end{aligned} \tag{2.26}$$

which is plotted in Fig. 2.7.

It is seen that the wave number vectors are more parallel to the isobaths for larger σ or smaller S. This is expected, since the fluid particles traverse the isobaths at a more normal angle for these waves, they are hence subjected to a greater restoring force for a given S, and fluctuate more rapidly; or equivalently, with frequency fixed, S has to be smaller for these fluid particles to be subjected to the same restoring force.

Some of the properties of the current ellipse will be derived next where all the superscripts " ' " refer to variables in the transformed coordinate system. Since w' vanishes at z' = 0, and the solution is exponentially decaying in -z', w' vanishes everywhere in the far field so that for a propagating wave with a wave number vector $\vec{k}'$,

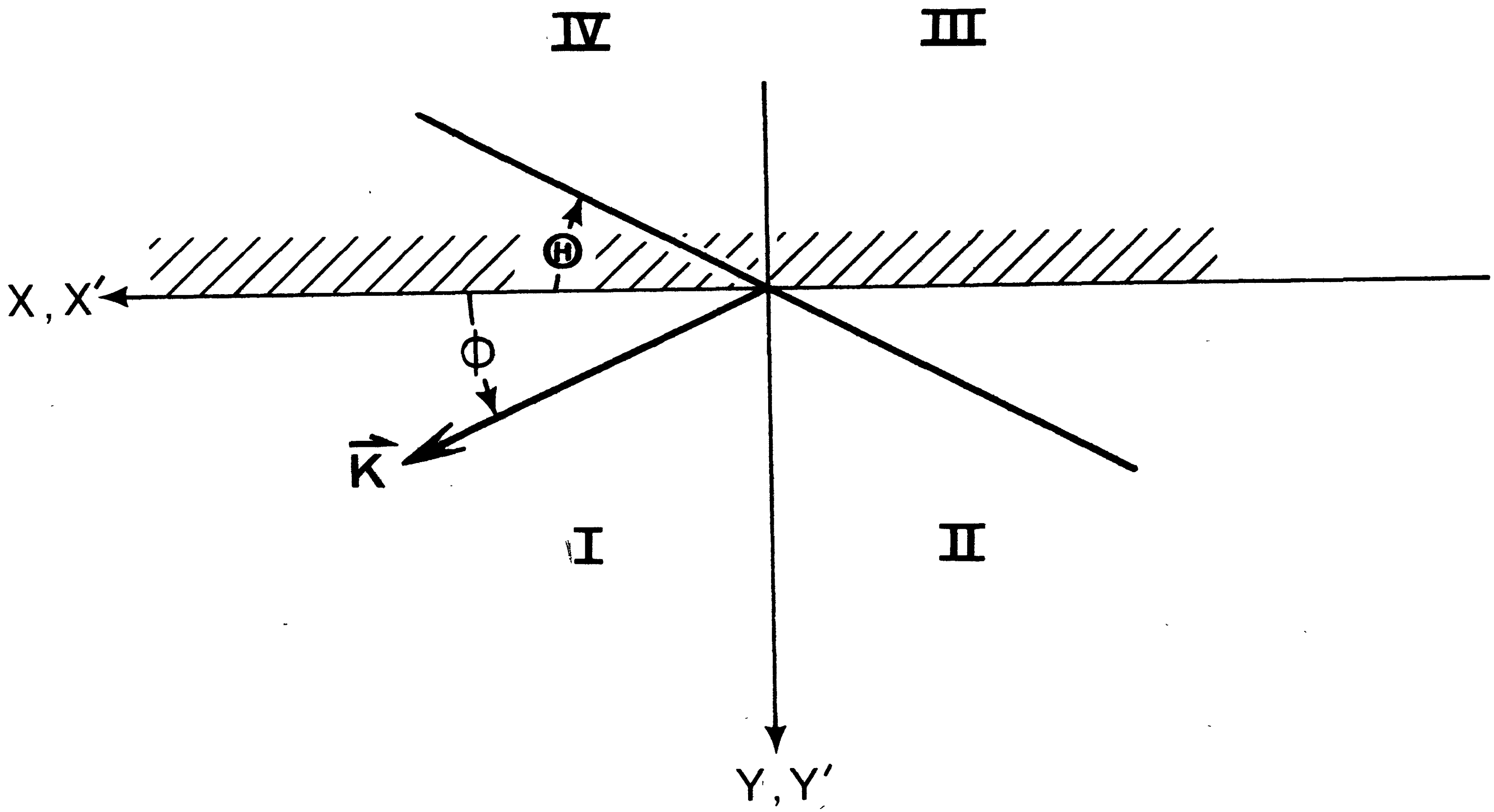

Figure 2.6. Figure showing the definition of ϕ and θ.

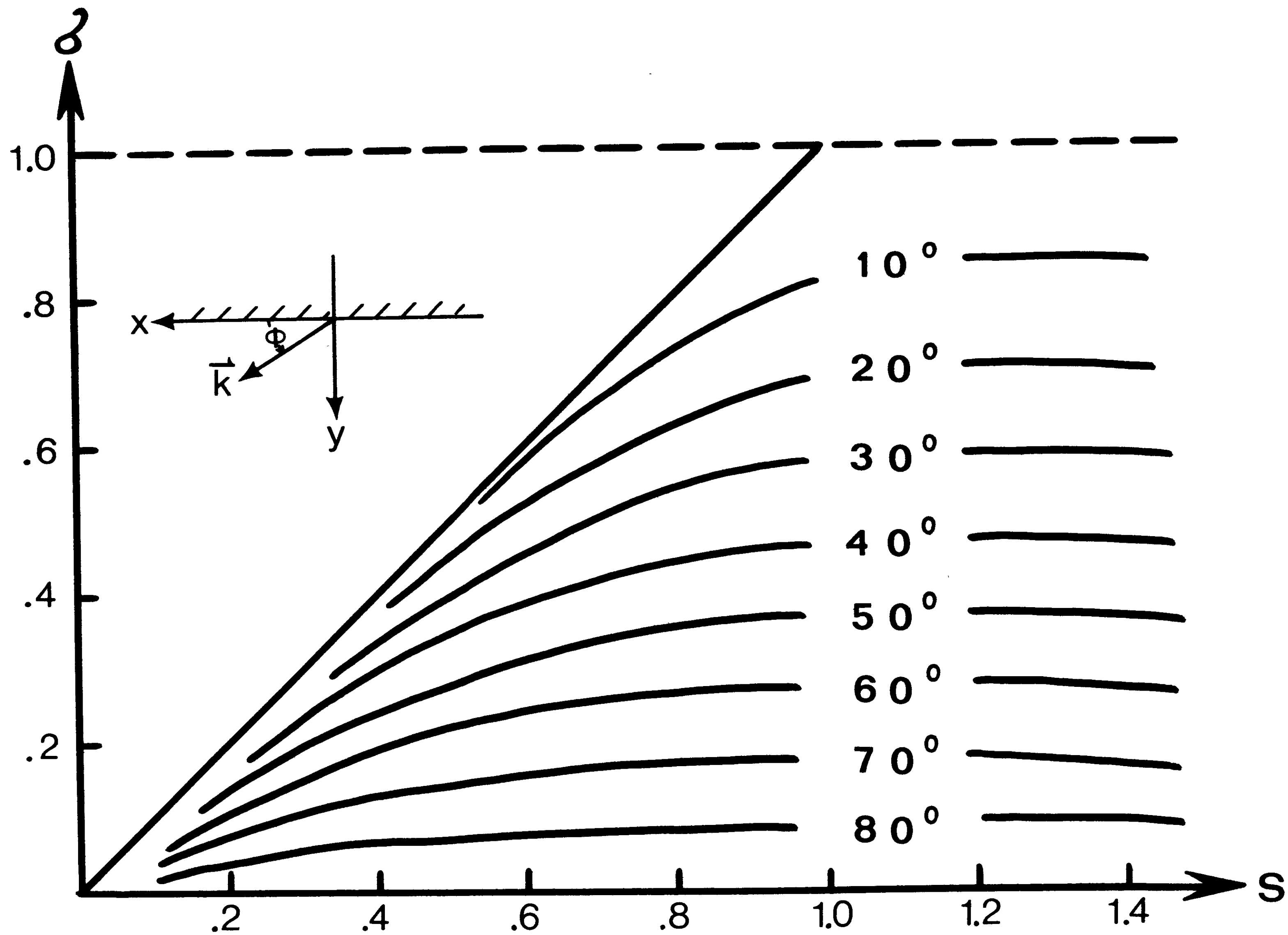

Figure 2.7. Contours of ϕ in the far field.

$$\overrightarrow{k'} \cdot \overrightarrow{v'} = 0 \qquad (2.27)$$

by mass conservation. Therefore, the particle motion is rectilinear and normal to the wave number vector. For incoming waves which must have wave number vector pointing into the first quadrant, the particle motion then lies in the second and fourth quadrant as shown in Fig. 2.6. This implies a negative Reynolds stress (i.e., $\overline{u'v'} < 0$) or an onshore flux of westward (+x) momentum.

The following results can also be derived,

$$\frac{|v|}{|u|} = \frac{|v'|}{|u'|} \cdot \cos\omega \qquad \text{(from (2.10) or Fig. 2.1)}$$

$$= \frac{k'}{\sqrt{1-k'^2}} \cdot \cos\omega \qquad \text{(from (2.27) and (2.20))}$$

$$= \frac{\sigma/S}{\sqrt{1-(\sigma/S)^2}} \qquad \text{(from (2.11) and (2.12))}$$

$$= \tan\Theta, \qquad (2.28)$$

where

$$\Theta = \sin^{-1}(\sigma/S) \qquad (2.29)$$

gives the orientation of the particle motion in the horizontal plane measured clockwise from the positive x-axis, as shown in Fig. 2.6. The functional relations between $|v|/|u|$, Θ, and σ/S are plotted in Fig. 2.8. Again, the fluid motion is more perpendicular to the isobaths as the frequency approaches the short wave cut-off. The value of σ/S, above which the motion is more normal than tangential to the isobaths is given by $\sin\pi/4$, or 0.71.

Since w and v are 180° out of phase along the bottom, they remain so everywhere in the far field because they are both exponentially decaying away from the bottom. Given the

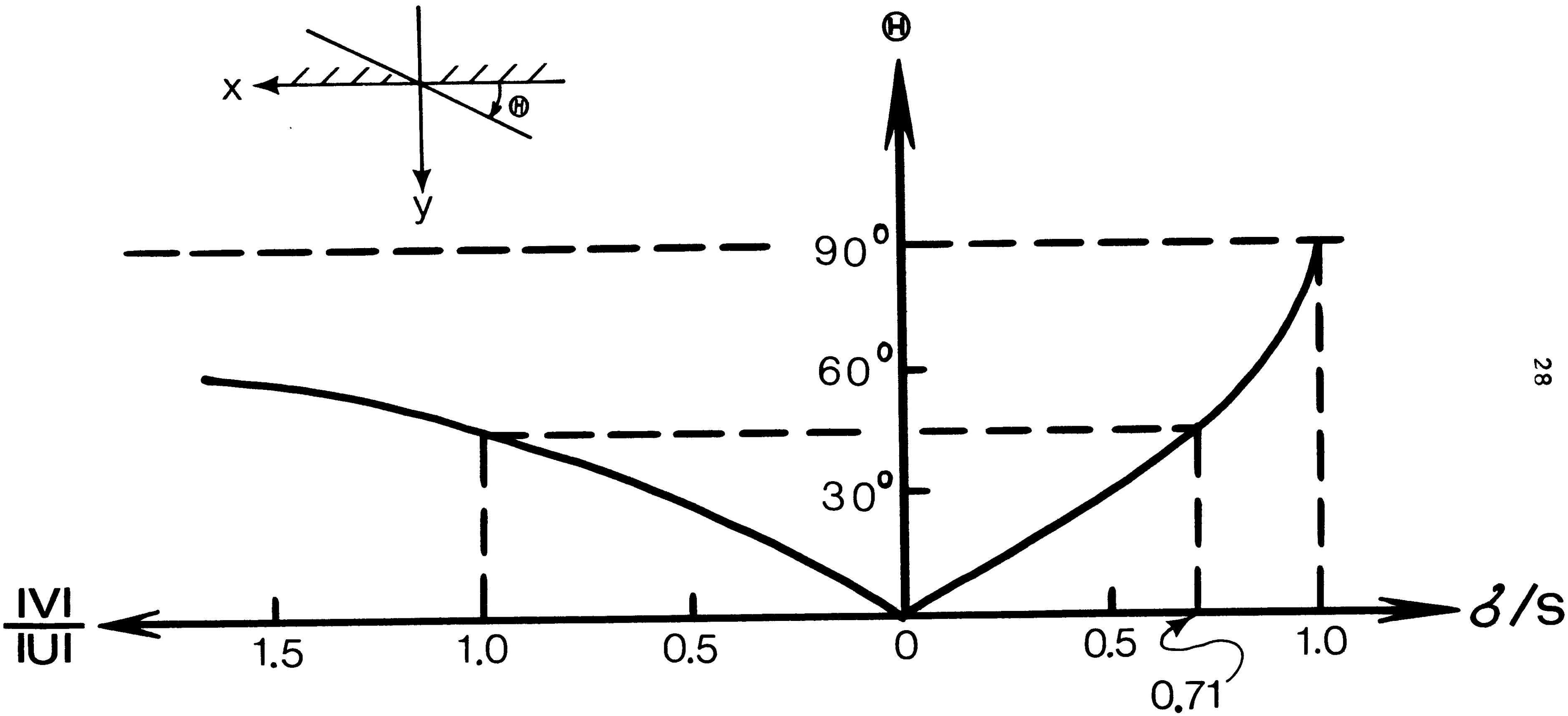

Figure 2.8. Functional relations between $|v|/|u|$, Θ, and σ/S in the far field.

fact that w is always in quadrature with ρ, the cross-wedge density flux $\overline{v\rho}$ vanishes in the far field.

In Appendix C, assuming a small linear friction in the interior region, we have derived expressions for the mean flow induced by these waves. It is found that to a first approximation the mean flow can be calculated as if these waves were inviscid. Since the mean cross-wedge flow is found to follow the contours of the density flux $\overline{v\rho}$ (see (C.5) in Appendix C), they must also vanish in the far field. The longshore mean flow is found to be given by (see (C.6) in Appendix C),

$$\overline{u} = \frac{1}{\sigma}(\overline{lu_y \cdot v} + \overline{lu_z \cdot w} + k \cdot \overline{v\rho}).$$

Since the incoming waves have their phase propagating outward and downward, all the three terms on the right hand side of this equation are positive and hence a positive longshore mean flow $\overline{u}$ is induced. By plugging the solution (2.21) into this equation, we derive that

$$\overline{u'} \equiv \frac{\overline{u}}{k|u|_\infty^2} = \frac{1}{2\sigma[1-(\sigma/S)^2]}, \qquad (2.30)$$

which is plotted in Fig. 2.9. Notice that for a given $S \lesssim 1$, and with $|u|_\infty$ and k fixed, $\overline{u}$ approaches infinity when the frequency approaches zero or the short wave cut-off.

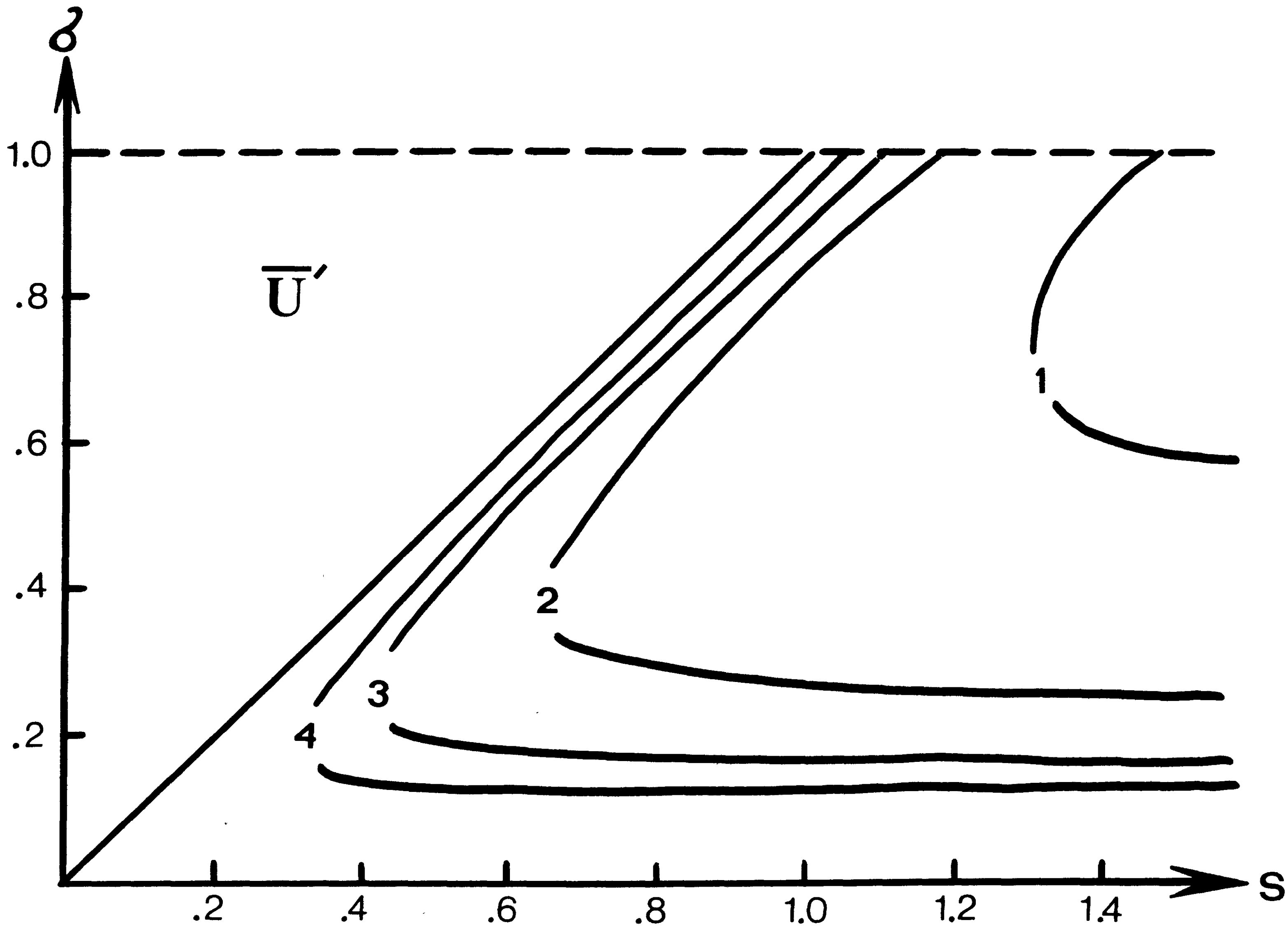

Figure 2.9. Contours of some nondimensionalized longshore mean flow at the bottom in the far field.

2.2.2 Asymptotic Solution for Small S

Using the saddle point method, Friedrichs (1948) obtained a very accurate asymptotic representation for the solution of a surface gravity wave impinging on a gently sloping beach at normal incidence. By a straightforward extension of his method, a similar expression can be obtained for our solution (2.17) when S approaches zero for an arbitrary incidence angle. Readers are referred to Appendix B for the derivation of the following results.

Let R_Λ and R_A denote the ratio of the cross-wedge wavelength and pressure amplitude to their asymptotic values in the far field. It is shown in Appendix B that

$$R_\Lambda = \frac{\lambda\sqrt{1-K'^2}}{B}, \tag{2.31}$$

$$R_A = \frac{(1-K'^2)^{1/4}}{2}\cdot\frac{\left(\frac{1}{r_1}-\lambda\right)\sqrt{\frac{\frac{1}{r_2}-\lambda}{\frac{1}{r_2}+\lambda}}+\left(\frac{1}{r_1}+\lambda\right)\sqrt{\frac{\frac{1}{r_2}+\lambda}{\frac{1}{r_2}-\lambda}}}{\sqrt{j(\lambda)}}, \tag{2.32}$$

where r_1, r_2 are given by (2.19),

$$\begin{aligned} j(\lambda) &= \left(\frac{1}{r_1^2}-\lambda^2\right)\cdot\lambda K'(\lambda)\cdot\frac{A}{B} \\ &= \frac{B}{A}\left(\tanh^{-1}\lambda r_1+\tanh^{-1}\lambda r_2\right)+\int_0^{\lambda r_1}\tanh^{-1}u\cdot\frac{du}{u} \\ &\quad+\int_0^{\lambda r_2}\tanh^{-1}u\cdot\frac{du}{u}-\frac{\pi}{2}\ln(r_1 r_2), \end{aligned} \tag{2.33}$$

$A = 1 + r_1 r_2 \lambda^2$,

$B = 1 - r_1 r_2 \lambda^2$,

and λ is related to the spatial coordinate y' by the equation

$$\begin{aligned} Sy' &\sim \omega y' \\ &= \frac{\lambda}{A}\tanh^{-1}\frac{\lambda}{A}. \end{aligned} \tag{2.34}$$

since $\omega \sim S$ in this asymptotic limit.

We plot in Fig. 2.10 and Fig. 2.11 the contours of constant R_Λ and R_A as a function of k' and $\epsilon = \omega k'y'$. For this asymptotic case we are considering, $k' \sim \sigma/S$, and $\epsilon \sim (Sk)y$ is the distance from the apex multiplied by some constant factor.

Figure 2.10 shows that the cross-wedge wavelength decreases as the wave approaches the apex. This refraction phenomenon is due primarily to the increased effect of vortex stretching as the water depth decreases. Since the lower frequency waves have their amplitude more confined to the bottom, they don't feel as much the presence of the upper surface until relatively closer to the apex.

As a consistency check for the dispersion relation, let's observe that in the far field ($Sy' \gg 1$), (2.34) implies that $\lambda \sim 1/r_1$. From (B.17) in Appendix B, the cross-wedge wavenumber l' is

$$l' = B / \lambda \tag{2.35}$$

$$\sim \sqrt{1 - k'^2}\,, \tag{2.36}$$

which agrees with the solution (2.20). Therefore, the dispersion relation in the far field agrees with (2.26), which in the limit $S \ll 1$, simplifies to

$$\phi = \tan^{-1}\sqrt{\left(\frac{S}{\sigma}\right)^2 - 1} = \cos^{-1}\left(\frac{\sigma}{S}\right). \tag{2.37}$$

This is the same result Rhines (1970) obtained for the short wavelength quasi-geostrophic motions over a gently sloping bottom. This agreement is expected since the short wavelength assumption applies in the far field and the quasi-geostrophic

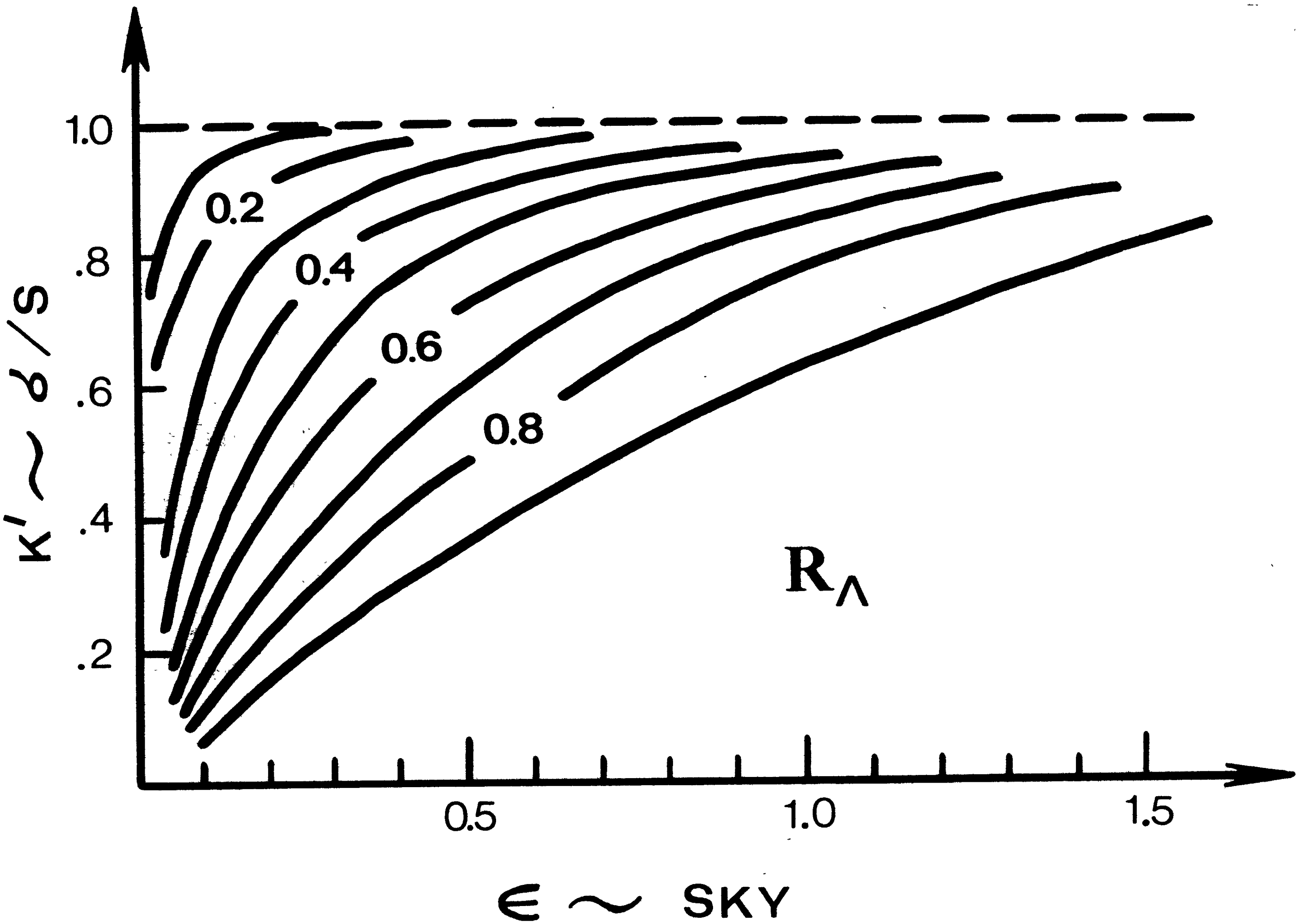

Figure 2.10. Contours of R_Λ.

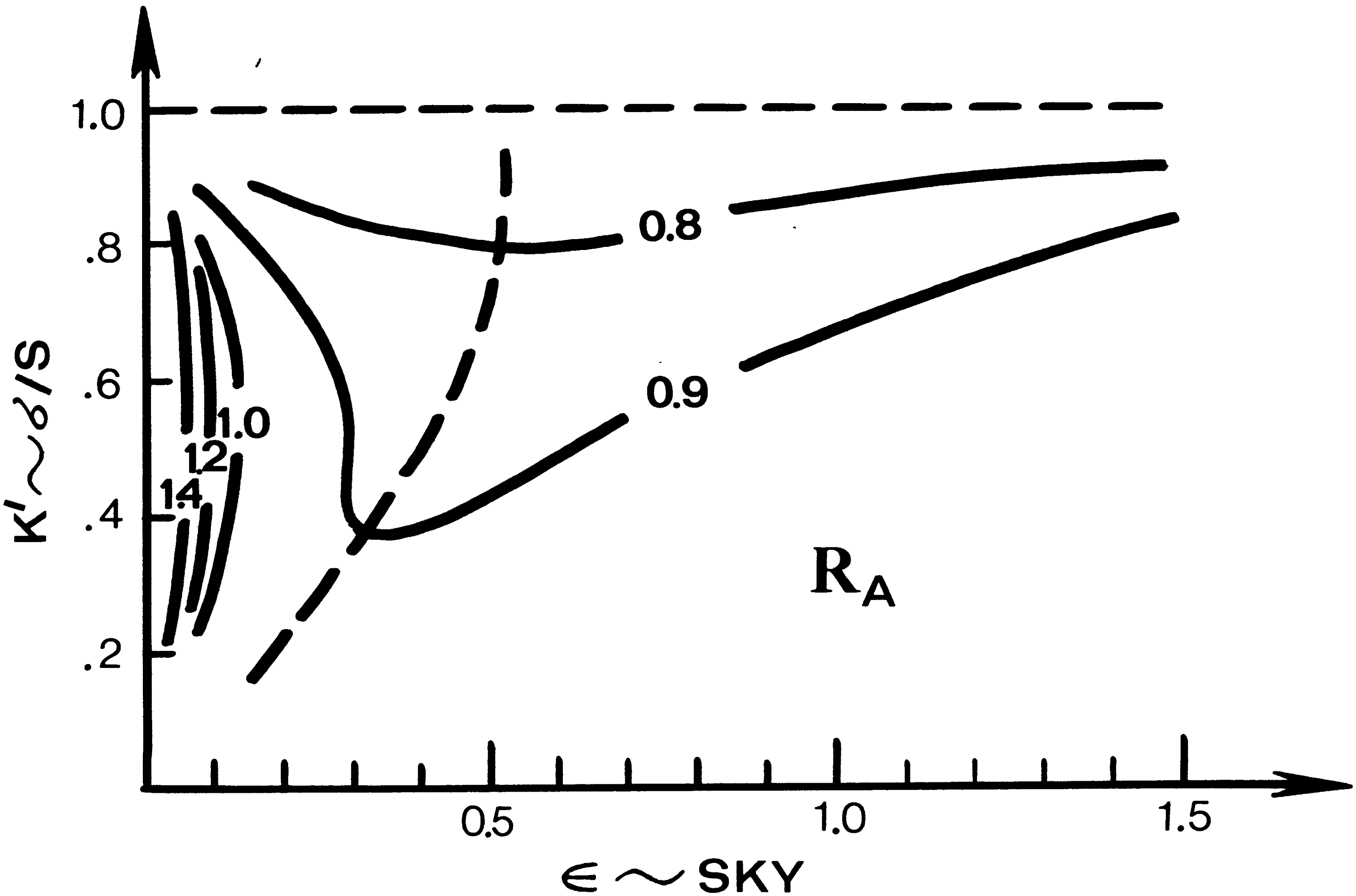

Figure 2.11. Contours of R_A. The thick broken line indicates the minimum.

assumption holds better when the bottom slope is small.

In the near field, where the motion becomes more barotropic, we expect the local dispersion relation to be given by that of the familiar barotropic topographic waves. This is indeed the case, as will be shown next. In the near field where $Sy' \ll 1$, (2.34) implies that,

$$Sy' \sim \lambda^2 \ll 1, \tag{2.38}$$

which implies from (2.35) that

$$l' \sim 1/\lambda. \tag{2.39}$$

These two relations ((2.38) and (2.39)) can be combined to give

$$Sy' \sim 1/l'^2,$$

or, since $y' \sim (k/k')\,y$, $l' \sim (k'/k)\,l$ from (2.10),

$$Sk' \sim k/(l^2 y),$$

or, since $k' \sim \sigma/S$ from (2.11) and (2.12),

$$\sigma \sim k/(l^2 y).$$

Therefore, in the dimensional units,

$$\sigma \sim \frac{f \tan\theta^*}{h} \cdot \frac{k}{\ell^2}. \tag{2.40}$$

This is the dispersion relation for the barotropic topographic Rossby waves when $l \gg k$, which holds in the near field. The refraction phenomenon follows clearly from (2.40), which, in addition, shows that $l \sim h^{-1/2}$ in the near field, i.e., the wavelength decreases as a square root of the local depth.

The most striking feature in Fig. 2.11 is the presence of an amplitude minimum shown by the thick broken lines. This is also commonly noticed in the theory of surface gravity waves. The following illustration is an attempt to help understand this result.

Consider the w field propagating toward the apex from infinity. As it begins to encounter the upper surface, the wave field must be modified in order to satisfy the boundary condition that w vanishes there. To a first approximation, this modified wave field can be regarded in its initial stage as a superposition of the original wave and its image wave that is symmetrical across the y-axis but with a π radians phase difference, as shown in Fig. 2.12, where the phase lines are represented by the thin broken lines in the y-z plane, and the amplitude is plotted along the x-axis with thick solid and broken lines representing the primary and image waves respectively. For a small slope, the phase lines are approximately perpendicular to the surface, and conceivably, the wave field of the image wave along the line CD has the same sign as that along the line AB (i.e., AC is shorter than a quarter of a wavelength), this image wave would therefore tend to decrease the amplitude at the point D. Bear in mind that this is only the initial effect as the wave first encounters the surface, and the boundary condition along the bottom is still approximately satisfied. As we move closer to the apex, the addition of a single image wave of course is not enough to satisfy all the boundary conditions, and the above argument breaks down.

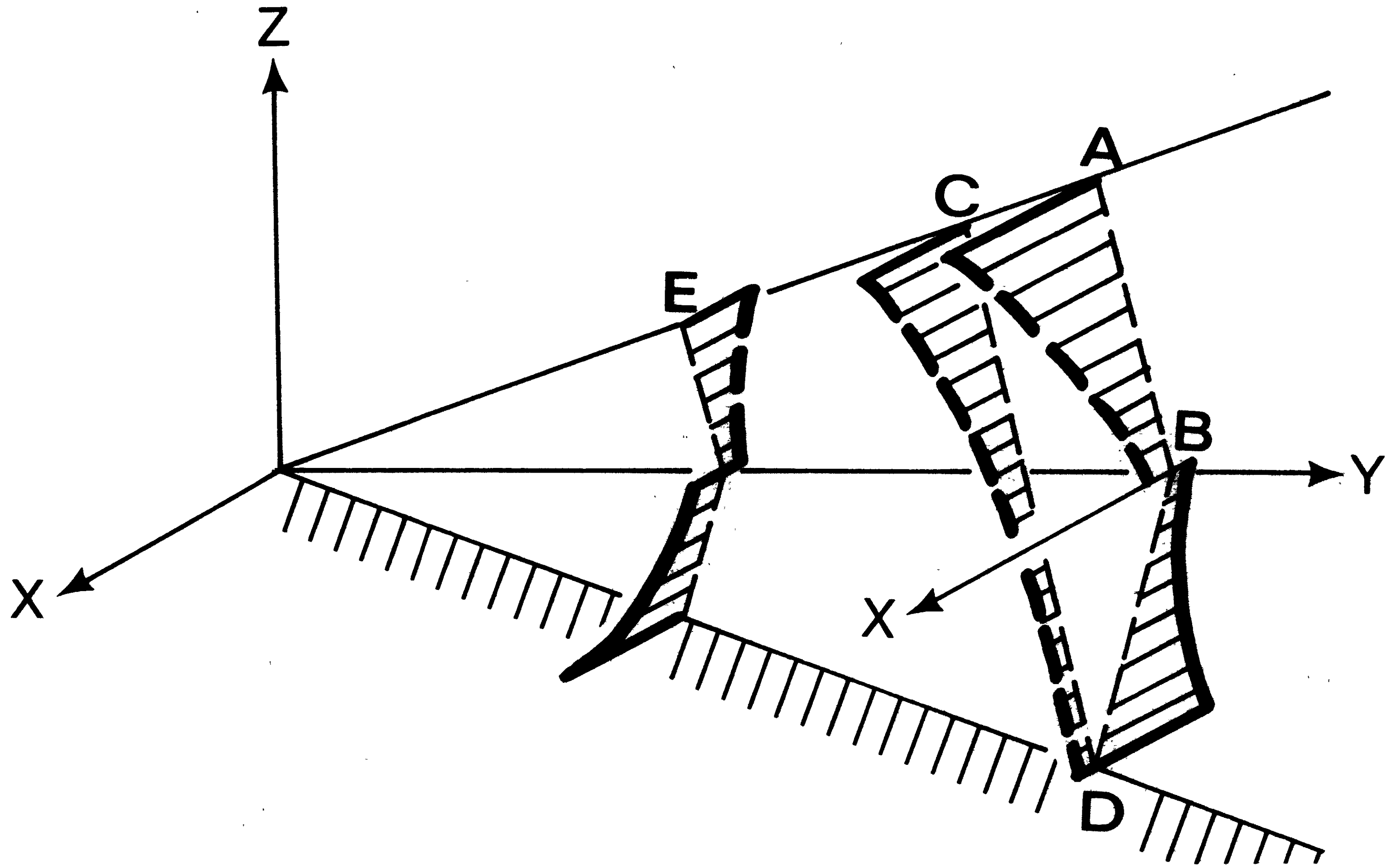

Figure 2.12. The w field of the primary wave and its image wave. The phase lines are shown by the thin broken lines on the y-z plane, and the amplitude is plotted along the x-axis with thick solid and broken lines representing the primary and image waves respectively. A and E are half wavelength apart.

Eventually, the wave amplitude has to increase and become singular at the apex. From this presence of image waves, we can also infer that, at the initial stage, the phase lines are tilted toward the vertical axis near the surface. This surface effect on the pressure field is expected to be smaller, since $p \sim \int_0^z w \cdot dz \cdot (\text{constant})$ which involves an integration over a region that is dominated by the primary wave. This fact has an important bearing on the direction of the heat flux as we shall see in the next section. Also, because of the same reason we gave earlier pertaining to Fig. 2.10, the amplitude minimum is expected to be less pronounced and occurs closer to the apex for the lower frequecy waves. The singular behavior begins to emerge no more than $\epsilon \sim 0.1$ from the apex, which corresponds to a dimensional distance y* no more than 0.1 / (kS).

2.2.3 The General Solution

The solution (2.17) can be simplified considerably when the transformed slope angle ω equals $\pi/2n$ where n is an integer. Readers are referred to Appendix A for this reduction of the solution which simplifies the numerical evaluation. Calculations have been done for cases shown as solid dots in Fig. 2.2. The wave properties predicted in Section 2.2.1 for the far field check very well with these calculations. Furthermore, the general behavior predicted in Section 2.2.2 for the asymptotic case of small S also applies even when S equals 0.57. The qualitative behavior of these waves are therefore fairly predictable over the whole range $S \lesssim O(1)$ and it is sufficient to present only the solution for the case $n = 3$ and $k' = .3$ with k set to 2π, or equivalently $S = .57$ and $\delta = .15$.

The pressure field is plotted in Fig. 2.13a, where the solid and broken lines represent the amplitude and phase contours respectively. The amplitude has been normalized to unity in the far field along the bottom. A similar normalization procedure will be used for the calculations of the velocities, kinetic energy, and the longshore mean flow. In the far field, consistent with the asymptotic solutions, these waves are bottom intensified, with amplitude contours parallel to the bottom, and phase lines tilted from the vertical axis by an angle predictable from Fig. 2.4. The rigid surface requires that both amplitude and phase contours intersect the surface at

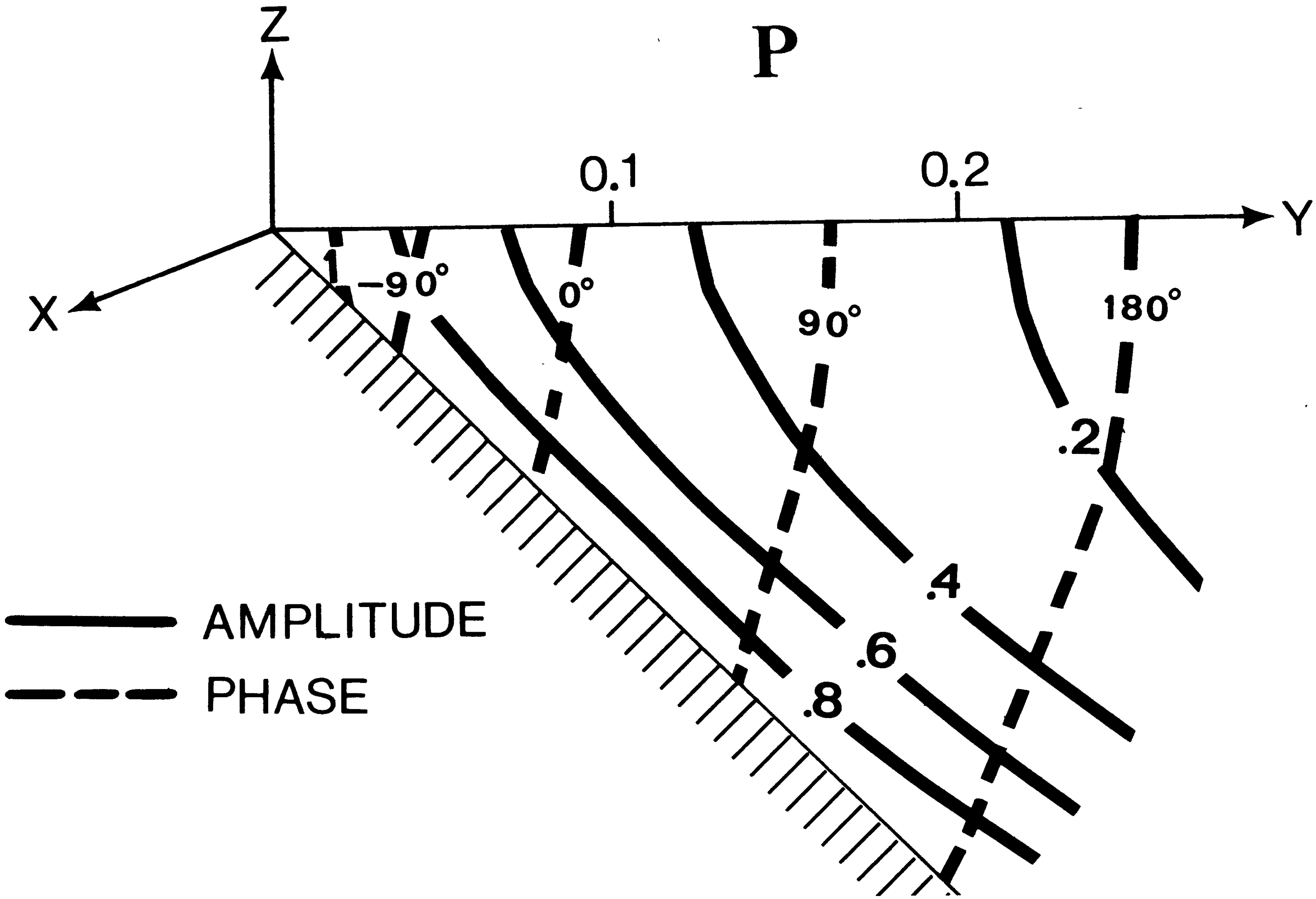

Figure 2.13a. Analytical solutions of the pressure field for the case $n = 3$ and $k' = .3$ (or equivalently $S = .57$ and $\sigma = .15$), with k set to 2π. Amplitude has been normalized to 1 at the bottom in the far field.

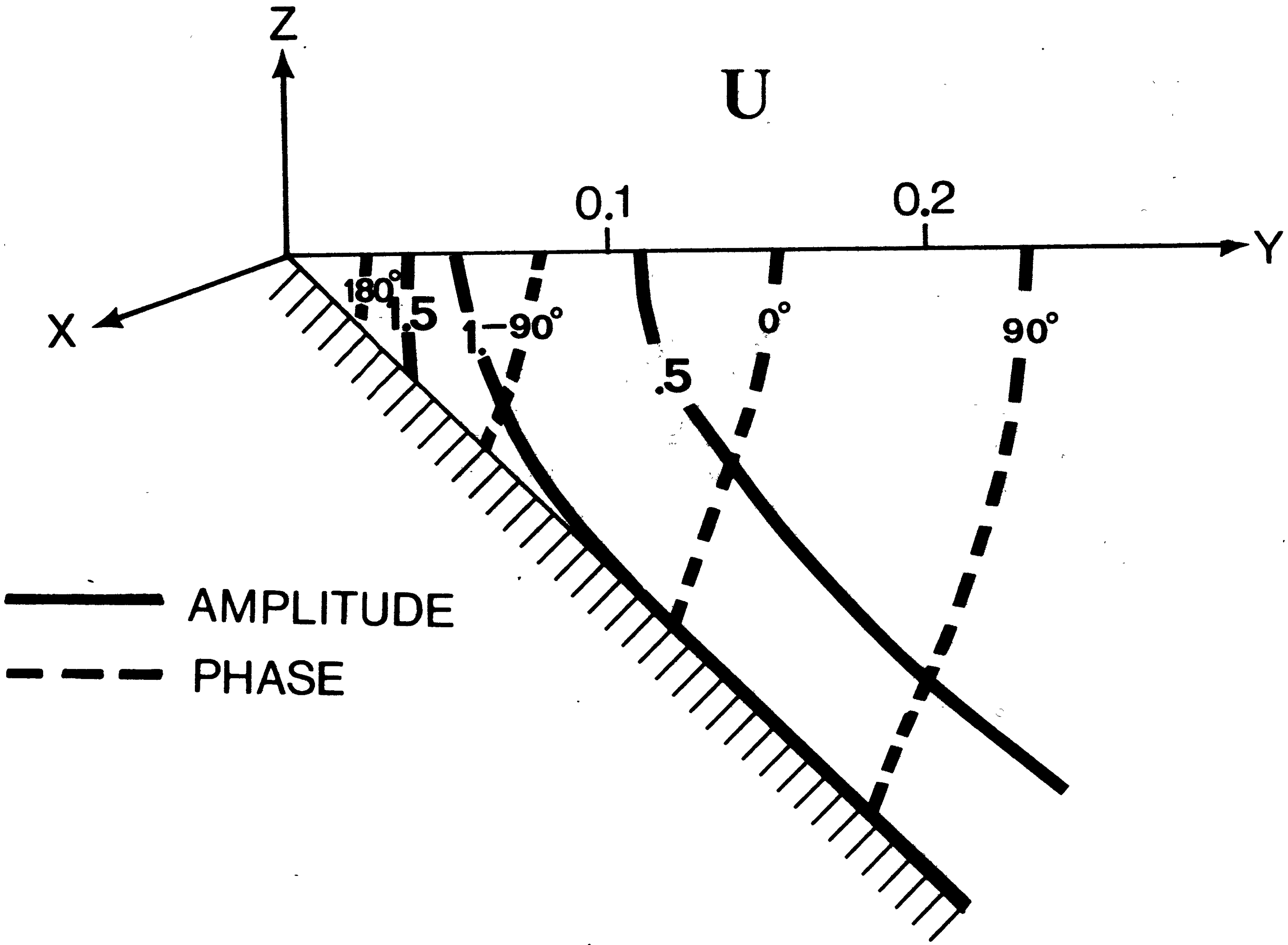

Figure 2.13b. Same as Fig. 2.13a, but for the longshore velocity u.

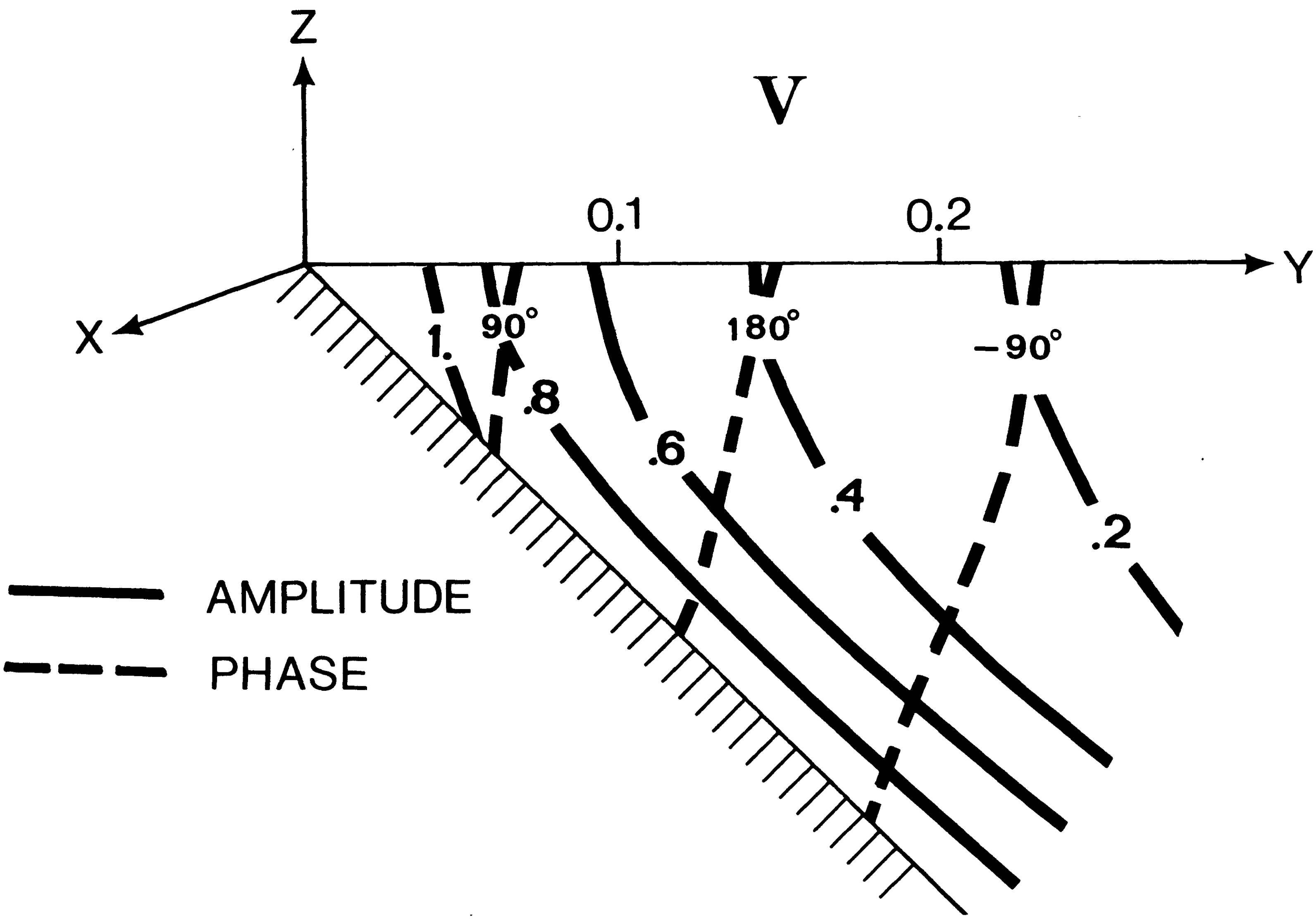

Figure 2.13c. Same as Fig. 2.13a, but for the offshore velocity v. The normalization factor is .27 if $|u| = 1$ at the bottom in the far field.

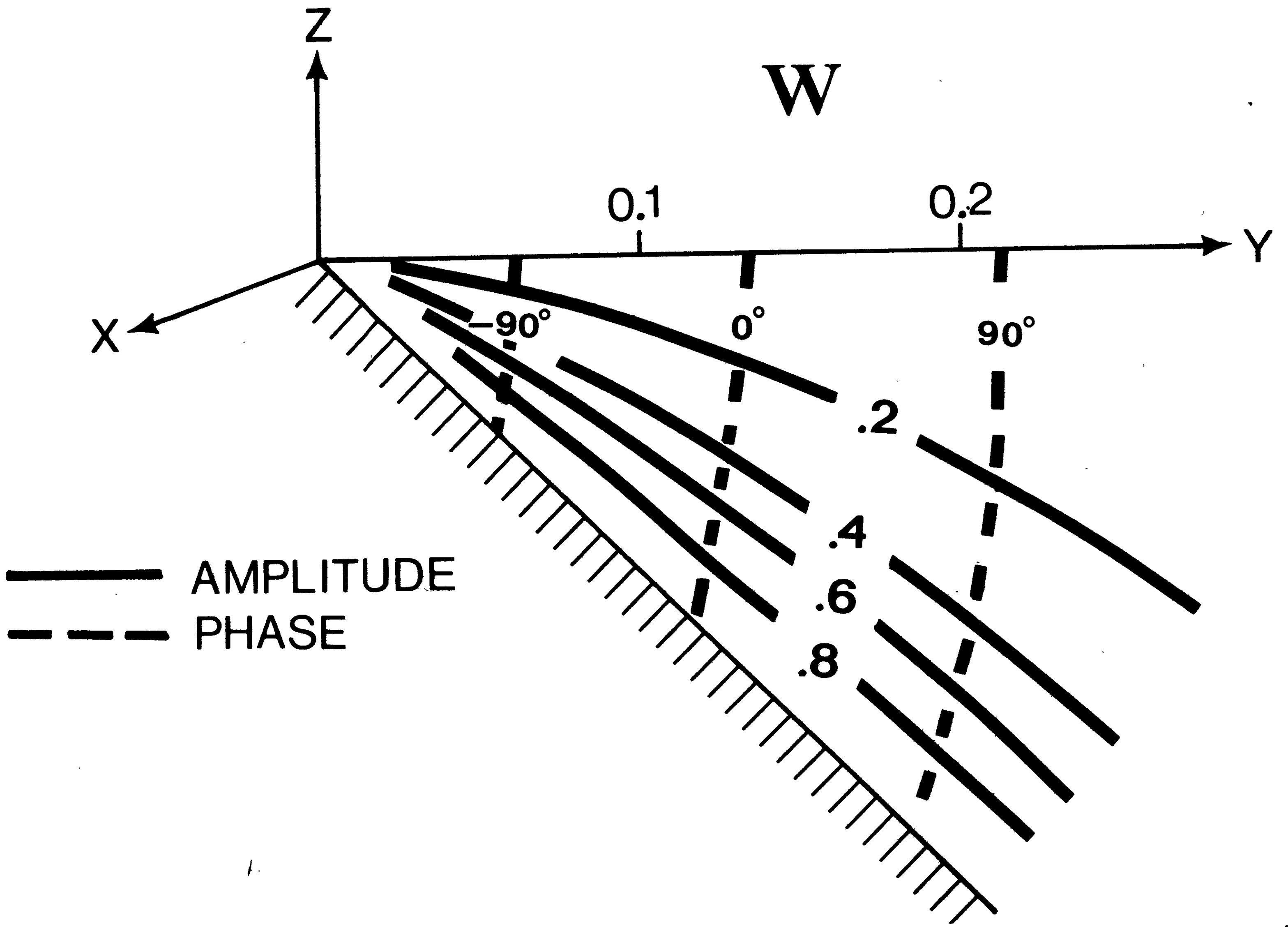

Figure 2.13d. Same as Fig. 2.13c, but for the vertical velocity w. The normalization factor is .27.

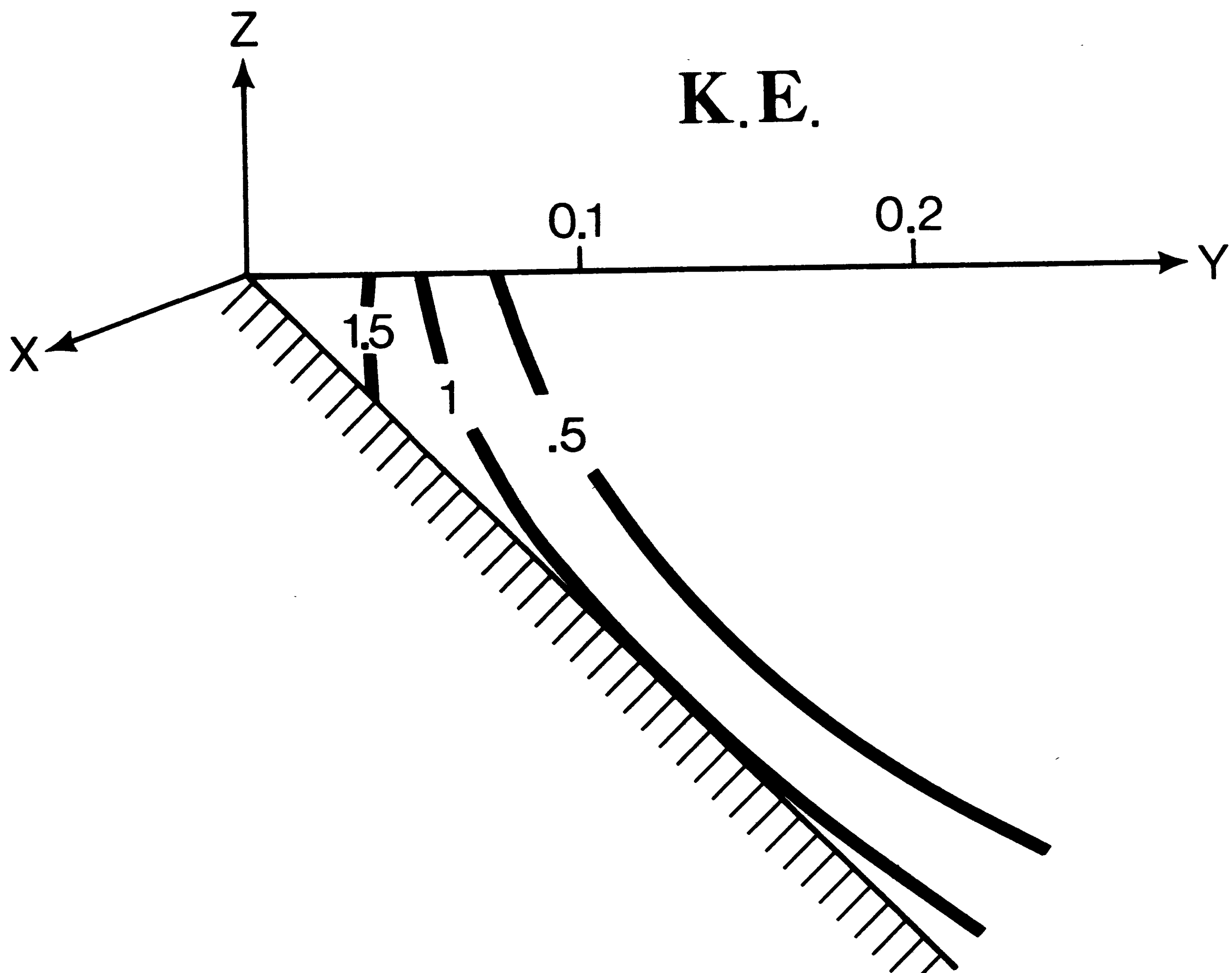

Figure 2.13e. Same as Fig. 2.13c, but for the horizontal kinetic energy. The normalization factor is .54.

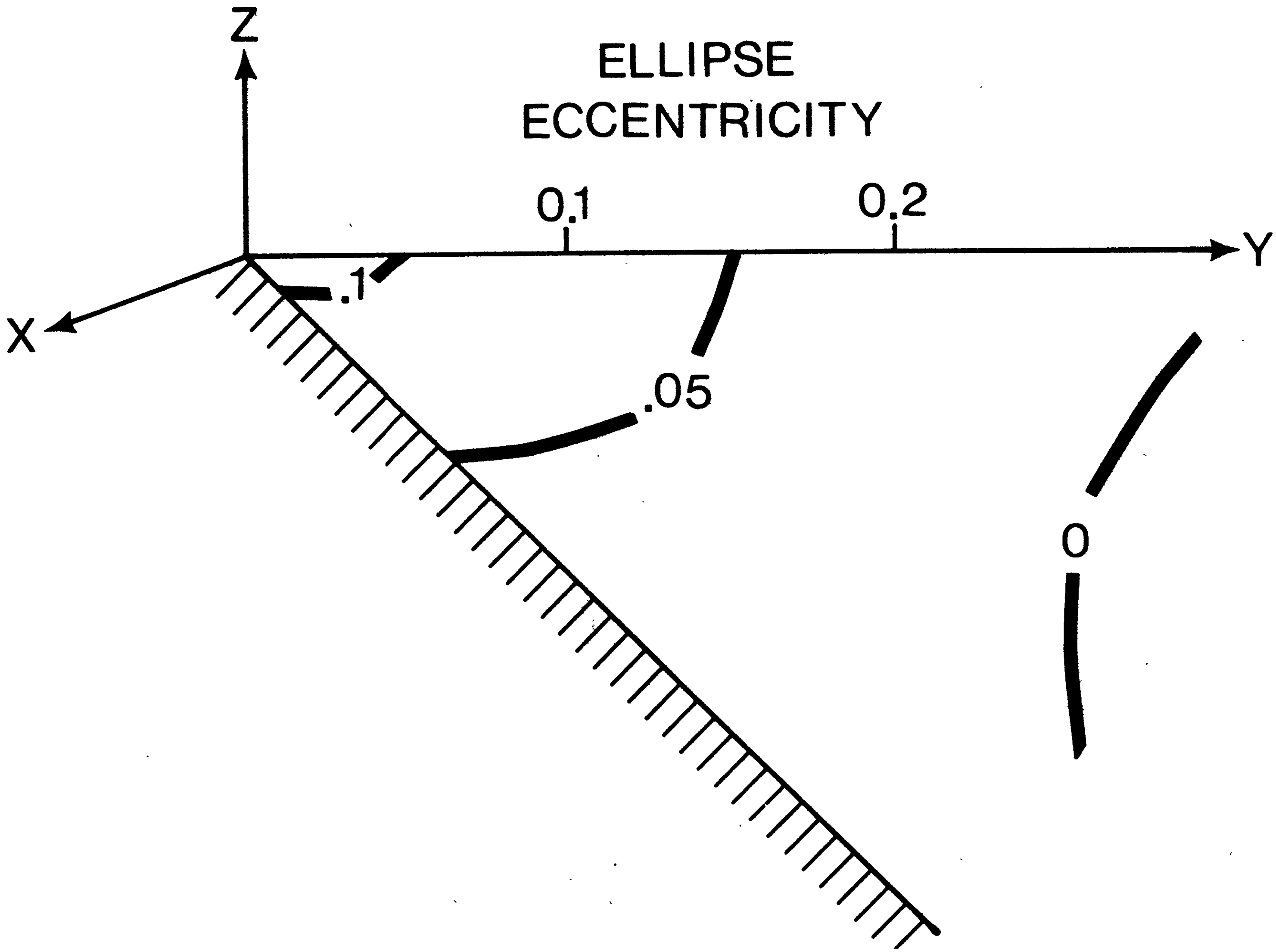

Figure 2.13f. Same as Fig. 2.13a, but for the ellipse eccentricity and no normalization is needed.

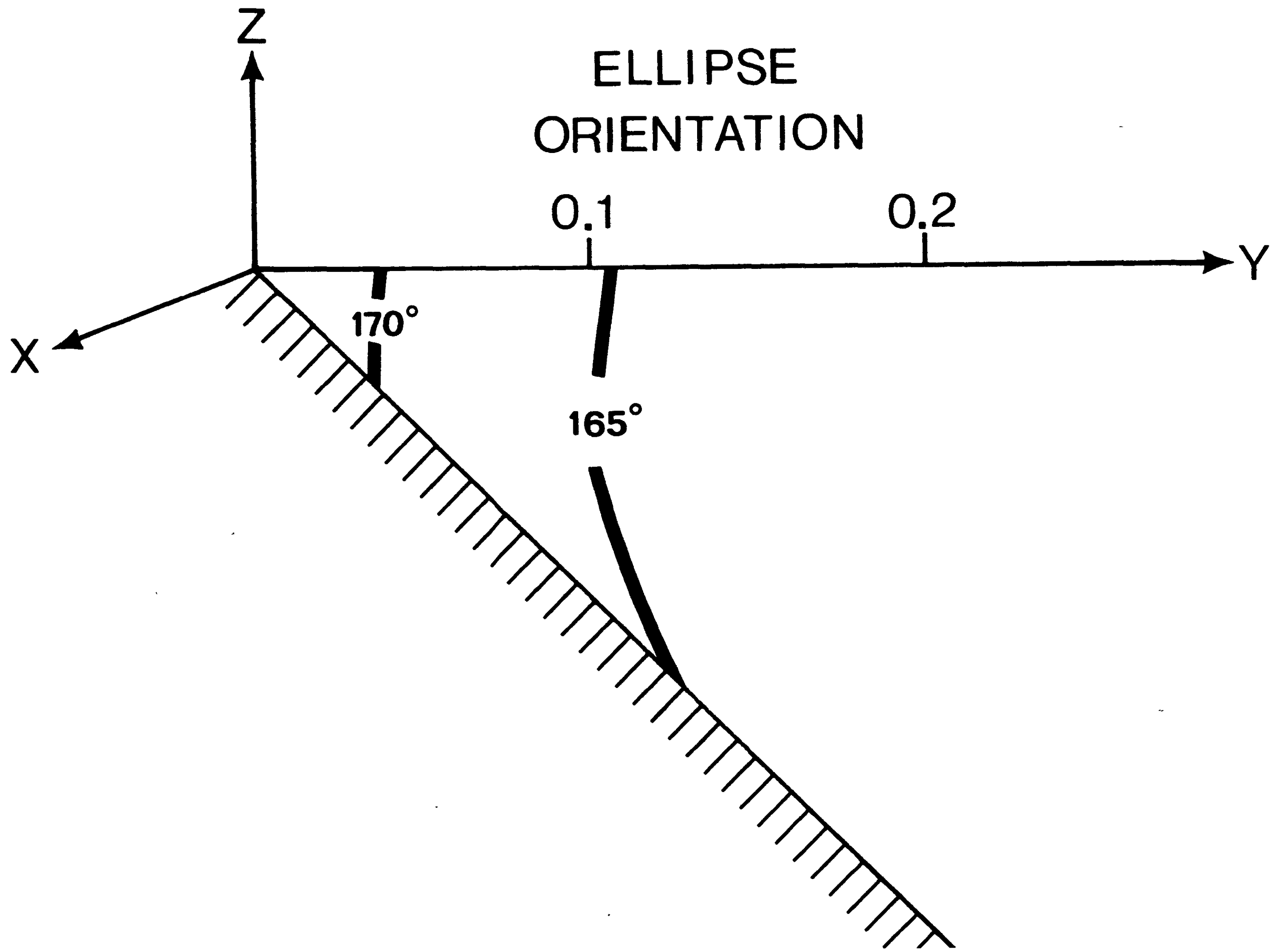

Figure 2.13g. Same as Fig. 2.13f, but for the ellipse orientation which is measured counterclockwise from the positive x-axis.

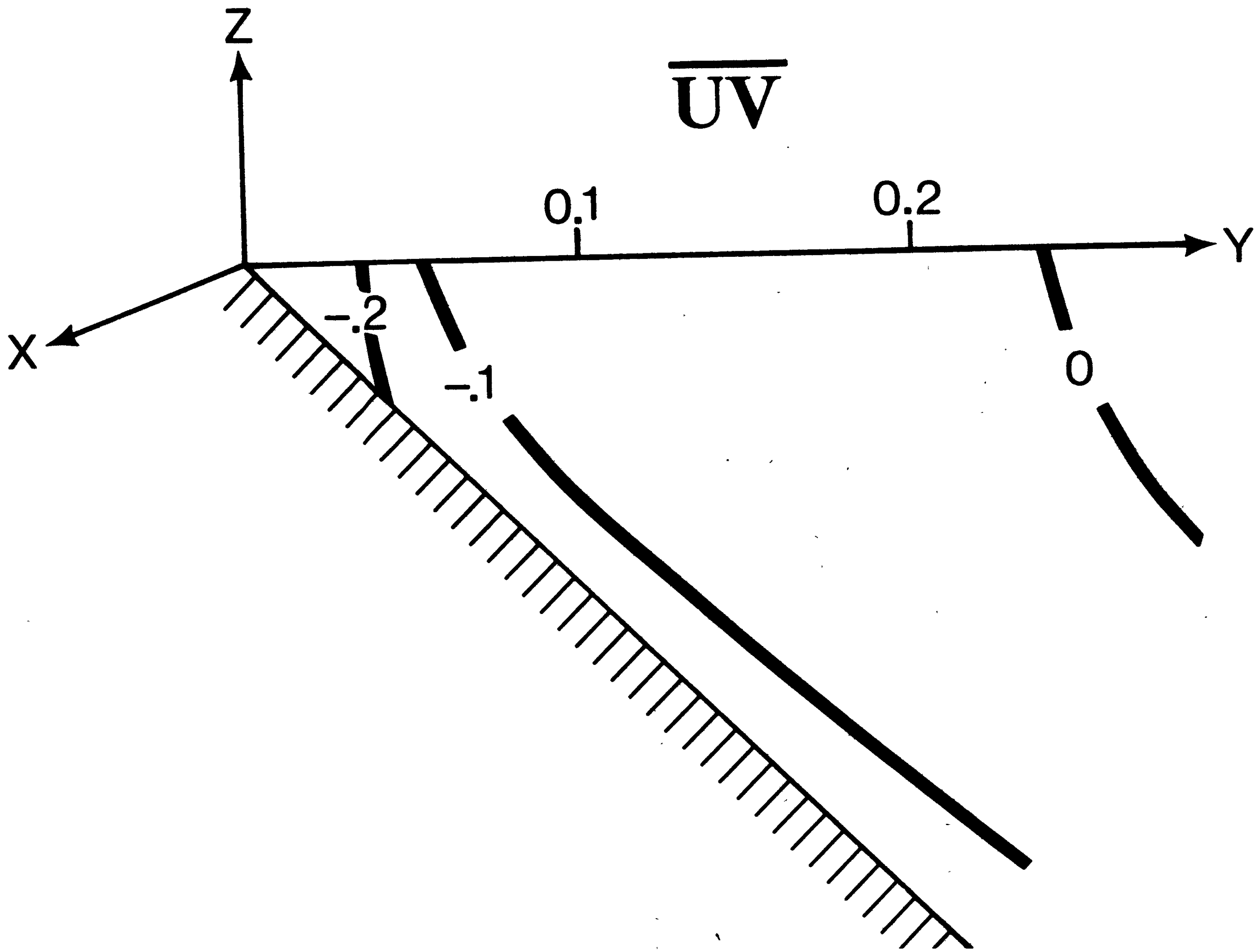

Figure 2.13h. Same as Fig. 2.13a, but for the Reynolds stress $\overline{uv}$, and the magnitude has been normalized so that $|u| = 1$ at the bottom in the far field.

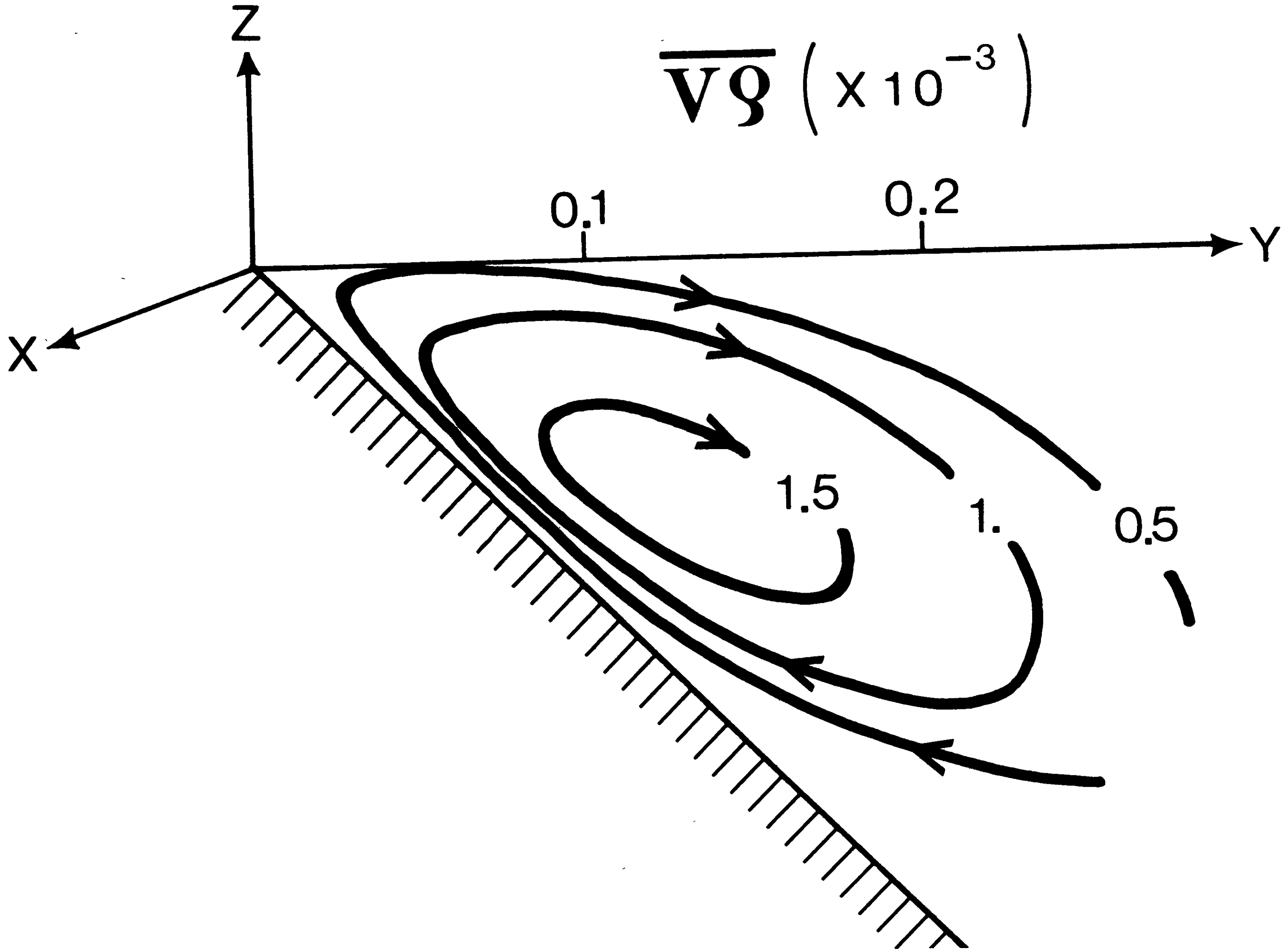

Figure 2.13i. Same as Fig. 2.13h, but for the offshore density flux $\overline{v\rho}$. Arrows indicate the direction of the mean flow.

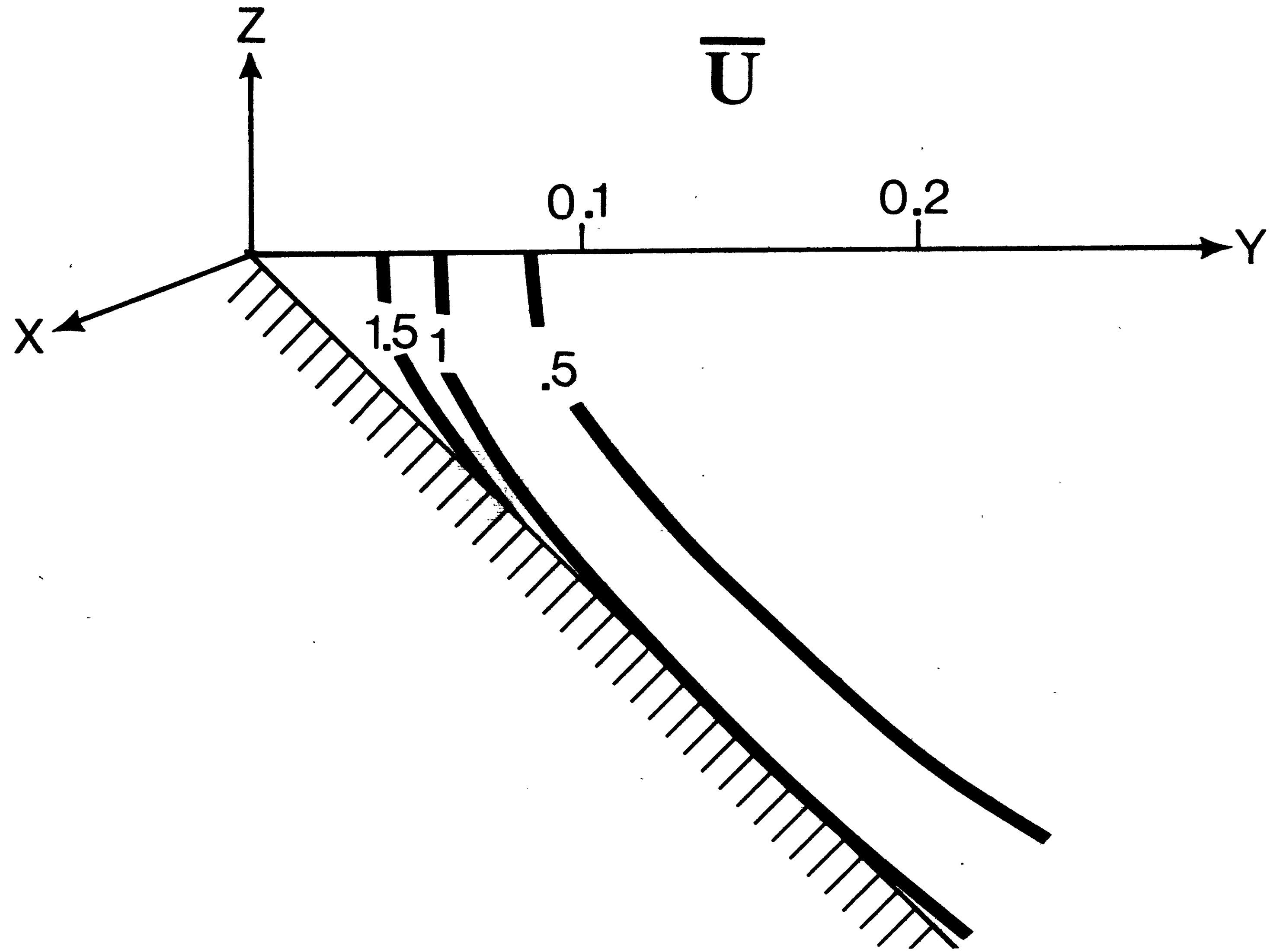

Figure 2.13j. Same as Fig. 2.13c, but for the longshore mean flow $\overline{u}$, and the normalization factor is 22.50.

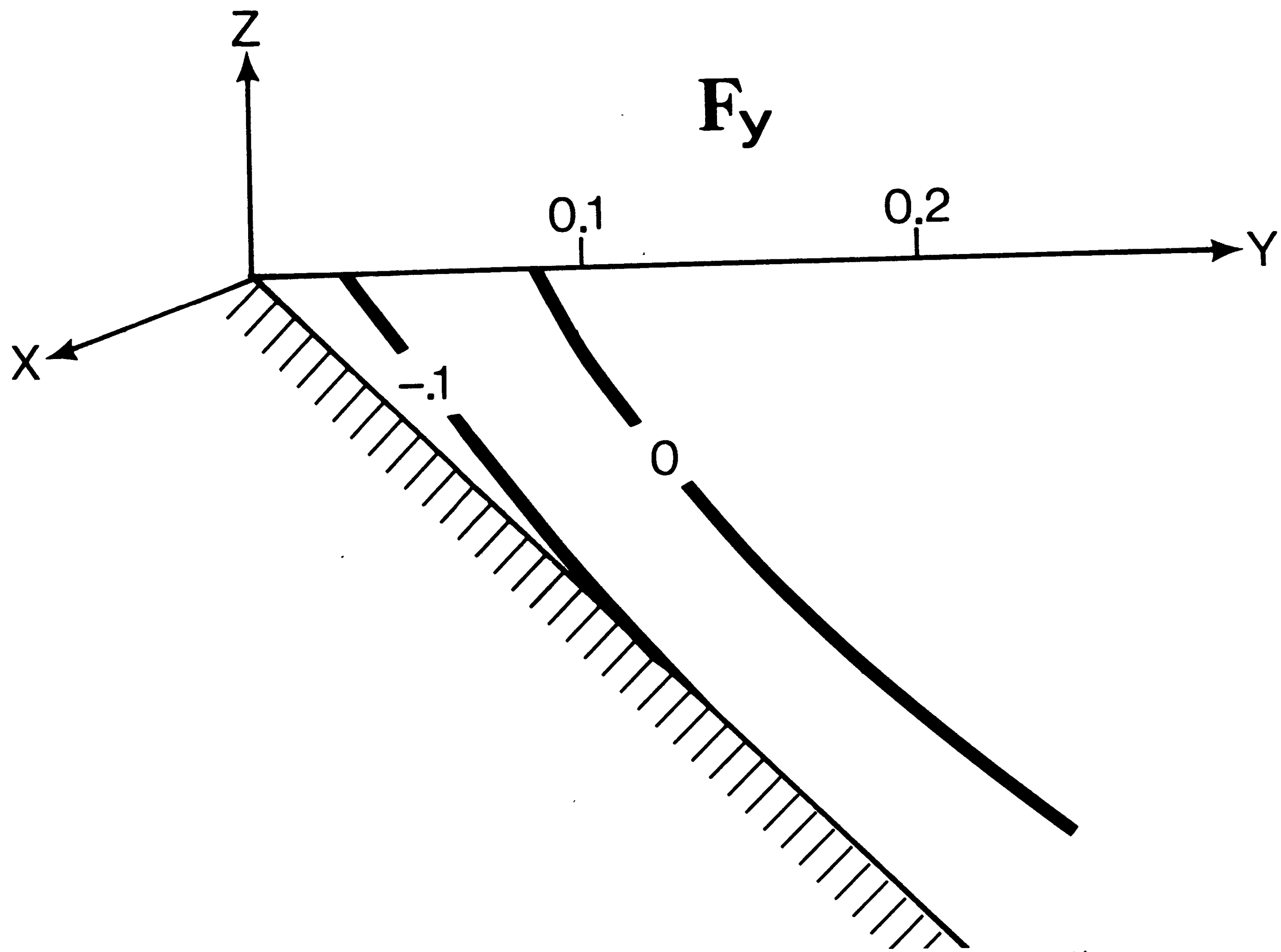

Figure 2.13k. Same as Fig. 2.13h, but for the Reynolds stress divergence F^y, defined as $-\partial_y \overline{v^2} - \partial_z \overline{vw}$.

right angles. This leads to the more barotropic appearance of the wave amplitude and the more vertical phase lines as the apex is approached. The refraction phenomenon is clearly shown by the shortening of the spacings between phase lines. Along the bottom, the amplitude first encounters a minimum before it becomes singular near the apex. This minimum has a value of .91 and occurs at $y \sim .075$, which agrees almost exactly with the values one obtains from Fig. 2.11. In fact, the agreement also holds for the other cases and hence the general behavior predicted for small S also holds for $S \sim O(1)$.

The velocities, kinetic energy, and some other wave properties are plotted in Figs. 2.13b-g. Some simple derivations assuming quasi-geostrophy can help explain the qualitative behavior of these fields. Let

$$p \sim |p| \cdot e^{ily},$$

then apart from some real and positive constant, quasi-geostrophy implies

$$v \sim ip \sim |p| \cdot e^{i(ly+\pi/2)}, \tag{2.41}$$

$$u \sim -p_y \sim \sqrt{|p|_y^2 + l^2 |p|^2} \cdot e^{i(ly+\tan^{-1}\frac{l|p|}{|p|_y})}. \tag{2.42}$$

As the apex is approached, $|v|$ therefore varies very much like $|p|$ while $|u|$ increases more rapidly due to the combined effect of bottom intensification and refraction. $|u|_{min}$ is displaced offshore from $|p|_{min}$ and the major axis of the current ellipse aligns more closely with the shoreline as the apex is approached. Since $-\pi/2 < \tan^{-1}\frac{\rho|P|}{|P|_y} < 0$, u leads v by less than 180°, which upsets the rectilinear motions in the far field and induces a counterclockwise polarization to the current ellipse. As the kinetic energy is quadratic in velocity, its minimum is more pronounced and occurs somewhere between $|u|_{min}$ and $|v|_{min}$. Also, as mentioned in the last section, the phase lines of w indeed are generally more vertical than that of the other variables.

The Reynolds stress $\overline{uv}$ and the offshore density flux $\overline{v\rho}$ are plotted in Fig. 2.13h and 2.13i, in which $|u|$ has been set to unity in the far field along the bottom. The Reynolds stress $\overline{uv}$ is always negative, and increases in magnitude toward the apex even though the current ellipse becomes less rectilinear and more parallel with the shoreline. The vertically integrated $\overline{uv}$ however has to remain constant in an inviscid model, otherwise it would accelerate indefinitely a longshore mean flow.

The imposed kinematic boundary conditions require that $\overline{v\rho}$ vanishes along the boundaries and in the far field. In the interior region, $\overline{v\rho}$ is seen to be positive. This can be explained by the following derivations. Assume that apart from some real and positive constant,

$$w \sim v\, e^{i\theta_{wv}}, \tag{2.43}$$

then, we see from Fig. 2.16b and 2.16c that the phase angle

θ_{wv} satisfies the condition

$$-\pi < \theta_{wv} < -\pi/2$$

in the interior region and therefore

$$\overline{v\rho} = \frac{B^2}{\sigma} \overline{v \cdot iw}$$

$$= -\sin(\theta_{wv}) \cdot (\text{some real and positive constant}) \qquad (2.44)$$

must be positive.

Since from (C.5) of Appendix C, the cross-wedge mean flow follows the $\overline{v\rho}$ contours, it is plotted in this same figure with its direction indicated by the arrows. Physically, the horizontal divergence (convergence) of the heat flux on the offshore (onshore) side of its maximum induces a mean sinking (rising) motion in the equilibrium state, which forms, through the mass conservation, the clockwise gyre observed. The core of the cell is located approximately above $|v|_{min}$ which is slightly displaced offshore from $|p|_{min}$.

The longshore mean flow $\overline{u}$ can be calculated from (C.6) of Appendix C, and is plotted in Fig. 2.13j. Consistent with the prediction made for the far field, it is always positive and bottom intensified. Since the divergence of the Reynolds stress

$$F^y = -\partial_y \overline{vv} - \partial_z \overline{vw}$$

is small compared to $\overline{u}$, as shown in Fig. 2.13k, $\overline{u}$ is approximately geostrophically balanced (see (C.7) in Appendix C). Given that $\overline{u}_z < 0$, the mean thermal wind relation implies a denser water near the apex.

2.3 Discrete Spectrum

Stokes (1846) has obtained an edge wave solution for surface gravity waves trapped near the apex of a wedge, and Ursell (1952) has shown that the Stokes' solution is only the fundamental mode ($n = 0$) of a discrete spectrum of possible edge wave modes. With minor modification of Ursell's solution, the solution for the n^{th} mode in our problem is given by

$$p = e^{-k'(y'\cos\omega - z'\sin\omega)} + \sum_{m=1}^{n} A_{mn}\left\{ e^{-k'[y'\cos(2m-1)\omega + z'\sin(2m-1)\omega]} + e^{-k'[y'\cos(2m+1)\omega - z'\sin(2m+1)\omega]} \right\}, \tag{2.45}$$

where

$$A_{mn} = (-1)^m \prod_{l=1}^{m} \frac{\tan(n-l+1)\omega}{\tan(n+l)\omega}, \tag{2.46}$$

and k' and ω satisfy the conditions

$$k' = \frac{1}{\sin(2n+1)\omega}, \tag{2.47}$$

and

$$\omega \leq \omega_c \equiv \frac{\pi}{2(2n+1)}. \tag{2.48}$$

The first condition gives the eigenfrequency of the n^{th} mode,

$$\sigma_n = \frac{\sin\omega}{\sin(2n+1)\omega}, \tag{2.49}$$

the first four of which are plotted against S in Fig. 2.2. The second condition is required by the assumption that the solution is coastally trapped and gives the critical value of ω below which the n^{th} mode is allowed. In the limit as S approaches zero, ω is small, and

$$\sigma_n \rightarrow \frac{1}{2n+1}, \tag{2.50}$$

which is the short wave limit of Reid's (1958) second class, barotropic, trapped waves in a wedge. Since a free surface is allowed in his model, the agreement with our rigid surface model is expected only for short waves where the surface stretching effect is negligible. The increase of the eigenfrequencies with stratification agrees with the intuition that the stratification imposes an additional restoring force.

The solution (2.45) becomes in the (y,z) space

$$p = e^{-ky} + \sum_{m=1}^{n} A^{p}_{mn}\, e^{-ky/\cos 2m\omega} \cdot \cos(kz \tan\omega \cdot \sin 2m\omega), \tag{2.51}$$

where

$$A^{p}_{mn} = 2\, A_{mn}.$$

The general modal structure of this solution will be discussed next.

Since the consecutive higher terms in the summation decay more slowly in y, they dominate the solution as we move offshore. And since they alternate in sign, the nodes are introduced, the number of which equals the mode number n. The modal structure also becomes more bottom trapped offshore because of the increasing depth and the stronger bottom trapping of the higher terms.

The u and v velocities can be derived from (2.51),

$$u = \frac{k}{1+\sigma}\left[e^{-ky} + \sum_{m=1}^{n} A^{u}_{mn}\, e^{-ky/\cos 2m\omega} \cos(kz \tan\omega \cdot \sin 2m\omega)\right], \tag{2.52}$$

$$v = \frac{ik}{1+\sigma}\left[e^{-ky} + \sum_{m=1}^{n} A^{v}_{mn}\, e^{-ky/\cos 2m\omega} \cos(kz \tan\omega \cdot \sin 2m\omega)\right], \tag{2.53}$$

where

$$A^{u}_{mn} = A^{p}_{mn} \cdot \frac{\cos 2m\omega - \sigma}{1-\sigma}, \tag{2.54}$$

and

$$A^{v}_{mn} = A^{p}_{mn} \cdot \frac{1 - \sigma \cos 2m\omega}{1-\sigma}. \tag{2.55}$$

Since $A^{u}_{mn} < A^{p}_{mn} < A^{v}_{mn}$, the nodes of u occur farther off-shore, while those of v occur closer inshore, than the corresponding ones of p. The first node of v occurs right at the apex due to the impenetrable boundary. As an example, p, u, and v are plotted in Fig. 2.14a-c for n = 1 and $\omega = 0.5\ \omega_c$ (or S = 0.249), where p and u have been normalized to unity at the apex for the pressure and velocity plots respectively. They confirm the above analysis.

To study the dependence of these modal structures on ω, we plot in Fig. 2.15, all the A_{mn} values for the mode n = 2. As ω or equivalently S increases, we see that all the A_{mn}'s decrease in magnitude. Since the y-decay rate is also reduced, we infer that the modal structure broadens in y with nodes being pushed offshore. This is clearly shown in Fig. 2.16 where the nodal positions are plotted. This effect would be the strongest for u which also becomes less depth dependent than the other variables. In the limit $\omega \rightarrow \omega_c$, p and v are no longer coastally trapped, and the second node of u is pushed to infinity since $A^{u}_{22} \rightarrow 0$. These trapped solutions look similar to some of the patterns shown by Wang (1976) since they represent a special case of Wang's numerical solutions.

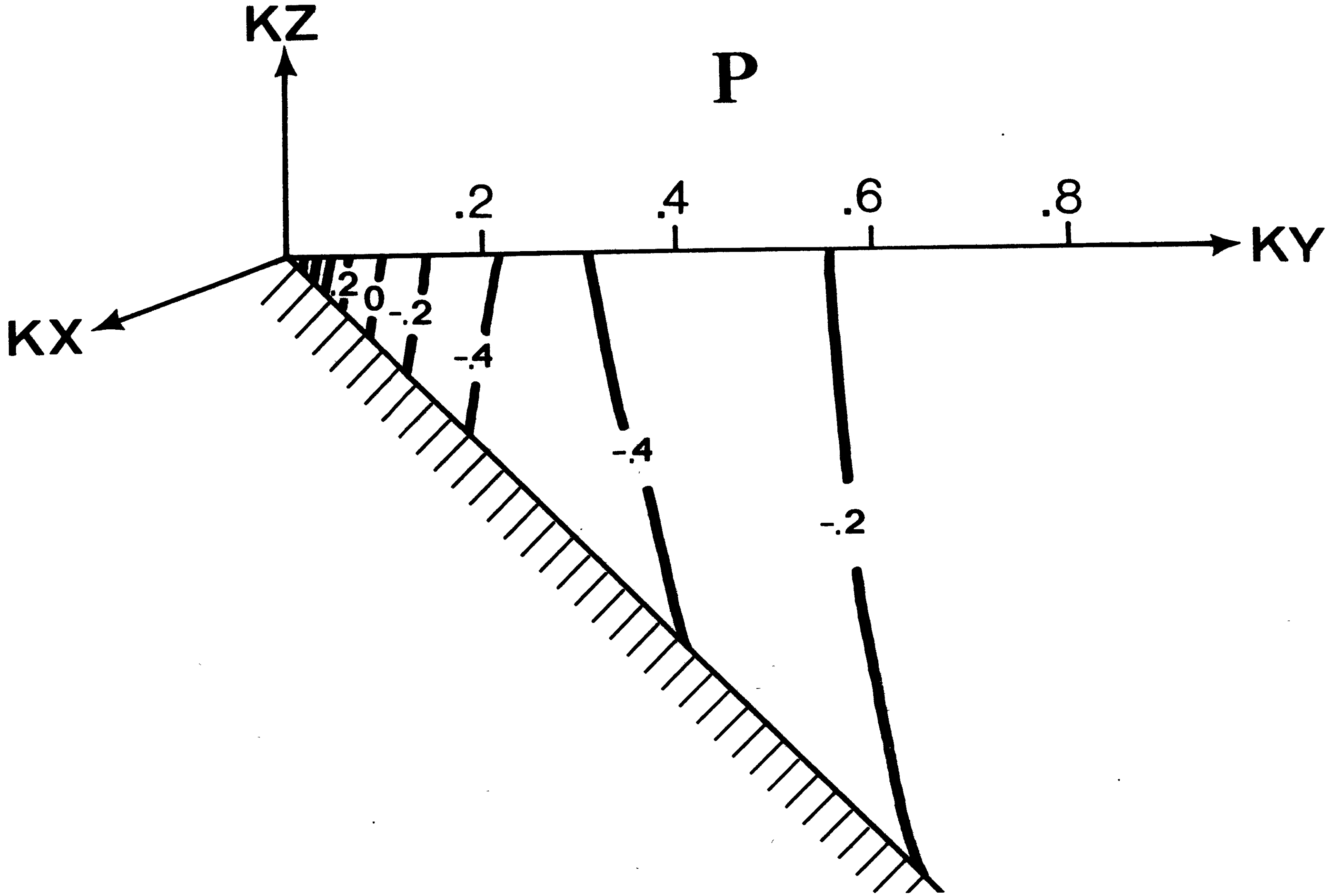

Figure 2.14a. Pressure fields of the first coastally-trapped mode with $\omega = 0.5\,\omega_c$ (or S = .249). The amplitude has been normalized to 1 at the apex.

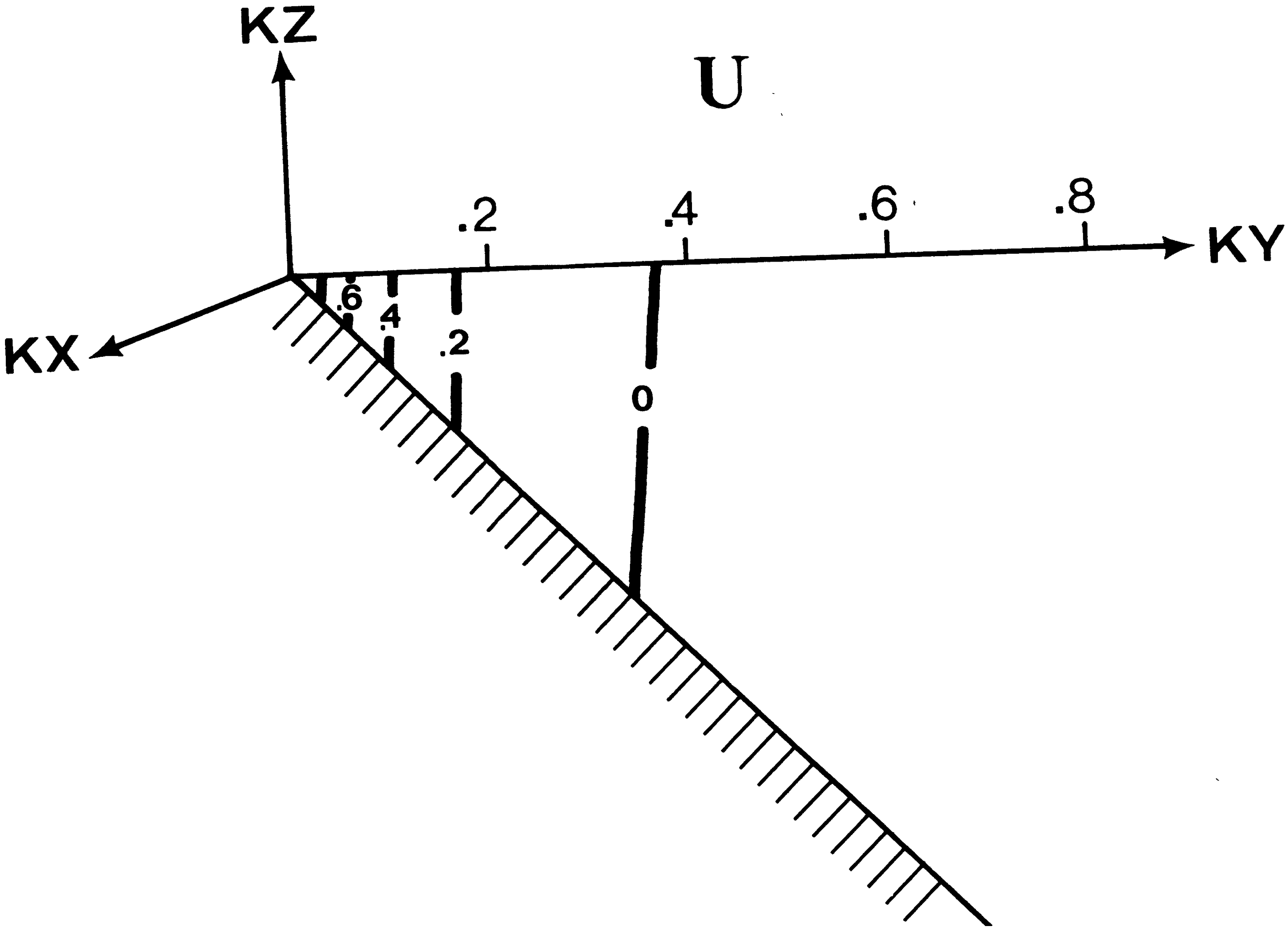

Figure 2.14b. Same as Fig. 2.14a, but for the longshore velocity u.

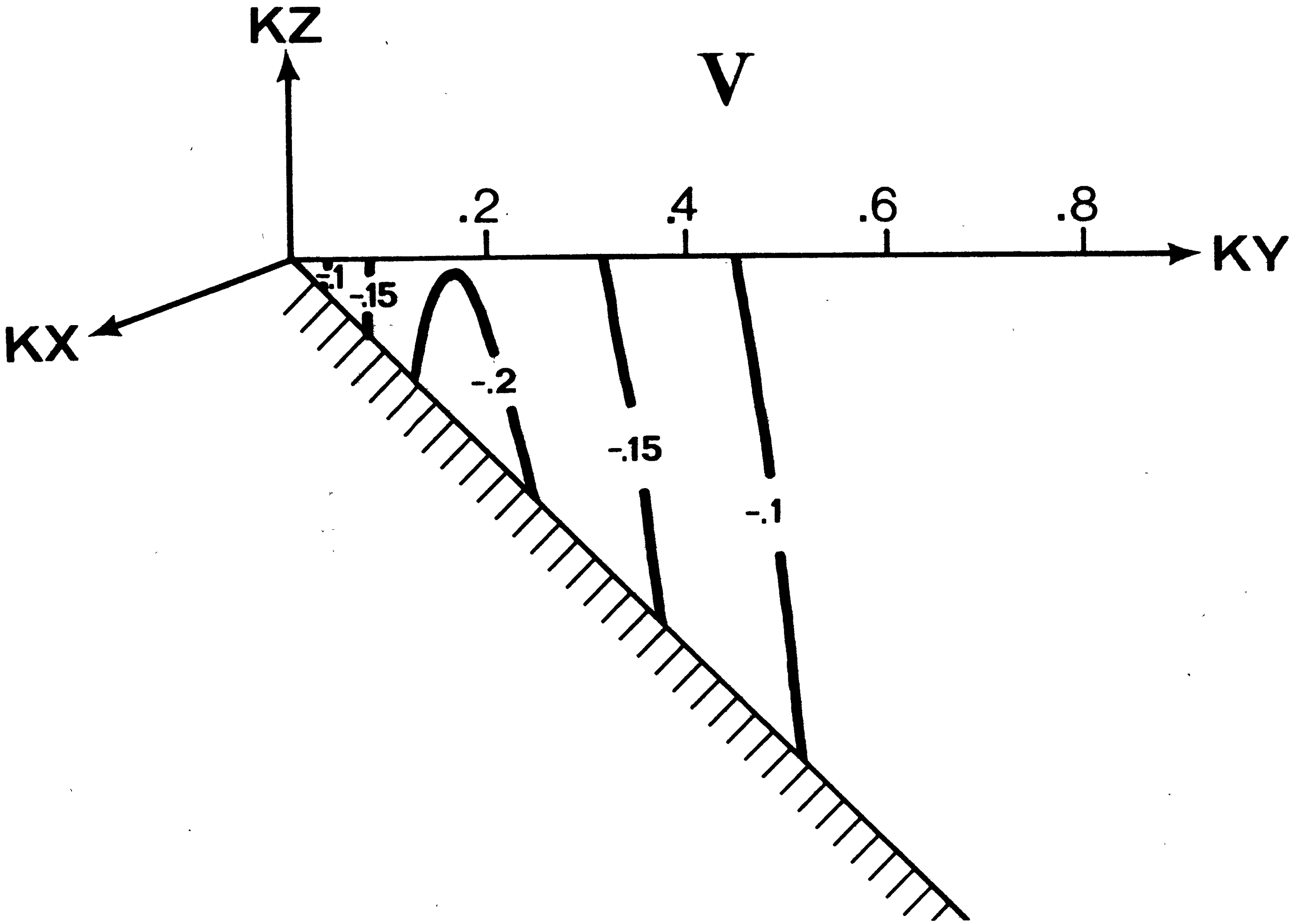

Figure 2.14c. Same as Fig. 2.14a, but for the offshore velocity v and the amplitude has been normalized so that u = 1 at the apex.

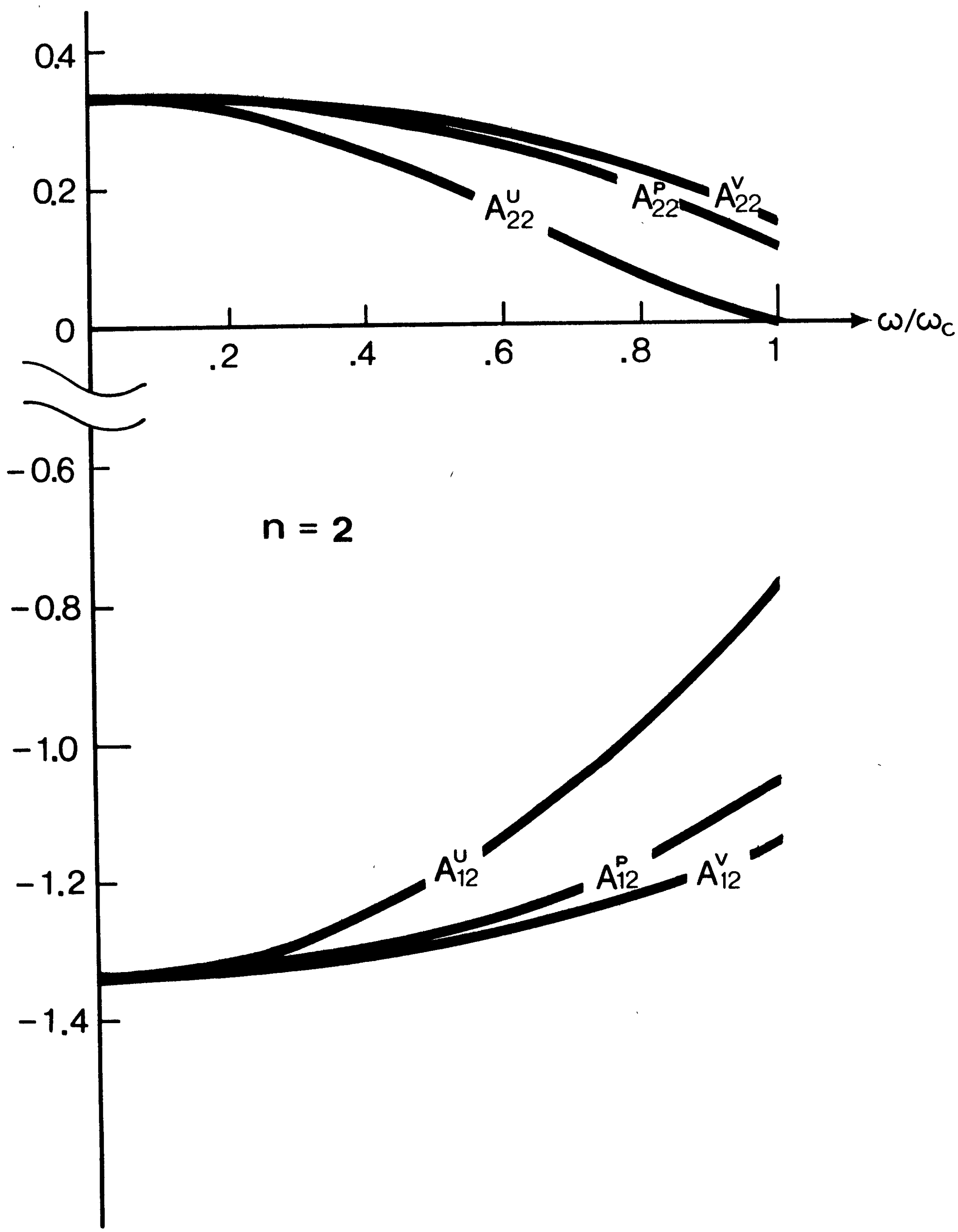

Figure 2.15. Values of all the A_{12} and A_{22}'s as a function of ω/ω_c.

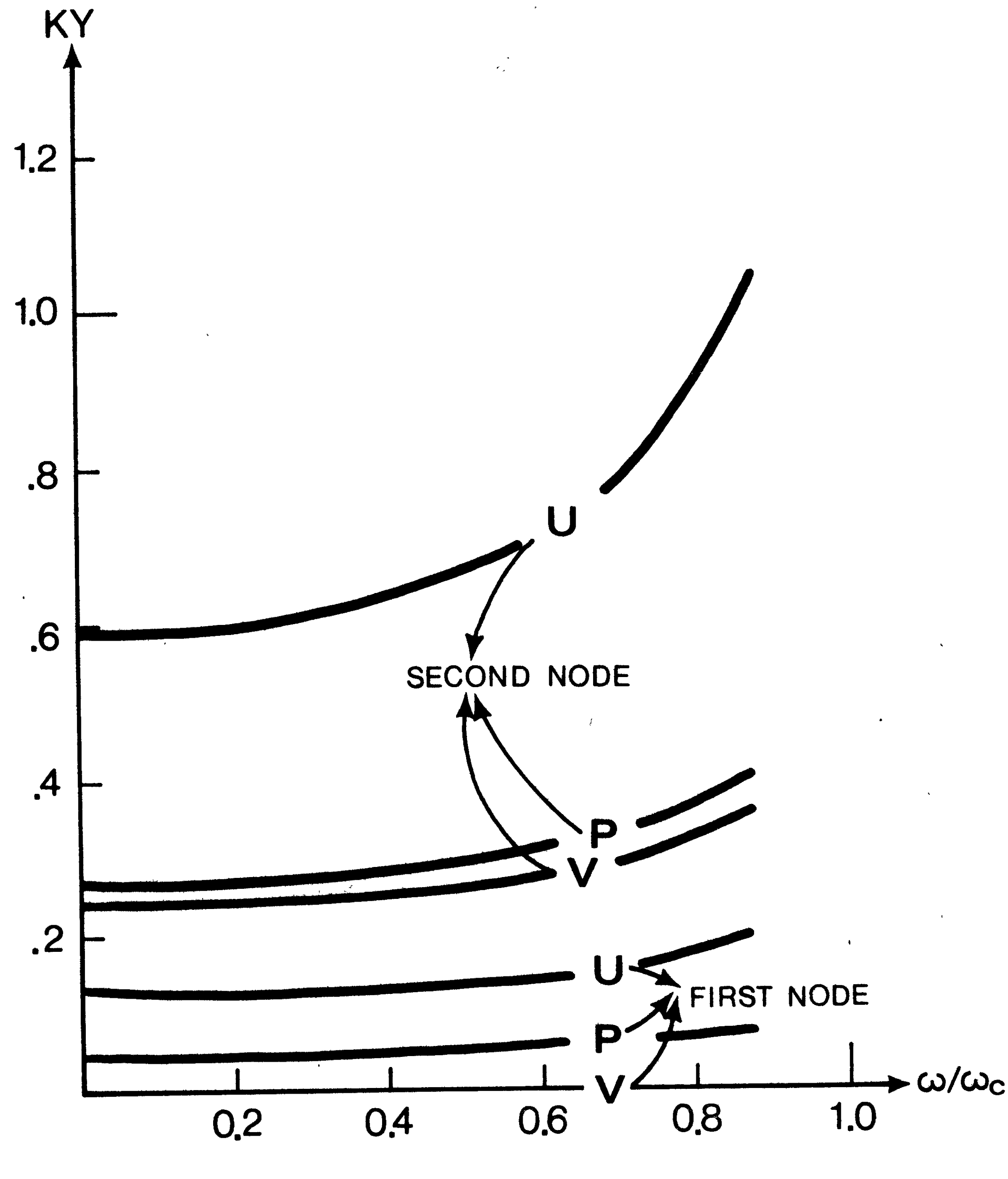

Figure 2.16. Nodal positions of p, u, and v for the second trapped mode, as a function of ω/ω_c.

2.4 Summary

We have presented in this chapter an analytical model of topographic Rossby waves propagating in an infinite wedge filled with a uniformly stratified fluid. The problem is found after some coordinate transformations to be identical to the corresponding surface gravity wave problem in a homogeneous fluid, but with the roles of the surface and bottom boundaries interchanged. Analytical solutions are thus available for both progressive and trapped waves, forming continuous and discrete spectra in frequency space. The separation occurs at a nondimensional frequency $\sigma = S$, defined as $(N/f) \tan\theta^*$, where N and f are the Brunt-Väisälä and inertial frequencies and $\tan\theta^*$ is the bottom slope. Since an infinite wedge has no intrinsic length scales, the only relevant nondimensional parameters are the frequency σ and the Burger number S. Therefore, stratification and bottom slope play the same dynamical role and the analysis is greatly simplified.

Asymptotic solutions of progressive waves have been obtained for both the far field and the small S, which enable us to examine the parameter dependence of some of the basic wave properties in the far field and the evolution of the wave amplitude and phase as they approach the apex when S is small. In the far field, these topographic Rossby waves are bottom trapped with amplitude contours parallel with the bottom and phase lines tilted from the vertical by an angle that increases for larger S and δ. The bottom trapping is stronger for larger S or smaller δ. Since the frequency depends only on the direction of the wave number vector, the group velocity is perpendicular to the phase velocity. For waves generated from some offshore source, the wave crests then propagate offshore. The angle between the wave crests and the coast is smaller for smaller S and larger δ. The particle motion is rectilinear and straddles the shoreline with the wave number vector. The particle motion becomes more perpendicular to the isobaths when the frequency increases and is more normal than tangential to the isobaths when $\delta > .71$ S. The heat flux as well as the cross-wedge mean flow vanishes in the far field. The induced longshore mean flow is approximately geostrophic and points to the left facing the apex. The greatest contribution to it comes from these waves with frequencies that are either very low or near S. The asymptotic solution for small S shows that the waves are refracted as they approach the apex, the cross-wedge wavelength decreasing as a square root of the local depth near the apex. The wave amplitude undergoes a minimum before it becomes logarithmically singular near the apex. Since the lower frequency waves are more isolated from the surface, the above phenomena are less pronounced until relatively closer to the apex.

The general solution for finite S is presented for the case S = .5 and δ = .15. The location of the amplitude minimum and its magnitude agree almost exactly with the predictions of the asymptotic case $S \ll 1$. Therefore the general behavior of the solution is fairly predictable over the whole range $S \lesssim O(1)$, and it is sufficient to discuss only the solution of this single case. It is seen that, as these waves approach the apex, the amplitudes of the horizontal velocities and the pressure become more barotropic and the phase lines become more vertical. The amplitude of the longshore velocity increases more rapidly than the onshore velocity and the current ellipse develops a counterclockwise polarization with its major axis aligned more closely with the isobaths. The Reynolds stress $\overline{uv}$ increases in magnitude and an onshore heat flux is generated in the interior. A mean clockwise gyre is induced across the transect and a bottom-intensified, geostrophically balanced longshore mean flow is induced which points in the +x direction.

The eigenfrequencies of the discrete modes decrease with decreasing S and reduce to the short wave limit of Reid's second class, barotropic edge waves when S approaches zero. The basic modal structure broadens as S increases to some critical value where it ceases to be coastally trapped. No coastally-trapped modes exist at frequencies above this critical limit.

3. A Numerical Model of Free Topographic Rossby Waves Near Continental Margins

3.1 The Model

A wedge extending to infinity in the offshore direction is, of course, an over-simplified geometry to model the continental margin. The numerical model presented here enables us to incorporate a more realistic topography which has rapid slope changes, especially over the slope-rise and shelf-slope junctions. To simplify the interpretations and for easier comparisons with other existing models, the stratification is assumed uniform and the topography shown in Fig. 3.1 is assumed to be comprised of three sections of exponentially varying bottom, corresponding roughly to the continental rise, slope and shelf. These restrictions can be easily relaxed in the model. A new coordinate system is used in this chapter with the x and y-axis pointing in the opposite directions from that used previously.

The equations we are solving are similar to (2.7) $\sim$ (2.9) except all the "$\tan\theta^*$" in the scaling rule (2.3) are replaced by H/L, and the boundary condition (2.9) is applied at the variable bottom $z = -h(y)$. The model is similar to that of Wang (1975,1976) which maps the domain of the variable bottom into a rectangle and then solves the transformed equations in a finite-differenced form. Readers are referred to Wang (1975) for the details of the model. The difference of our model lies

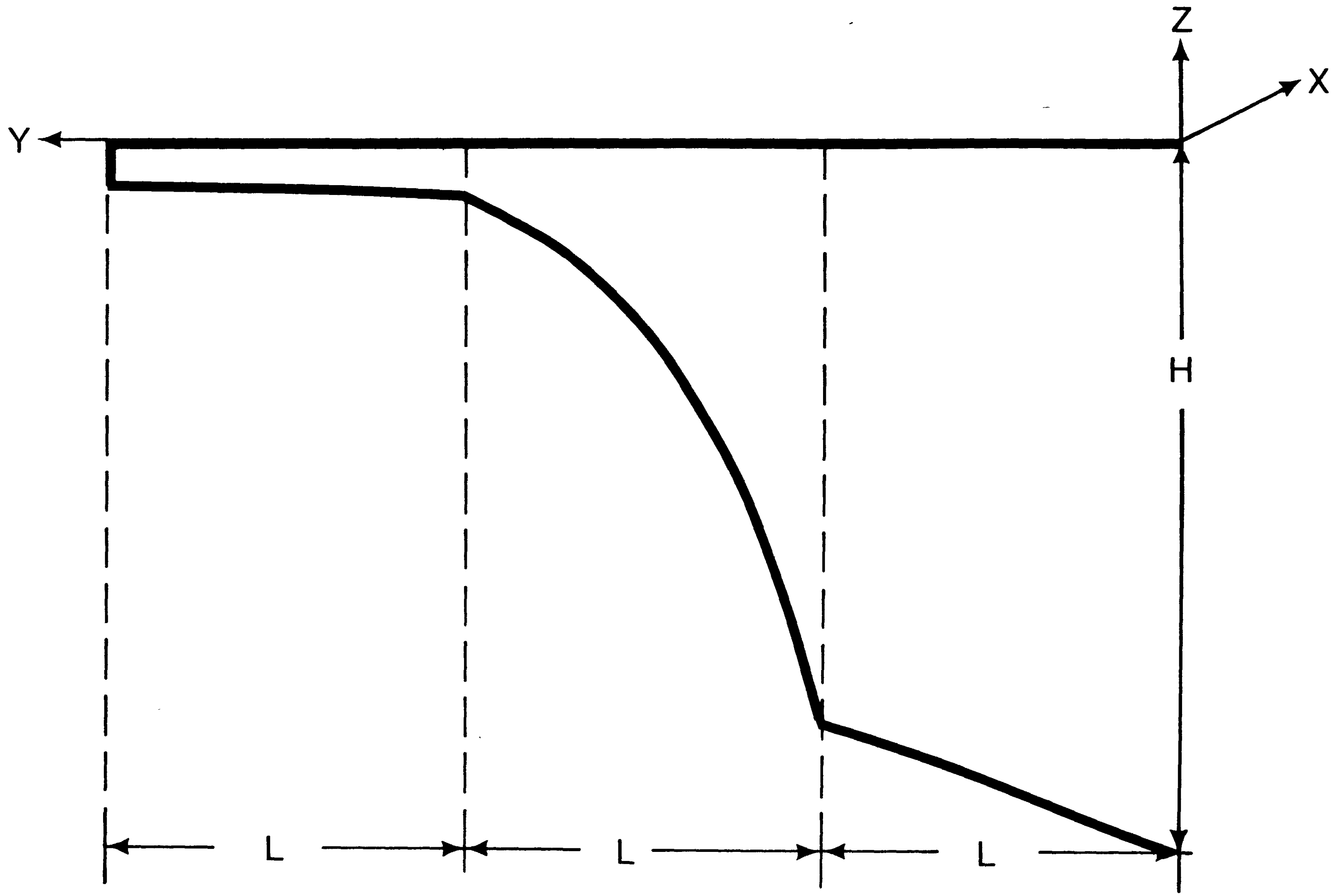

Figure 3.1. The geometry considered in the numerical model.

in the boundary conditions applied at the bottom and horizontal boundaries.

The bottom boundary condition we used is,

$$w = (-h_y)\cdot v + \frac{1}{2}E^{1/2}(v_x - u_y) \qquad \text{at } z = -h(y), \qquad (3.1)$$

where an Ekman suction velocity has been introduced to simulate the effect of friction. This is a simplification of Pedlosky's (1974) formula when bottom slope is small. In terms of p, (3.1) becomes

$$p_z = -\frac{S^2}{1-\sigma^2} h_y \left(p_y - \frac{k}{\sigma} p\right) - \frac{i S^2}{2\sigma(1-\sigma^2)} \cdot E^{1/2} \nabla^2 p \qquad \text{at } z = -h(y).$$

At the horizontal boundaries, we decompose the motions into Rhines' (1970) quasi-geostrophic modes in the following way,

$$p = \sum_{n=1}^{N} \left(I_n e^{-l_n y} + R_n e^{l_n y}\right)\cdot \cos m_n z \qquad \text{at } y = 0, \qquad (3.2)$$

and

$$p = \sum_{n=1}^{N} T_n e^{-l_n'(y-3)} \cdot \cos m_n' z \qquad \text{at } y = 3, \qquad (3.3)$$

where N is the number of grid points in the vertical, which is also the number of modes we can resolve. I_n, R_n, T_n are the incident, reflected, and transmitted wave amplitudes of the n^{th} mode, and l_n, m_n, l_n', m_n' can be either real or imaginary, and are determined by external parameters and local bottom slope through Rhines' solutions. In the model, I_n are specified, and R_n and T_n are unknowns. From this assumed form of solution at the boundaries, we can further impose the boundary conditions that

$$p_y = \sum_{n=1}^{N} (-l_n)(I_n - R_n) \cos m_n z \qquad \text{at } y = 0, \qquad (3.4)$$

and

$$p_y = \sum_{n=1}^{N} (-\ell_n') T_n \cos m_n' z \qquad \text{at } y = 3, \qquad (3.5)$$

to counter-balance the additional degrees of freedom introduced by the unknowns R_n and T_n. By defining $\vec{I}$, $\vec{R}$, and $\vec{T}$ as column vectors composed of elements of I_n, R_n and T_n, the above boundary conditions can be written in a matrix form, and can be fit into the general numerical scheme in a straightforward way.

With incoming waves specified at some offshore location on the continental rise, we can then study the evolution of the wave fields as they approach the coast.

3.2 The Numerical Solution

For a given topography, the independent nondimensional parameters are frequency σ, longshore wavenumber k, Burger number S, defined here as NH/fL, and the Ekman layer depth $E^{1/2}$. As a practical approach, we will first present the inviscid solution for what we think is a typical oceanic case. The solution will be discussed at some length to provide some insight into the underlying processes. This will then be followed by some discussion of parameter dependence and frictional effect.

3.2.1 An Example

For a typical oceanic case, let's choose the values of the dimensionless parameters (δ, k, S, $E^{1/2}$) = (.1, .8, 1., 0.). With H = 2.7 km, L = 45 km, and f = .94 x $10^{-4}sec^{-1}$, they correspond to the following dimensional values:

wave period $\sim$ 7.74 days,

longshore wavelength $\sim$ 353.25 km,

Brunt-Vaisala period $\sim$ 1.13 hrs,

kinematic viscosity $\sim$ 0. cm^2sec^{-1} .

The nondimensionalized depth h(y) on the continental rise, slope, and shelf are given by $e^{-.203y}$, h(1) $e^{-2.325(y-1)}$, and h(2) $e^{-.203(y-2)}$ respectively.

The pressure field for this case is shown in Fig. 3.2a, where the solid and dashed lines represent the contours of constant amplitude and phase respectively. The amplitude of the incoming wave has been set equal to 1 at the bottom at y = 0. This normalization procedure is also used for the velocity plots shown later. The reflection coefficients for this particular example are R_1 = .72, R_2 = .08, R_3 = .01 and are negligible for higher modes. This reflection gives a standing mode appearance to the wave field over the continental rise and slope which shows up in the undulation of the amplitude contours and the accompanying rapid phase change across the nodes. It is worthwhile to point out that a combination of

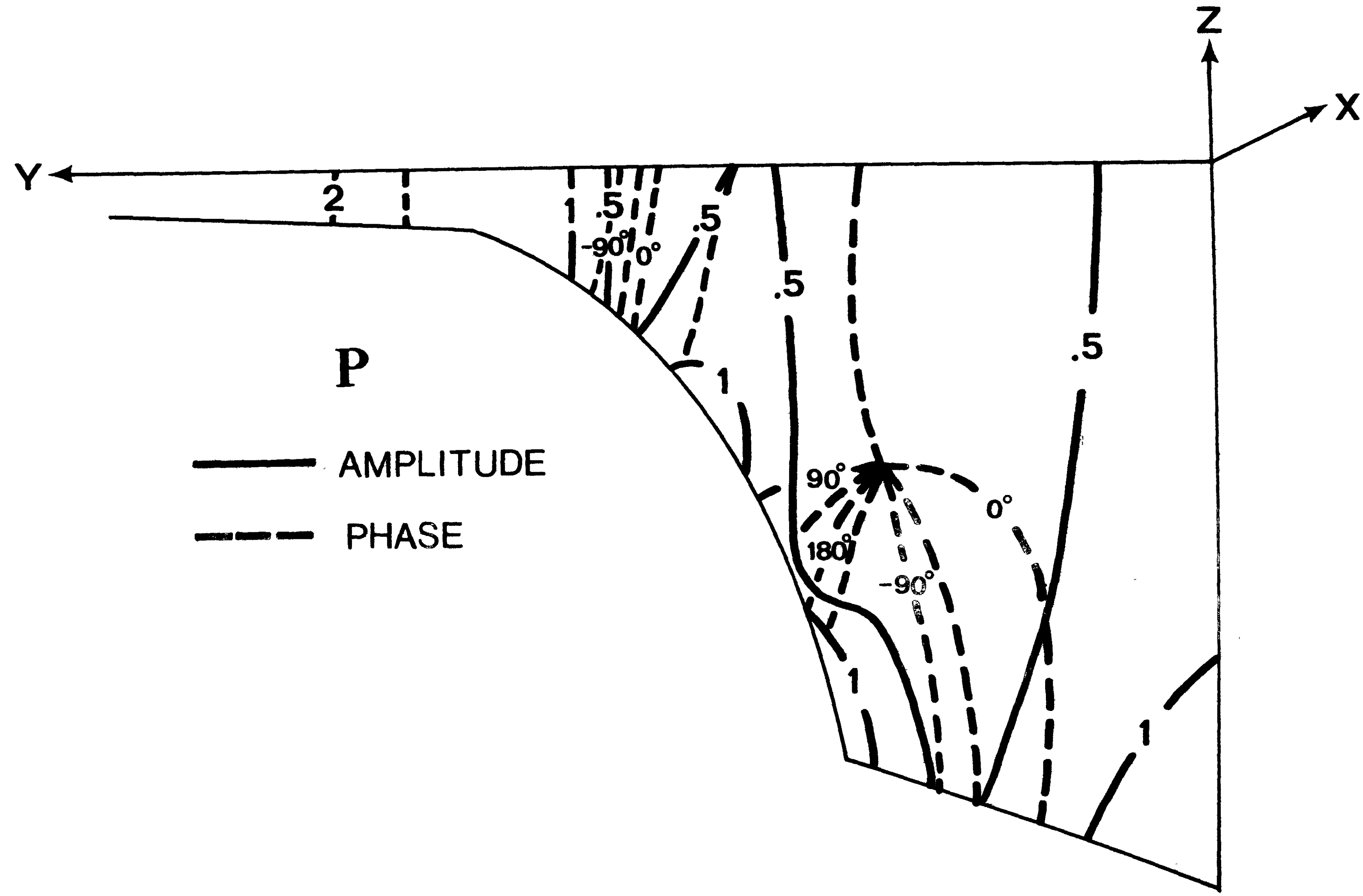

Figure 3.2a. Inviscid solution of pressure field p for the case $(\sigma, k, S) = (.1, .8, 1)$. Amplitude of the incoming wave has been normalized to 1 at the bottom at $y = 0$.

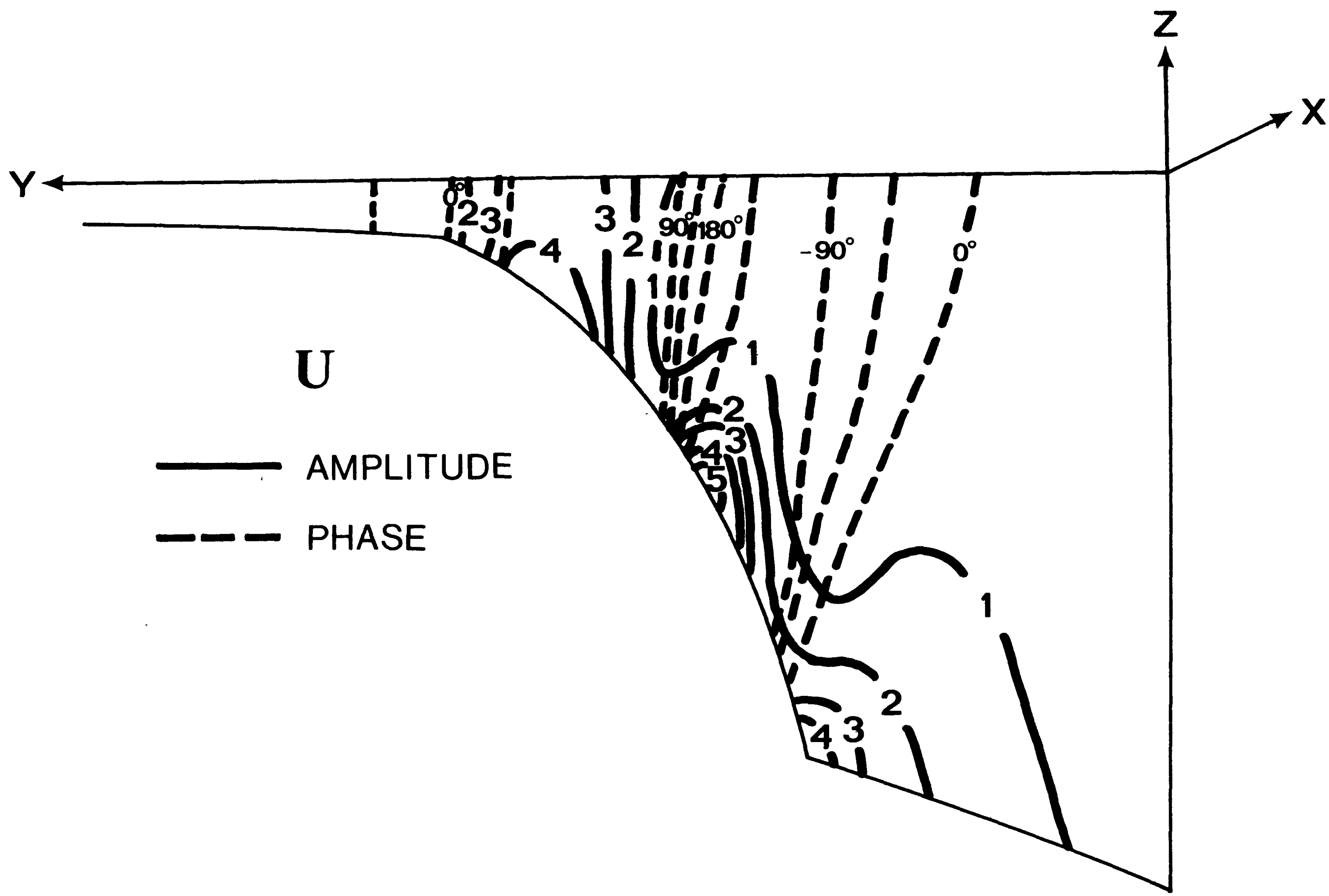

Figure 3.2b. Same as Fig. 3.2a, but for the longshore velocity u.

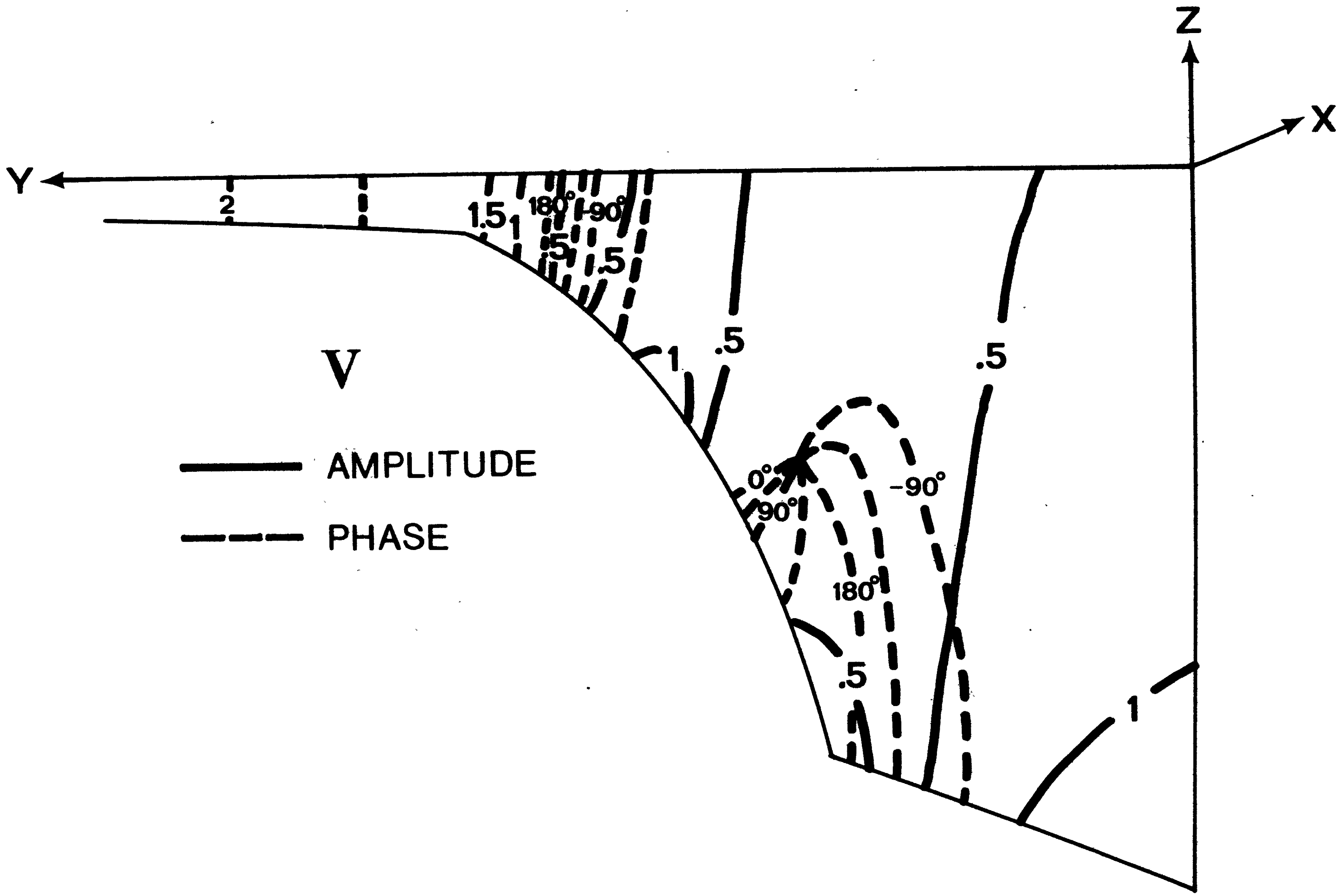

Figure 3.2c. Same as Fig. 3.2a, but for the onshore velocity v. The normalization factor is .56 if $|u| = 1$ at the bottom at $y = 0$ for the incoming wave.

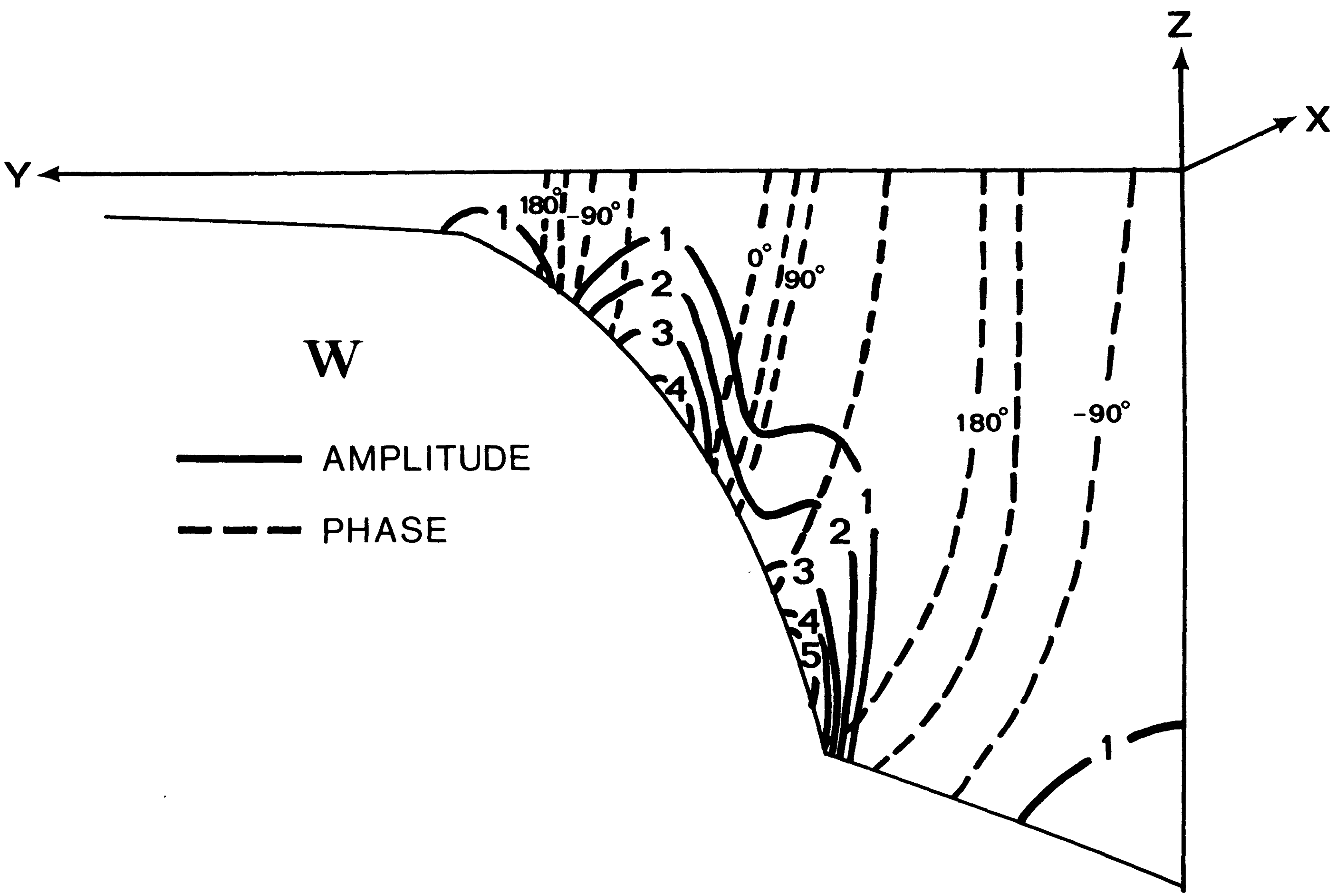

Figure 3.2d. Same as Fig. 3.2c, but for the vertical velocity w. The normalization factor is .11.

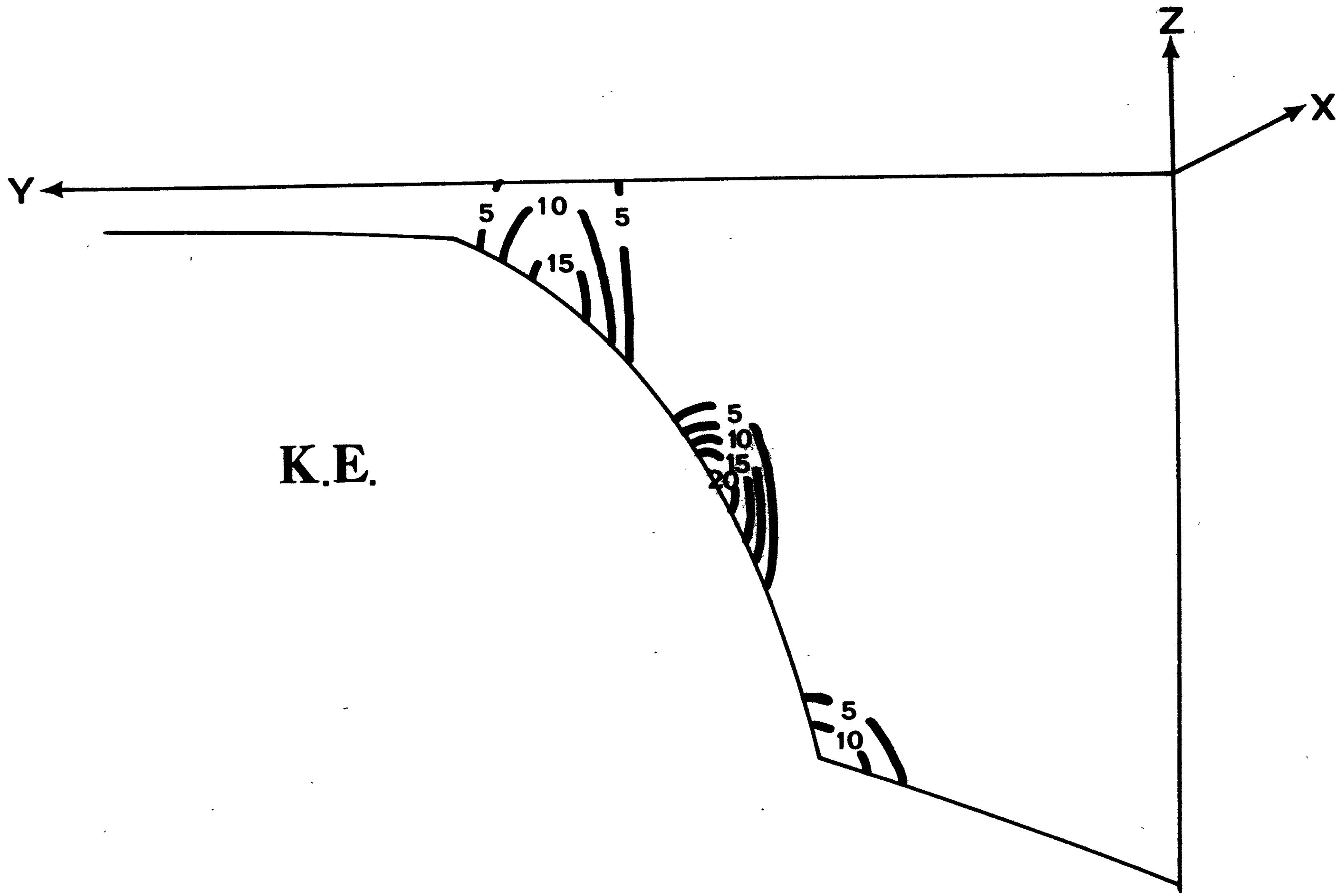

Figure 3.2e. Same as Fig. 3.2c, but for the horizontal kinetic energy. The normalization factor is .65.

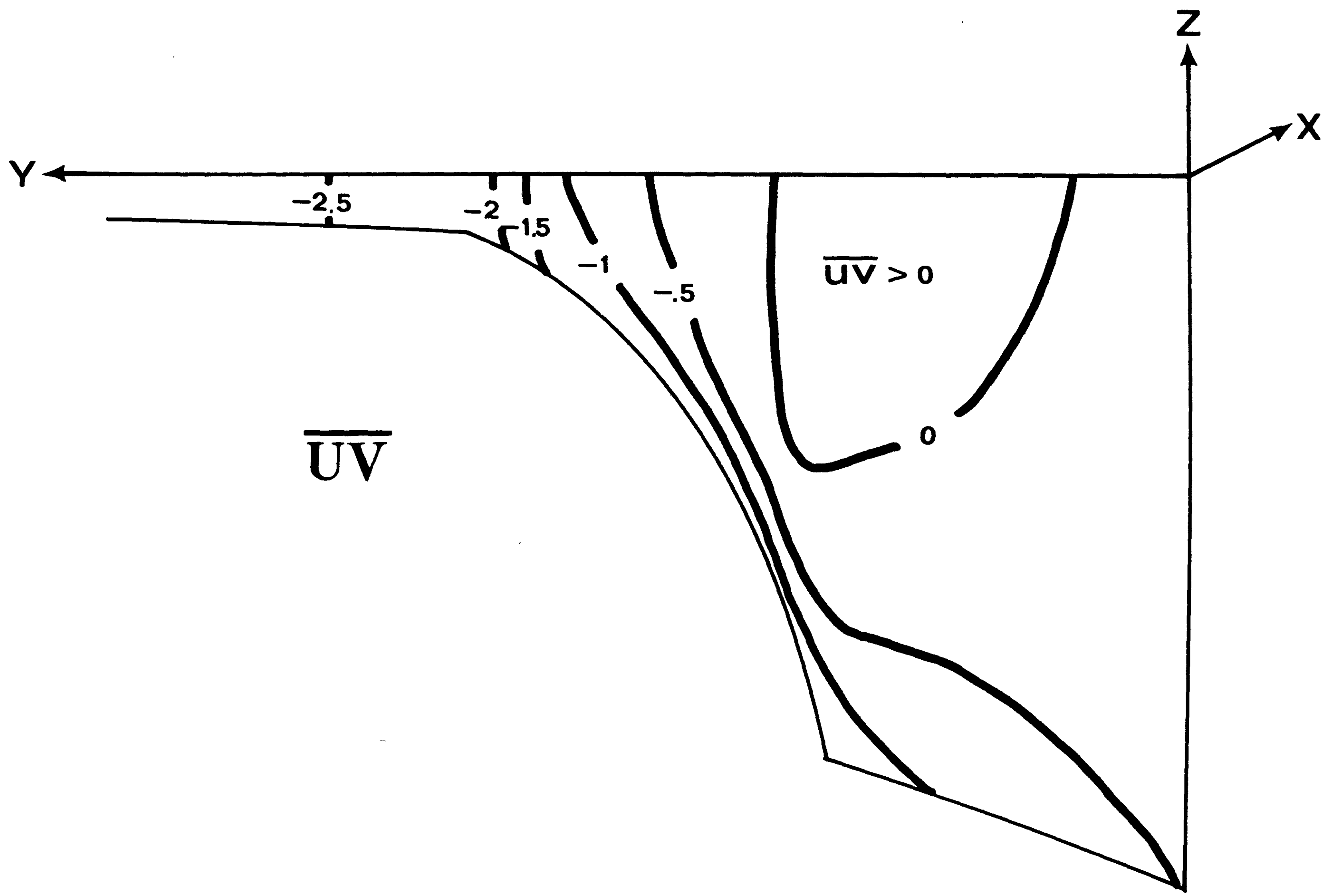

Figure 3.2f. Same as Fig. 3.2c, but for the Reynolds stress $\overline{uv}$. The normalization factor is .27.

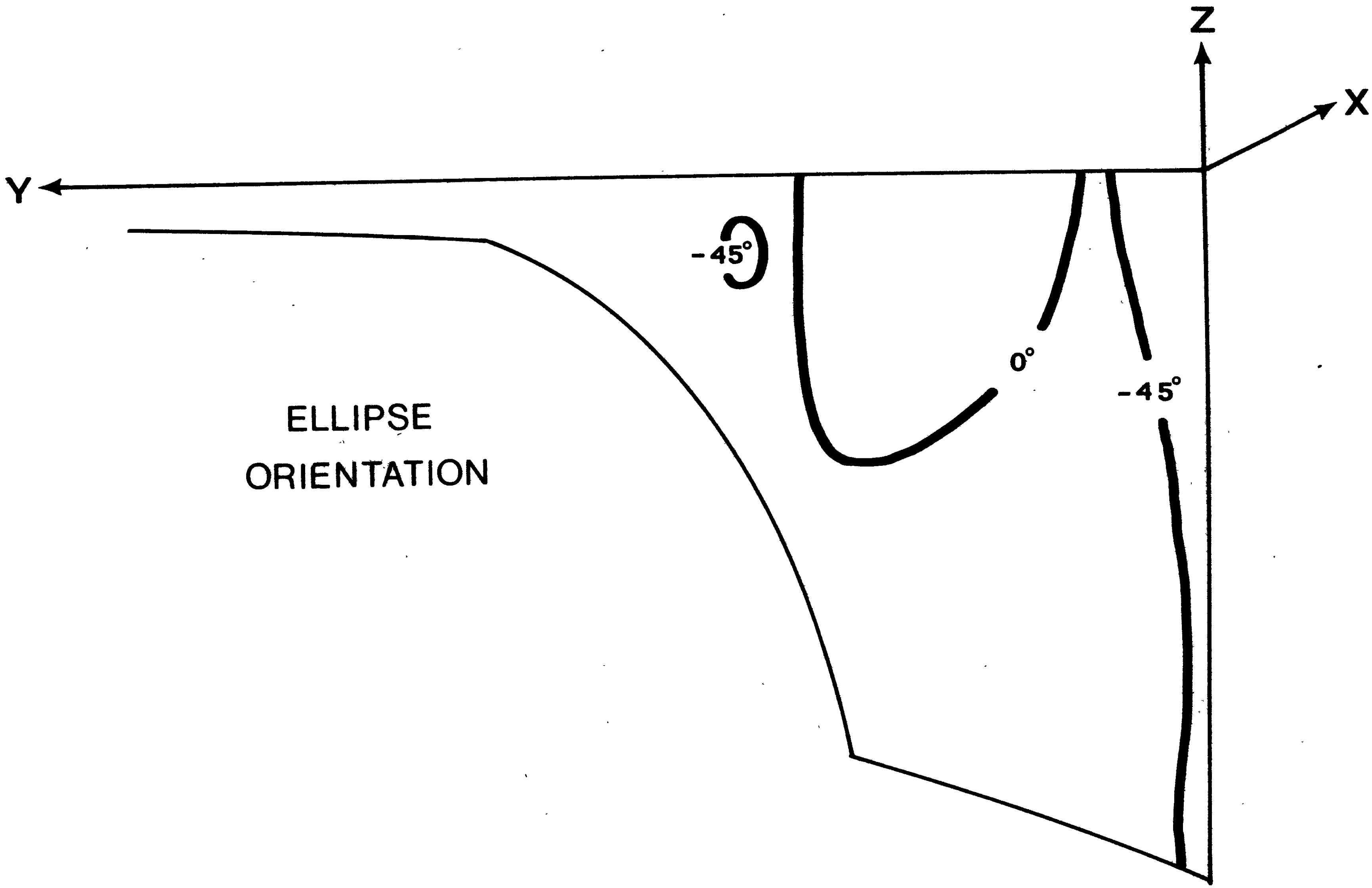

Figure 3.2g. Same as Fig. 3.2a, but for the ellipse orientation and no normalization has been done. The ellipse orientation is measured counterclockwise from the positive x-axis.

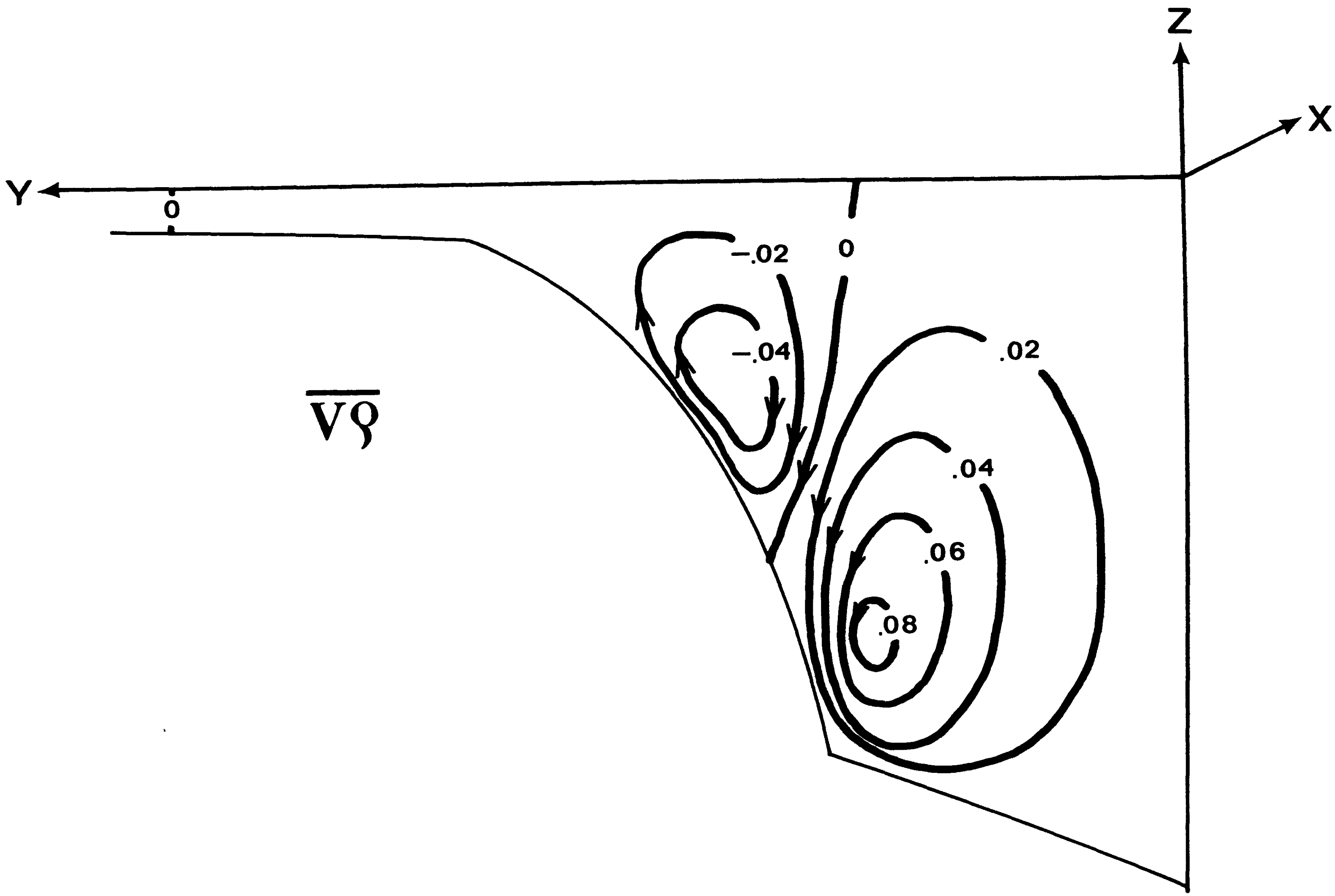

Figure 3.2h. Same as Fig. 3.2a, but for the onshore density flux $\overline{v\rho}$ and the magnitude has been normalized so that $|u| = 1$ at the bottom at $y = 0$ for the incoming wave.

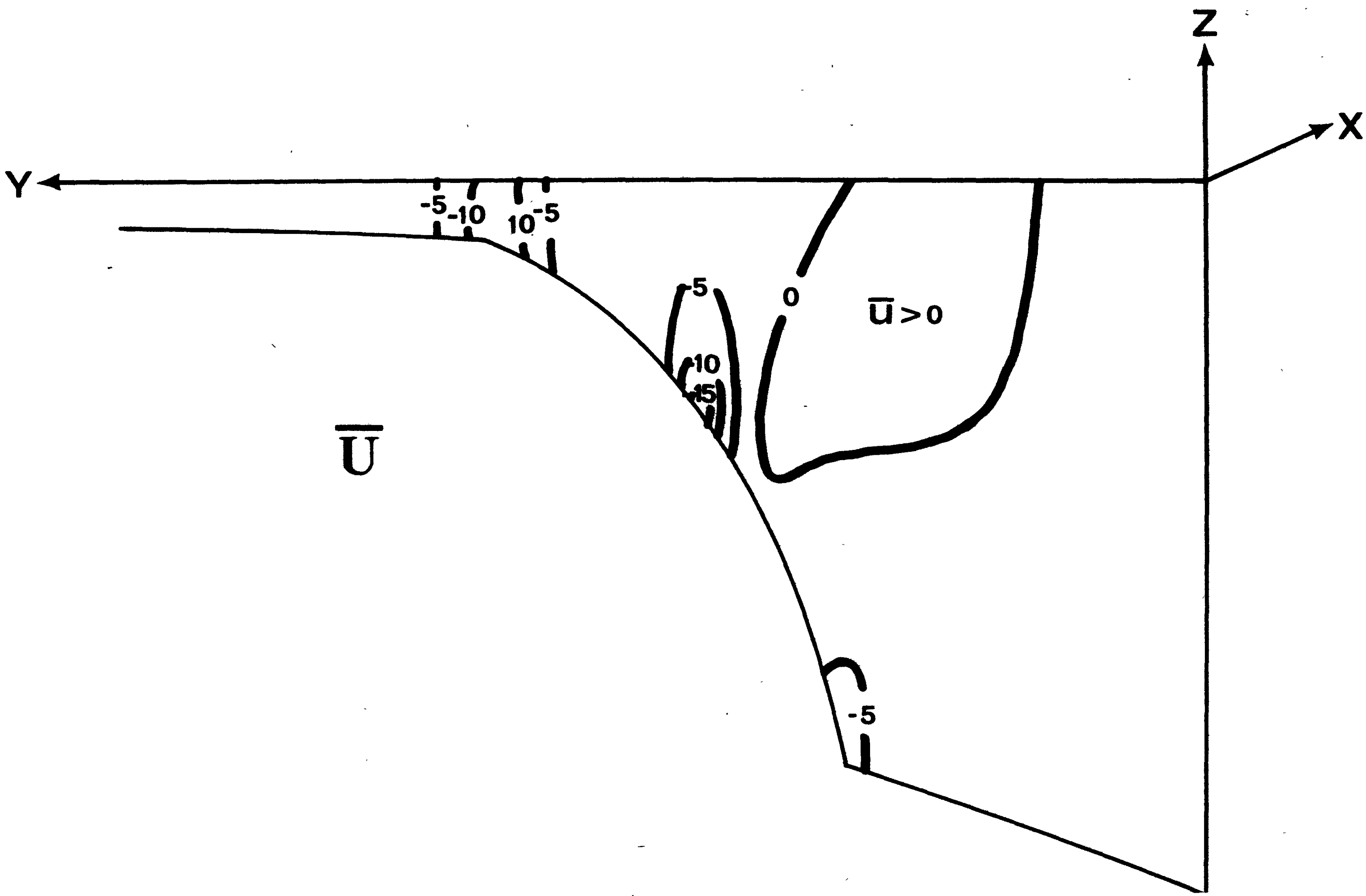

Figure 3.2i. Same as Fig. 3.2c, but for the longshore mean flow $\overline{u}$. The normalization factor is 5.1

the tilting of the phase lines and the presence of the standing mode can cause an apparent surface trapping of the wave amplitude. Away from the slope-rise junction, the basic horizontal and vertical scales as well as their spatial evolution can be understood from the earlier analysis of the solution in a wedge. For example, as the wave propagates into the slope region where the bottom slope is greater, the bottom trapping is intensified, accompanied by the reduced horizontal scales. As it approaches the shelf break, where the effect of the rigid surface dominates, the motion becomes more barotropic and the phase lines become more vertical. As the wave enters the shelf region, the wavelength increases again and the motion is virtually uniform throughout the water column. There are, however, some new features associated with this numerical solution. First of all, we notice that the standing mode component of the pressure field has an anti-node located at the shelf break. This is a trivial result caused by the assumption that the waves are allowed to propagate freely through the inshore boundary at y = 3. The justification for this assumption lies partly on the vanishing depth at the coast which serves as an efficient energy sink by either refracting the ray paths (Smith, 1971; Rhines, 1971) or increasing the frictional damping there. The existence of an anti-node in the pressure field at the shelf break also implies a sharp drop in the kinetic energy level across the shelf break as will be seen later.

Another striking feature in Fig. 3.2a is the formation of an amphidromic point over the slope-rise junction, indicating that some locally trapped baroclinic motions are generated there.

Suarez (1971) has discussed the excitation of these baroclinic modes over a small slope discontinuity. He shows that these "fringe" modes are necessary to match the bottom-intensified waves across the slope discontinuity. Since his analysis is valid only when the bottom slope is small and hence the solution is separable in the horizontal and vertical directions, we will use it to study the effect of baroclinic fringe modes on the phase propagation of the bottom-intensified waves over the continental rise. Let's assume that over the continental rise the bottom slope is small and the solution can be approximated by a superposition of an incoming bottom-intensified wave and a first baroclinic mode that decays away from the slope-rise junction,

$$p \sim I\, e^{-ily} \cosh(mz) + C\, e^{l'y} \cos(\pi z), \qquad (3.6)$$

where the origin of y has been moved to the slope-rise junction for convenience; l, m, l' are postive quantities, and I is assumed real and positive without loss of generality. To match the bottom-intensified component of p across the slope-rise junction, C must be real and negative. The phase of p is given by

$$\theta_r \sim \tan^{-1}\left\{ \frac{-I \sin ly \cosh mz}{I \cos ly \cosh mz + C e^{l'y} \cos \pi z} \right\}, \qquad (3.7)$$

which, in the absence of the baroclinic mode, is simply a linear function of y, shown by the straight line in Fig. 3.3. But with $C < 0$, it's deflected from the straight line in opposite directions depending on whether we are above or below the mid-depth. This apparent upward propagation will rotate the phase lines counterclockwise, pivot them against the mid-depth point. The effect may be negligible near the bottom where the bottom-intensified mode is dominant. While the numerical solutions are more complicated, there is some indication in Fig. 3.2a that this basic effect is operating.

The velocity fields are plotted in Fig. 3.2b-d. It is seen that $|v|$ and θ_v are very similar to that of p while the contours of $|u|$ are shifted a quarter of a wavelength from that of $|p|$, and hence has a node at the shelf break, as is expected for quasi-geostrophic motions. There are, however, some modifications caused by various factors, the detailed analysis of which are both difficult and of no practical importance as these patterns depend very much on the external parameters. Instead, we will try to deduce next some more general results that might be useful for data interpretation.

First, we notice that $|u|$ is generally much larger than $|v|$ over the slope, consistent with the analytical solution in a wedge. And since the kinetic energy is dominated by the longshore velocity, the kinetic energy contours shown in Fig. 3.2e mimic the $|u|$ contours. Therefore the kinetic energy level is

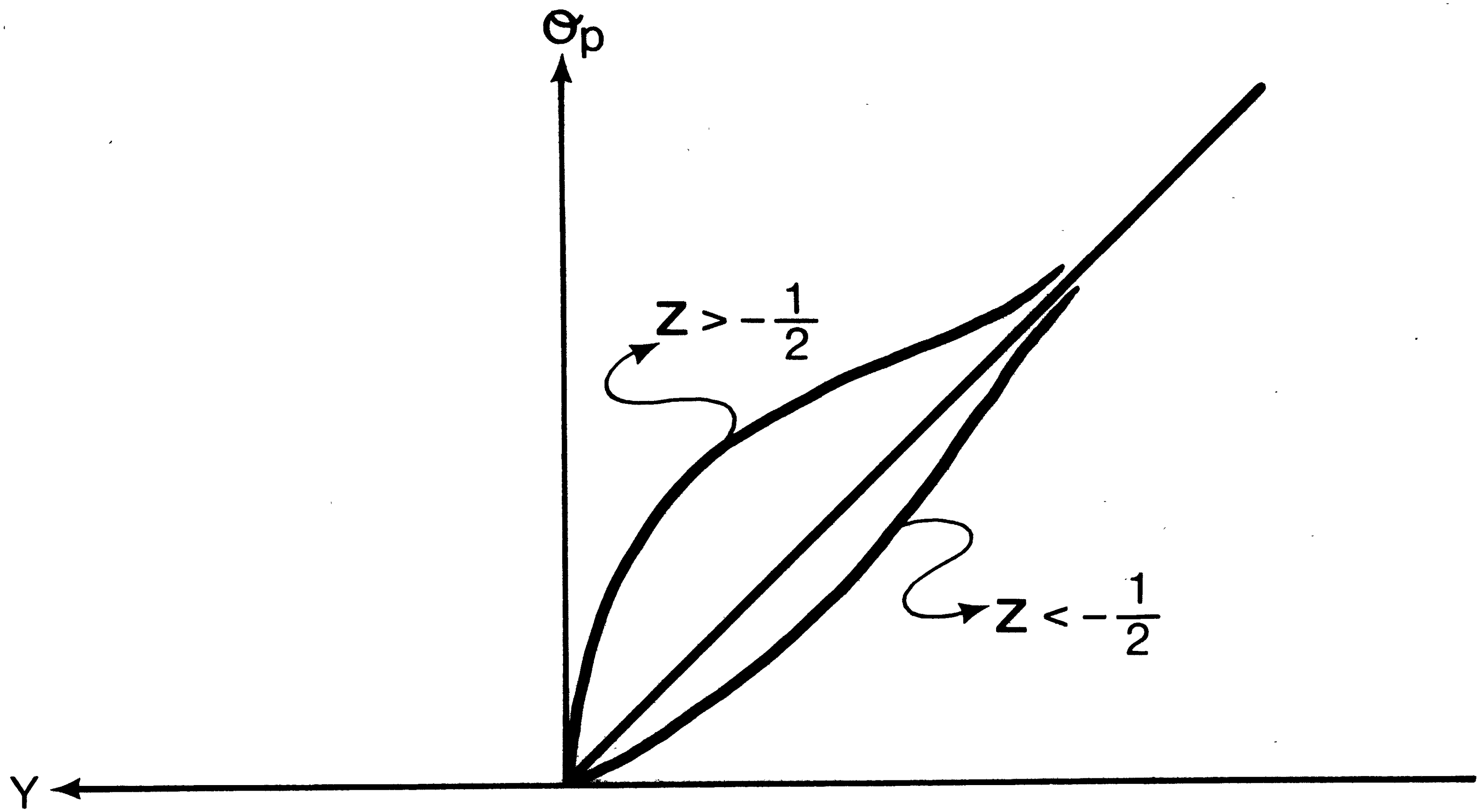

Figure 3.3. The effect of the first baroclinic mode on the phase propagation of the pressure field over the continental rise.

much higher over the slope region and drop rapidly across the shelf break.

Similar expressions as (3.7) can be derived for the velocities by assuming quasi-geostrophy. It is trivial to show from these expressions that the phase lines of u and w are tilted in opposite directions from that of p and v. This is clearly shown in Fig. 3.2a-d.

The Reynolds stress $\overline{uv}$ is plotted in Fig. 3.2f, where $|u|$ has been set equal to one at the bottom at $y = 0$. The basic structure is similar to that of a wave in a wedge shown in Fig. 2.13e, except in the region near the slope-rise junction where the baroclinic fringe waves become important. As these waves tilt the phase lines of u and v in opposite directions, the magnitude of the Reynolds stress is reduced, and in the extreme case when the amphidromic point is formed in p, it changes sign altogether above the amphidromic point. The orientation of the major axis of the current ellipse (measured counterclockwise from the positive x-axis) is plotted in Fig. 3.2g, indicating that the ellipse orientation shifts from the II-IV quadrant into the I-III quadrant above the amphidromic point, consistent with the Reynolds stress distribution.

Density flux $\overline{v\rho}$ is plotted in Fig. 3.2h with the same normalization factor as that for $\overline{uv}$. Again, over the slope region, it agrees with that of a wave in a wedge shown in Fig. 2.13i, but on the continental rise, it is of a different sign.

From our discussion earlier, we see that over the continental rise the baroclinic fringe waves tend to shift the phase lines of v toward the coast above some mid-depth point, while that of w in the opposite direction. This implies that the phase difference between w and v or the θ_{wv} in equation (2.43) lies in the first two quadrants. Therefore, $\overline{v\rho}$ is negative from (2.44) and the heat flux is offshore. This is unlike over the continental slope, where the effect of the rigid surface dominates and θ_{wv} lies in the third quadrant.

Since the cross-shelf mean flow follows the heat flux contours as discussed earlier, it is plotted in this same figure with its direction indicated by the arrows. Therefore, the mean cross-shelf circulation is comprised of two counter-rotating gyres with a more concentrated downwelling occuring near the slope-rise junction and a more diffused upwelling occuring on both sides of it.

The longshore mean flow $\overline{u}$ is plotted in Fig. 3.2i which has been normalized to unity for the incoming wave along the bottom at y = 0. Again, it agrees with that of a wave in a wedge shown in Fig. 2.13j except the direction reverses locally above the amphidromic point. This can be explained by the domination of baroclinic fringe waves there. If we neglect the second term on the right in equation (C.6) near surface, then in the present coordinate system,

$$\overline{u} \sim \frac{1}{\sigma}\left(i\overline{u_y \cdot v} - k\overline{v^2}\right). \qquad (3.8)$$

For quasi-geostrophic motions,

$$u \sim -\, p_y,$$

$$v \sim -\, ikp,$$

(3.8) then becomes

$$\overline{u} \sim \frac{k}{\sigma}\overline{(p_{yy} - k^2 p)\cdot p}. \qquad (3.9)$$

Since the baroclinic modes are exponentially decaying in y with an e-folding length shorter than k^{-1}, $\overline{u}$ can be positive when these modes dominate.

3.2.2 Parameter Dependence

The horizontal and vertical scales of the motion depend of course very much on the external parameters, which in turn affect the intensity of the baroclinic fringe waves generated and/or the magnitude of the reflection coefficient. The effect of changing parameters on the scales of the motion can be qualitatively inferred from the solution of the bottom-intensified quasi-geostrophic waves over a small slope (e.g., Suarez, 1971)

$$p \sim \cosh(m'z)\, e^{-i(kx+ly+\sigma t)}, \tag{3.10}$$

where

$$m' = \sqrt{k'^2 + l'^2}, \tag{3.11}$$

with

$$(k',l') = S(k,l), \tag{3.12}$$

and the frequency scaled by the short wave cut-off frequency fS·(bottom slope) is given by,

$$\sigma' = \frac{|k'|}{m' \tanh m'} \tag{3.13}$$

We plot in Fig. 3.4 (Suarez, 1971), the contours of constant σ' (solid lines) and m' (dashed lines), as a function of the scaled wave numbers k' and l'. These dispersion curves have been discussed in some detail by Suarez. For our purpose, we only want to mention that, given σ, k and S as independent external parameters, the vertical and cross-shelf scales are determined through the values of m' and l' which can be predicted from the figure. For example, the motions with larger σ or

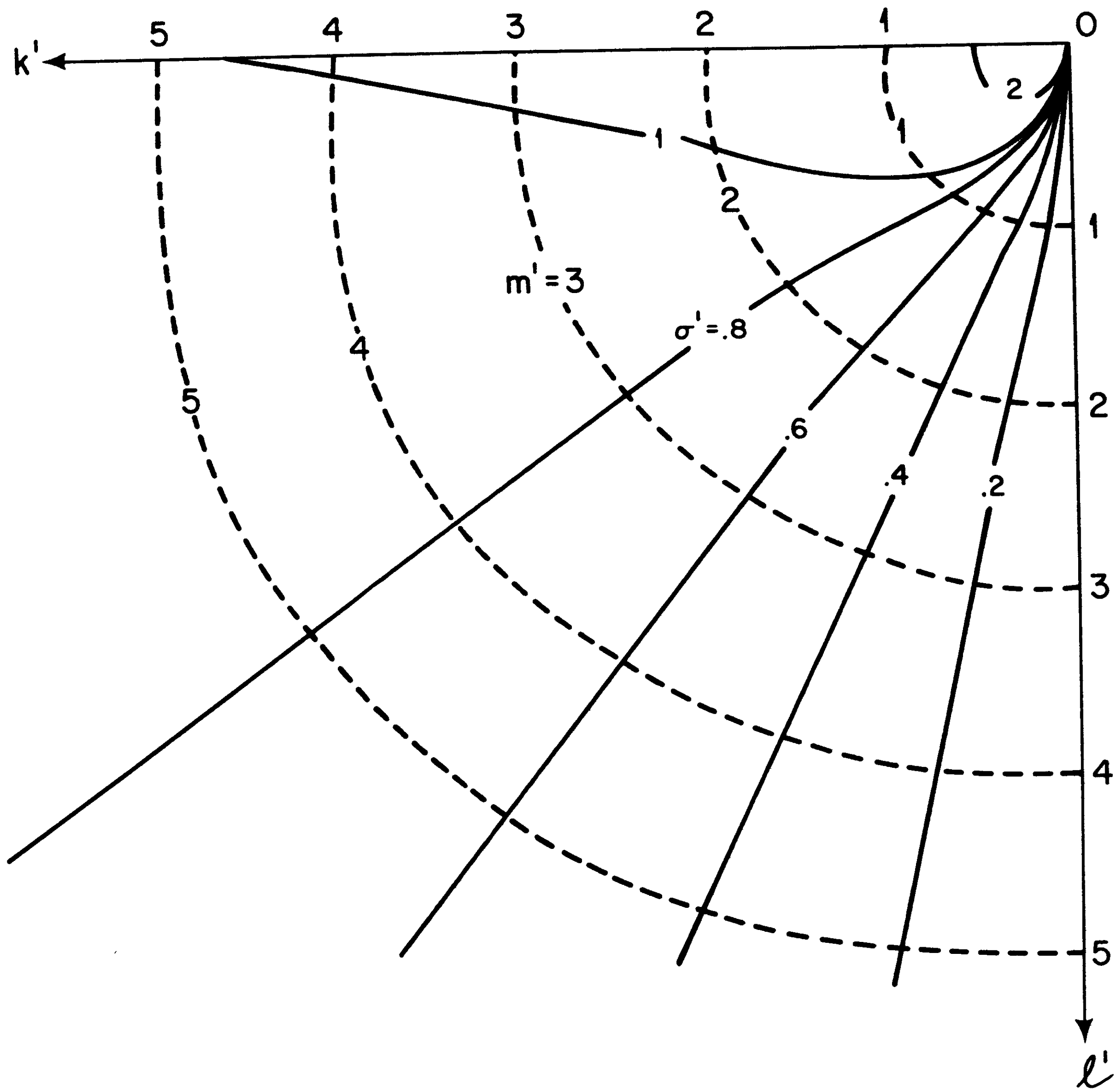

Figure 3.4. Contours of the scaled σ' (solid lines) and m' (dashed lines), as a function of the scaled wave numbers k' and l', for the bottom-intensified, quasi-geotrophic waves.

smaller k and S generally have larger vertical and cross-shelf scales, and vice versa. Apart from the complications which arise in our model, this qualitative behavior generally still holds. There are, however, some additional features associated with this change of scales. Rhines (1969) has discussed the analog of Ramsauer effect in his study of the reflection of barotropic, topographic Rossby waves from a sloping step, which states, in essence, that if an integral number of half-wave-length can be fit into the slope region, then it poses no obstacle to the transmission of these waves, despite the rapid change of the medium. This effect is well displayed in Fig. 16 of Kroll and Niiler (1976), where the energy flux transmission coefficcient has peaks for certain values of k when the above condition is satisfied. In Fig. 3.5, the stratified version of this figure is plotted for δ = .1 where the open and solid circles represent the numerical calculations for S = .1 and 1., respectively, and the lines joining them are just freehand. Besides changing the location of the peaks which can be roughly estimated from Fig. 3.4, the increased stratification also reduces the height of the peak for the shorter waves. This is because the increased vertical mis-match for the shorter waves of the bottom-intensified mode across the slope-rise junction excites more vigorous baroclinic fringe waves and reduces the transmission coefficient (Suarez, 1971). The maximum energy

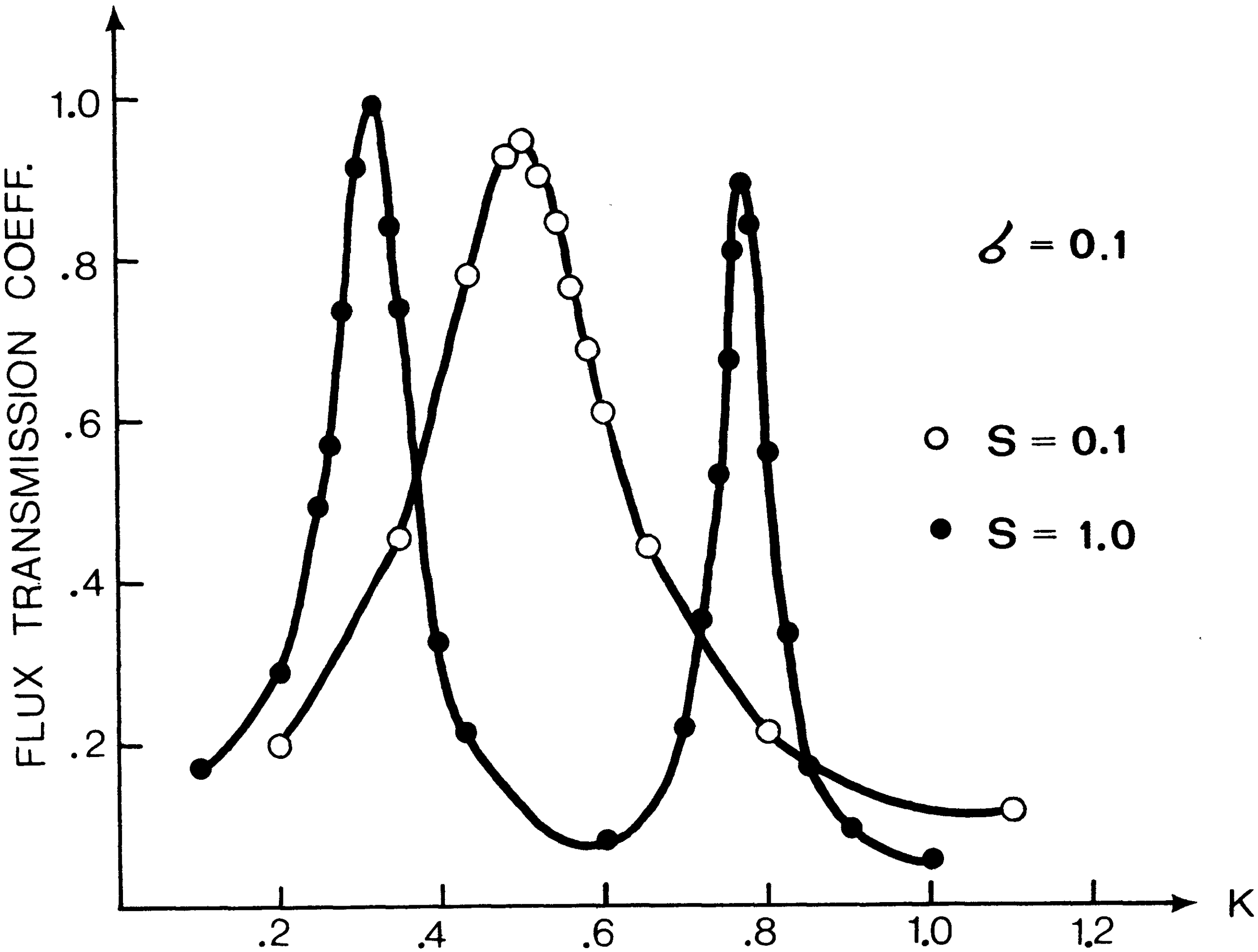

Figure 3.5. Curves of energy flux transmission coefficient as a function of k for $\sigma = .1$, with S = .1 and 1.

flux transmission coefficient obtained by Kroll and Niiler in their barotropic model is therefore an upper bound, and can be significantly reduced for short waves. The varied strength of the baroclinic fringe waves would certainly affect some of the wave properties discussed earlier. The effect is straight-forwrd and need not be discussed here.

3.2.3 Frictional Effect

Friction, of course, dissipates the waves, and reduces the wave amplitude from that of the inviscid case. But since at a given point, the amplitude of the reflected waves has suffered more from this dissipation because of the additional distance they have traveled, the propagating component actually increases relative to the standing component. This would increase the magnitude of the heat and momentum flux, at least near the source region until eventually the overall dissipative effects overtake some distance farther up the slope. We plotin Fig. 3.6a-c, the pressure field p, the Reynolds stress $\overline{uv}$ and the onshore density flux $\overline{v\rho}$ when ν (kinematic viscosity coefficient in the bottom Ekman layer) equals 22 $cm^2 sec^{-1}$. Comparing with the inviscid solutions shown in Fig. 3.2a, f, and h, the greater propagating component in the pressure field and the accompanied greater values of $\overline{uv}$, $\overline{v\rho}$ offshore are evident. It is also seen that the friction induces a positive density flux along the bottom. This can be explained by the following derivation. Since we only need to know the relative phase between the various variables to determine the sign of their correlations, the symbol "$\sim$" used below implies that "the phases on the two sides of this symbol are approximately equal".

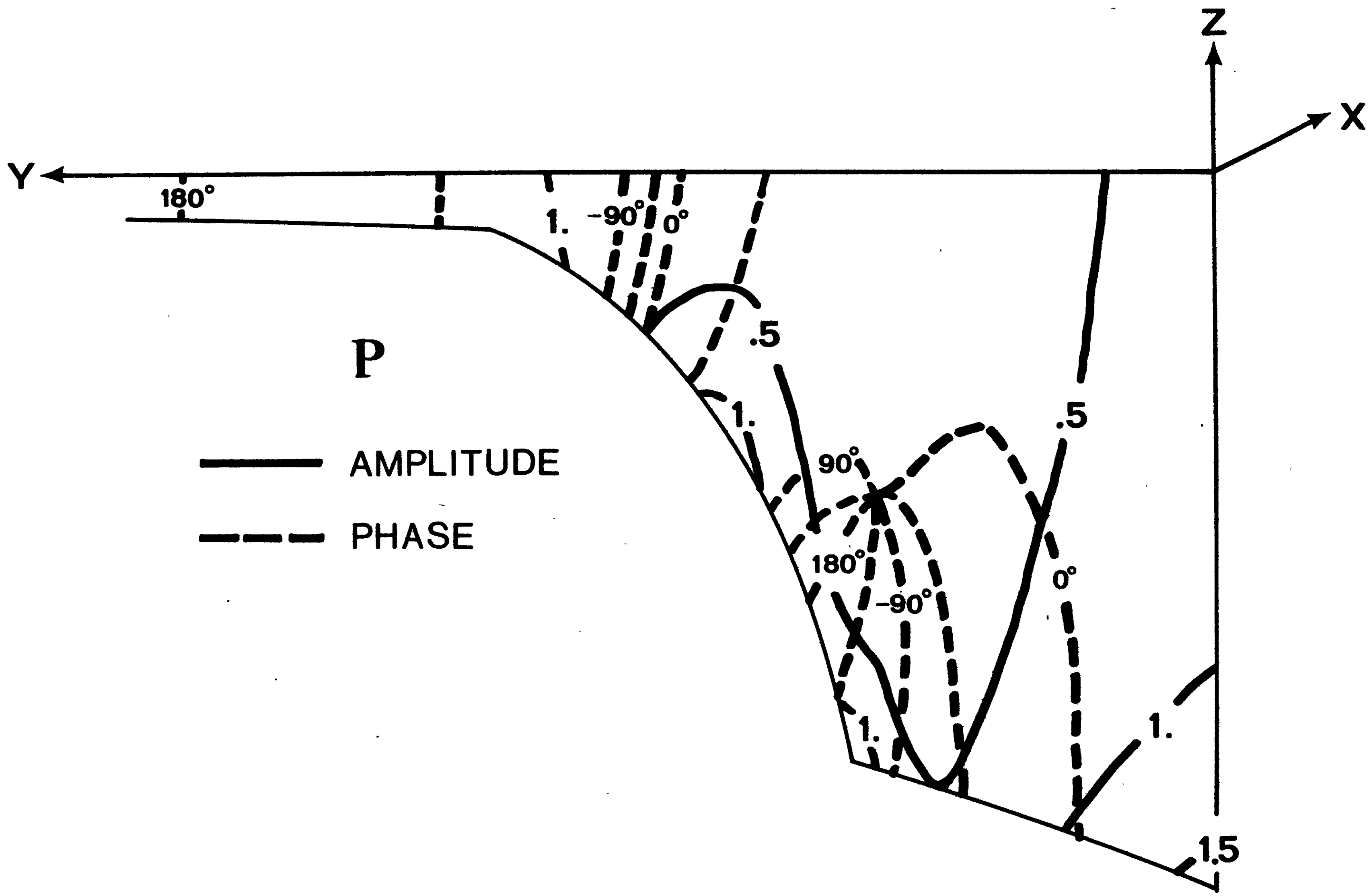

Figure 3.6a. Same as Fig. 3.2a, but with ν (kinematic viscosity coefficient) set to 22 cm²/sec.

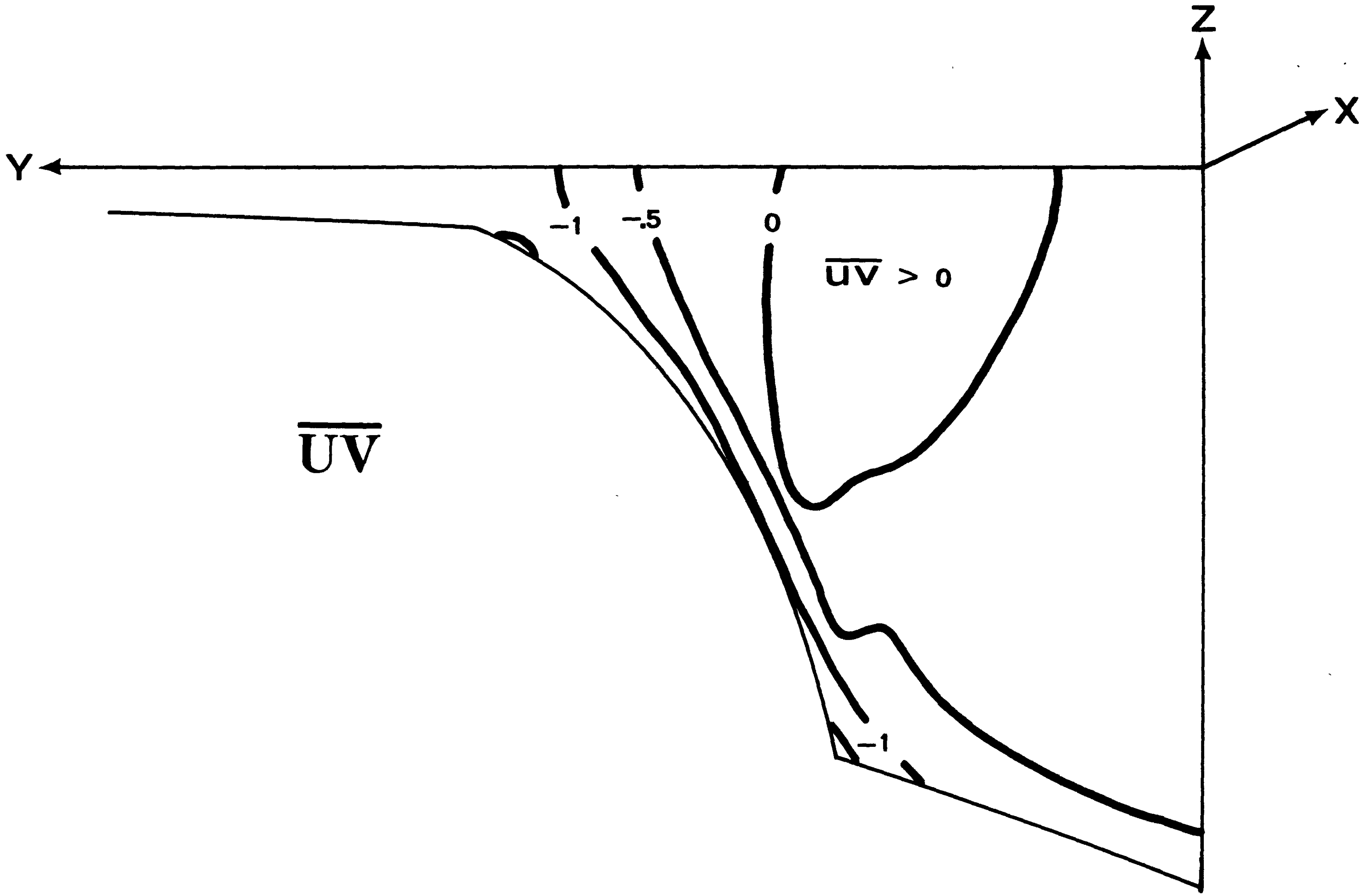

Figure 3.6b. Same as Fig. 3.2f, but with ν set to 22 $cm^2 sec^{-1}$.

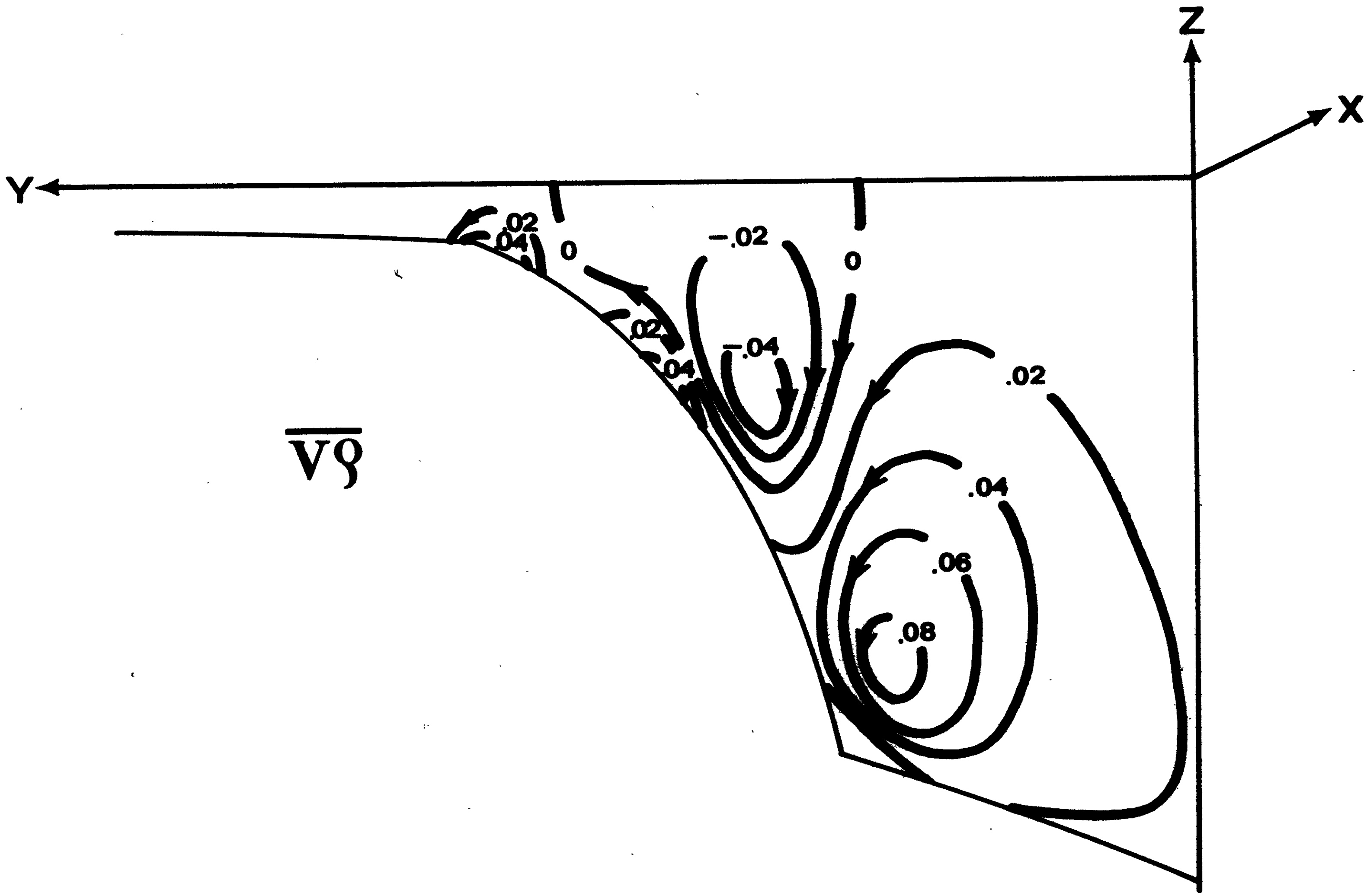

Figure 3.6c. Same as Fig. 3.2h, but with ν set to 22 $cm^2 sec^{-1}$.

Now that,

$$v_x - u_y \sim p_{yy} - k^2 p$$

$$\sim - p_{zz} \qquad \text{(from (2.7))}$$

$$\sim - p \qquad \text{(assuming that the bottom-intensified mode dominates near the bottom)}$$

$$\sim - iv, \qquad \text{(assuming quasi-geostrophy)}$$

(3.1) implies

$$w \sim (- h_y - i\mu)\, v,$$

where μ is some real and positive constant. Hence, θ_{wv} of (2.43) lies in the third or fourth quadrant and $\overline{v\rho} > 0$ from (2.44).

3.3 Summary

Although still much simplified, this numerical model retains the essential elements of stratification and finite slope changes. Apart from the excitation of baroclinic fringe waves near the slope-rise junction and the modification caused by friction, many of the results can be explained by the analytical theory of a wave in a wedge. This is especially true over the slope region, where the modification caused by these baroclinic fringe waves is minimal, because of their more locally confined influence and their dominance by the much more vigorous bottom-intensified waves. Without undue repetition, readers are referred to the last section of Chapter 2 for a proper summary of the wave properties over the slope region in a frictionless model.

The replacement of the apex of a wedge by a finite shelf where the waves are allowed to propagate freely through, introduces at the shelf break a node in the longshore velocity field which accounts for the rapid drop of kinetic energy across the shelf break. The baroclinic fringe waves excited near the slope-rise junction in the presence of finite slope change can form an amphidromic point at some mid-depth and reverse the direction of phase propagation above it.

On the continental rise, the baroclinic fringe waves shift the phase lines of u and w in opposite direction from that of p and v, pulling the latter toward the coast above some mid-depth point where their effect is the most pronounced. This generates an offshore heat flux over the continental rise and reverses the cross-shelf mean flow predicted in an infinite wedge. The longshore mean flow generally points to the left facing the shoreline, but its direction can be reversed where the baroclinic fringe waves dominate.

Changing the values of the external parameters would of course change the horizontal and vertical scales of the motion which in turn change the intensity of the baroclinic fringe waves generated and/or the reflection coefficients. The excitation of the baroclinic fringe waves generally reduces the transmission coefficient, especially for shorter waves, and hence the maximum energy transmission coefficient obtained in Kroll and Niiler's barotropic model is likely an upper bound. Friction, besides its overall dissipative effect, can increase the magnitude of the Reynolds stress $\overline{uv}$ and cross-shelf heat flux near the source region by reducing the amplitude of the reflected waves. Friction also generates an offshore heat flux near the bottom and hence modifies somewhat the cross-shelf mean flow pattern in an inviscid model.

4. Application of the Model

Observational work by Thompson (1977) and others has demonstrated that over the continental rise south of New England the low frequency motions below the thermocline can be described by linear topographic Rossby wave dynamics. Furthermore, the observed phase propagation is consistent with the assumption that these waves are generated offshore and radiate their energy shoreward onto the coast. To study the dynamical implications of these waves as they approach the shelf, Beardsley, Vermersch and Brown conducted an experiment in 1976 (called NESS76) to obtain long-term, simultaneous measurements of current, temperature, and bottom pressure across the New England continental margin. The setup of the moored instruments is shown in Fig. 4.1, which, according to their locations, will henceforth be referred to as shelf (NE2,2W), slope (NE3,3W) and rise (NE4,5) stations, separated by the 200 and 2000 m isobaths. Except for the loss of the moorings at NE3B and 3E, the loss of the rotor at 32 shortly after deployment, and a rotor fouling at NE21 and 22 that cut short the data, the data last about six months. The detailed analysis of the data will be presented elsewhere (Beardsley, Ou, and Brown, in preparation), and only some relevant observations will be discussed here to check their consistency with the model predictions.

Since the detailed spatial distribution of many of the wave

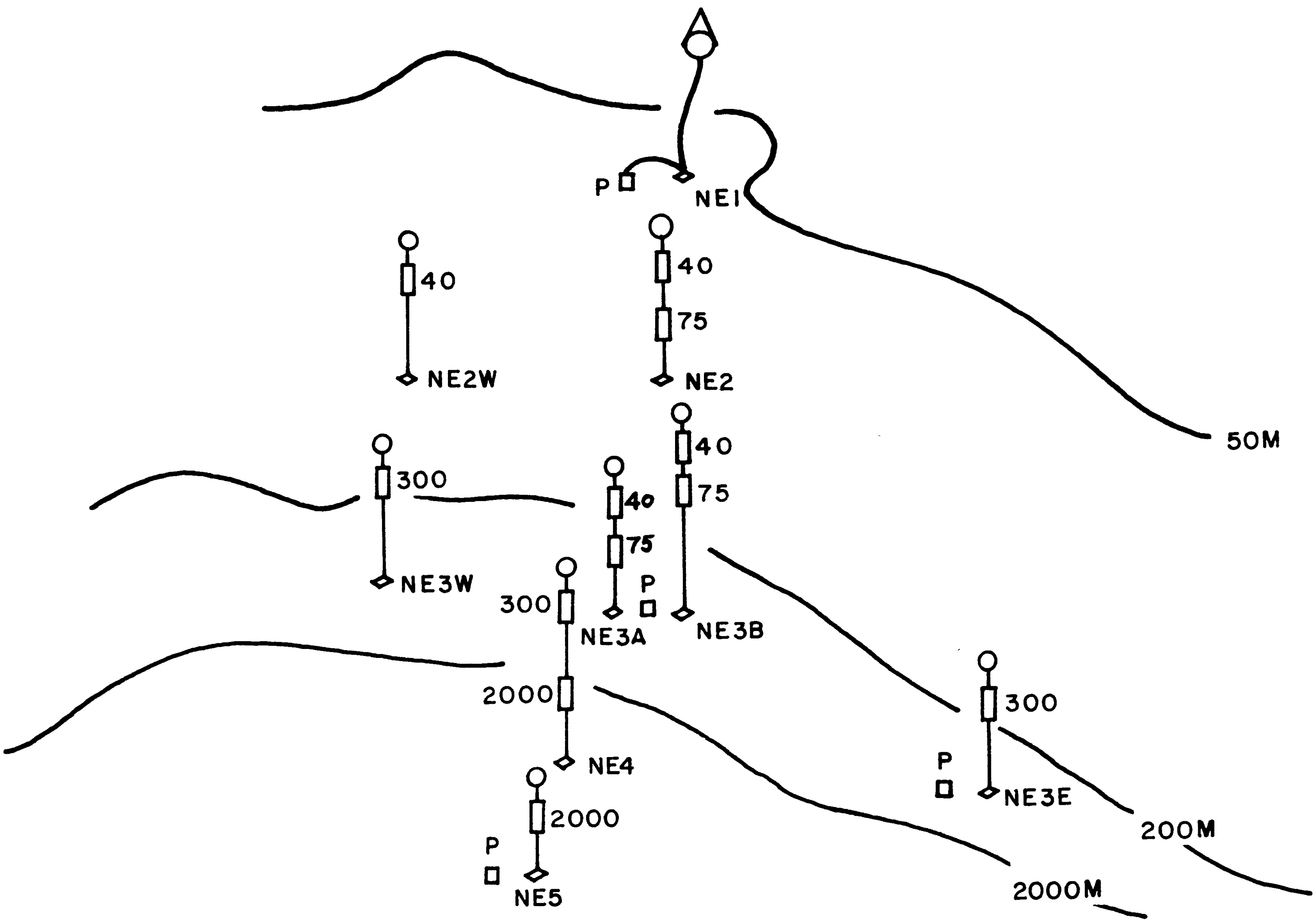

Figure 4.1. The setup of the moored arrays of NESS76. Shelf, slope and rise stations are separated by the 200 and 2000 m isobaths.

properties predicted by the model depend on the longshore wave number, our inability to isolate the motions of different longshore scales and the sparse spatial coverage across the transect seriously limit our ability for a more detailed comparison. Hence, only the two major predictions that are the least scale-dependent will be compared here with the data.

4.1 Comparison with Observations

The kinetic energy and temperature spectra are shown in Fig. 4.2 for all the available data. In the energy spectrum, the energy levels for the three stations have been displaced one decade apart, and the light shading with a "-2" slope for periods shorter than 14 days is plotted to assist visual comparisons. As are typical of all oceanic observations, the spectrum is generally red for sub-inertial motions. The smaller spectrum slope as we move toward shallower depths is presumably caused by the increasing wind effect which tends to fill in the energy at the intermediate range. The break of the slope at about 14 days for the instruments 42 and 51, which also shows up clearly in the temperature spectrum, is consistent with Thompson's observations near Site D, and has been attributed to the short wave cut-off which is of the order of $2\pi/(10$ days$)$ over this region. Also notice that over some frequency band for both the slope and rise stations, motions are bottom intensified. This is a definite signature of topographic Rossby waves which in the presence of stratification tend to concentrate their energy near the bottom. The more serious contamination by the surface-intensified motions on both sides of this frequency band certainly limits the application of the model there. Also, because the motions on the continental shelf are predominantly wind-driven, we will only discuss the observations on the continental slope and rise.

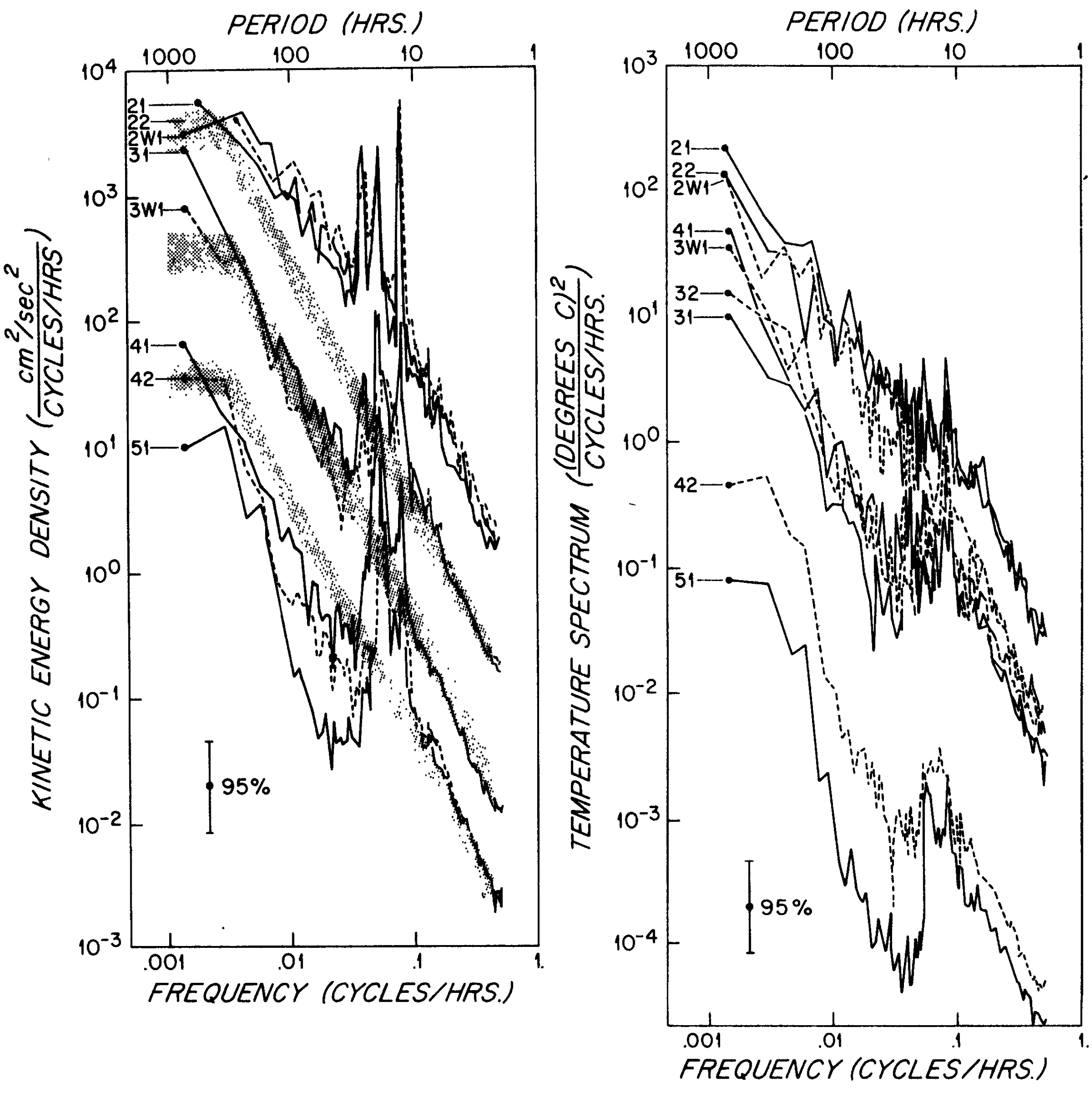

Figure 4.2. Kinetic energy and temperature spectra of NESS76. In the kinetic energy spectrum, the energy level for the shelf, slope, and rise stations have been displaced one decade apart, and the light shading with a "-2" slope for periods shorter than 14 days is to assist visual comparisons.

One of the major predictions of the model is the formation of the vertical amphidromic point near the slope-rise junction for short waves. This amphidromic point will locally reverse the direction of phase propagation above it and hence change the sign of the Reynolds stress $\overline{uv}$ and the sign of the ellipse orientation from the local isobaths. The spatial distribution of the ellipse orientation for a numerical run using the same nondimensional parameters as that used previously, but with a topography simulating that across the experimental site is shown in Fig. 4.3. The different sign of ellipse orientation above the amphidromic point is clearly shown. For a period of 10 days, this amphidromic point is formed when longshore wavelength is shorter than about 300 km, and this critical wavelength increases approximately linearly with the frequency. Since the motion is comprised of all different longshore scales, we then expect a low stability of the ellipse orientation at 41. The model also predicts that the ellipse axis will be more closely aligned with the local isobaths over the slope region. This is because increased vortex stretching tends to reduce the cross-shelf scales and hence leads to a greater longshore flow relative to the onshore flow.

The observed ellipse orientations are plotted in Fig. 4.4a-b as a function of frequency (the radius) where the x-axis is parallel with the estimated local isobaths and y-axis points onshore. Data points averaged over 6 frequency bands are indi-

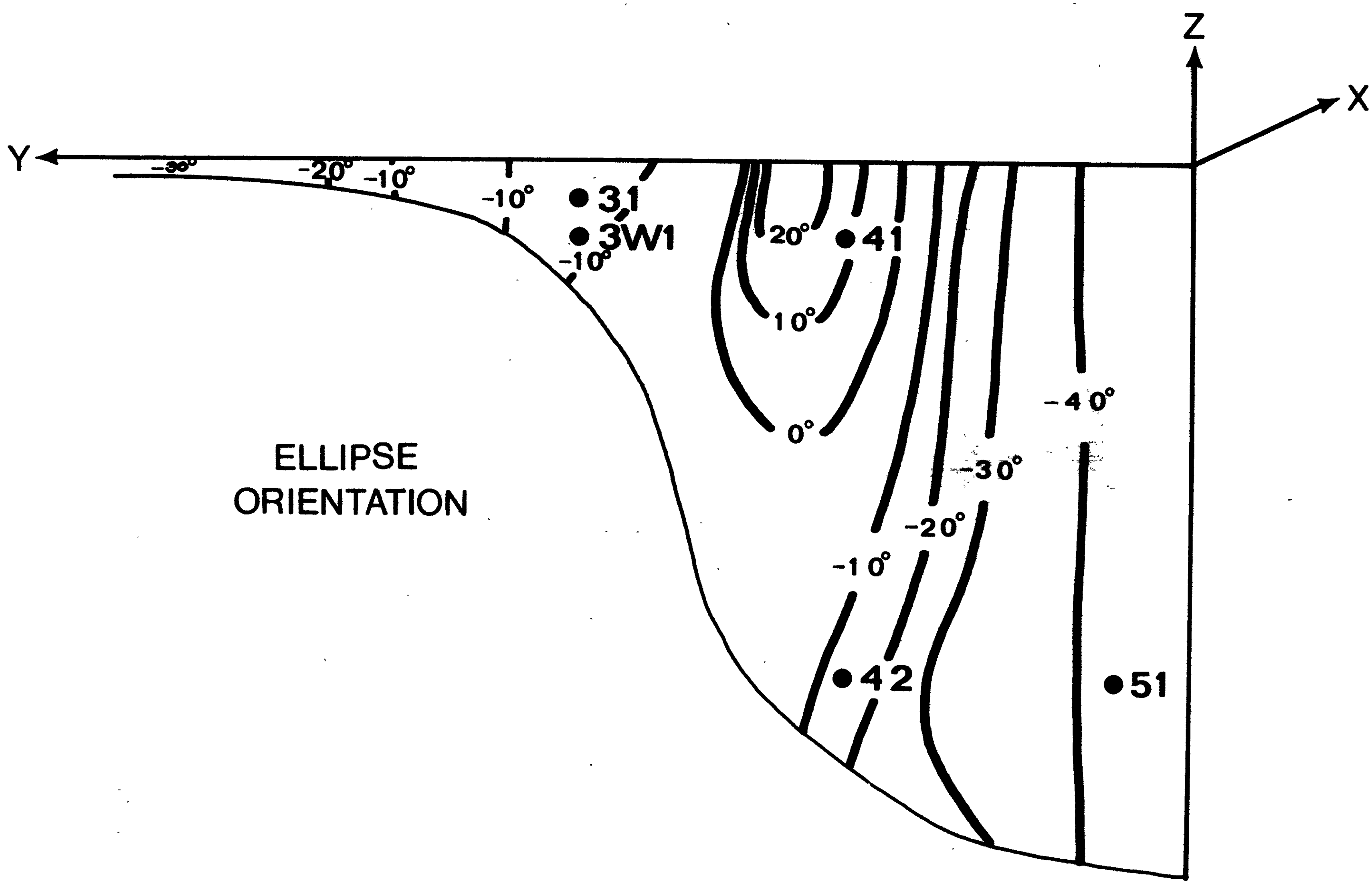

Figure 4.3. Same as Figure 3.2g, but with a topography simulating that across the New England continental margin, and ν has been set to 22 $cm^2 sec^{-1}$.

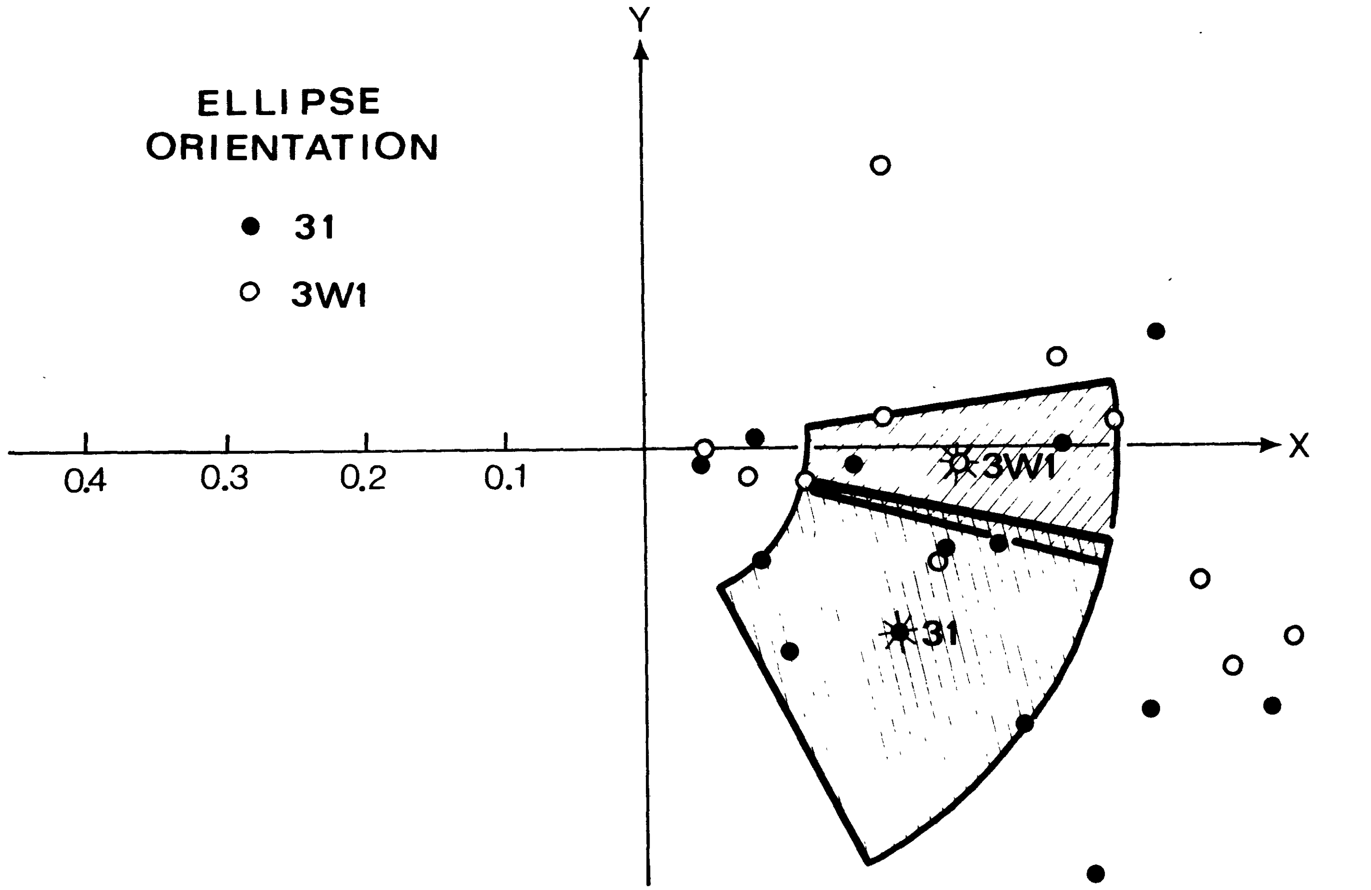

Figure 4.4a. The observed ellipse orientations as a function of frequency (the radius) at NE31 and 3W1. The x-axis is parallel with the estimated local isobaths and y-axis points onshore. Data points averaged over 6 frequency bands are indicated by the plain symbols while that averaged over 36 frequency bands are indicated by an additional "*". The shaded areas centered at the "*" represent the band width and the estimated 95% confidence limit of these data points. The shaded area is not drawn if it encompasses the whole circular band.

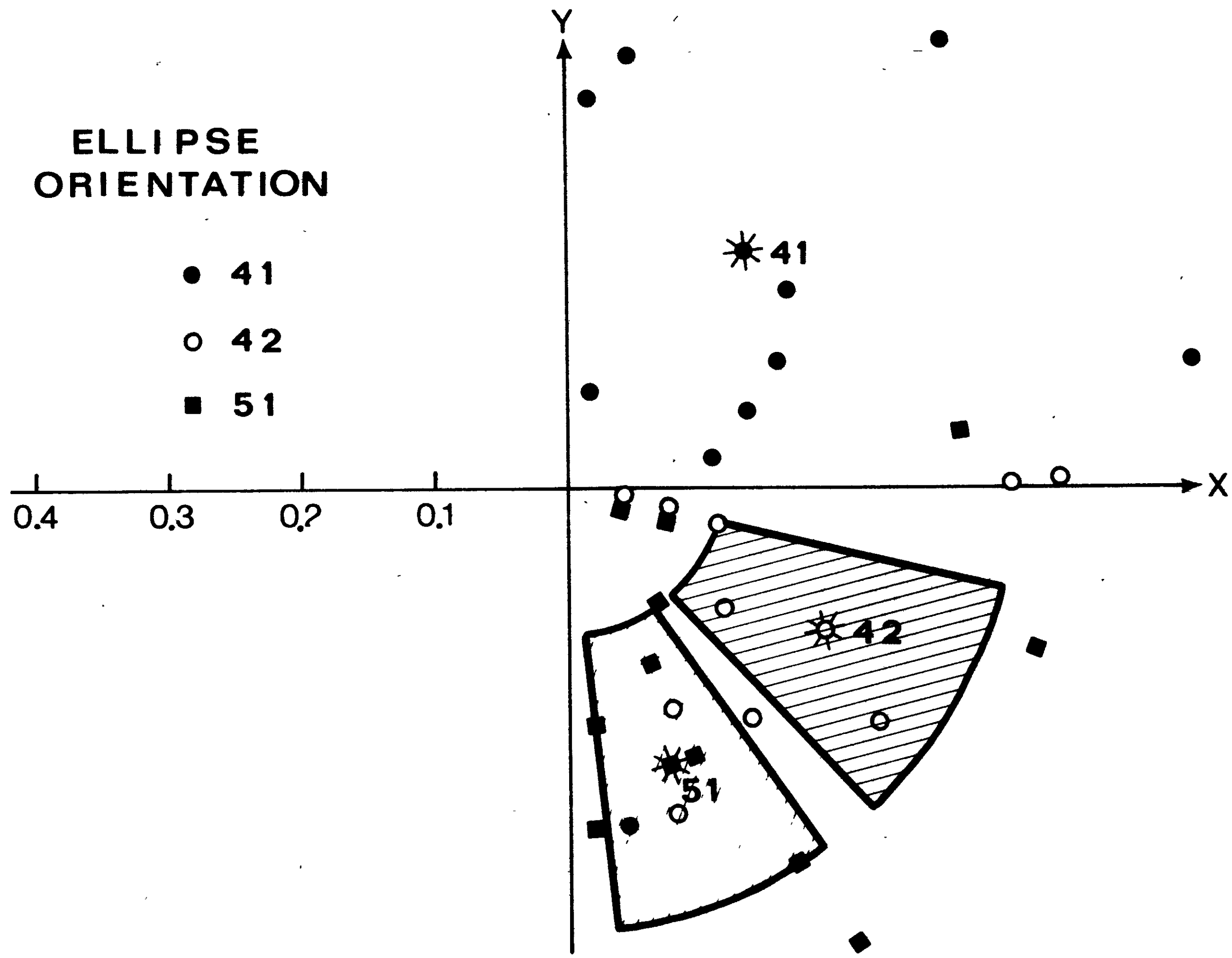

Figure 4.4b. Same as Fig. 4.4a, but for the data at NE41, 42, and 51.

cated by the plain symbols while those averaged over 36 frequency bands are indicated by an additional "*". The shaded areas centered at the "*" represent the band-width and the estimated 95% confidence limit of these data points. The shaded area is not drawn if it encompasses the whole circular band. As is expected from the above discussions, the data points at 41 behave very differently from that of the other instruments. Not only do most of the data points at 41 lie in the first quadrant instead of the fourth, but also the stability of the ellipse orientation is so low that no directionality can be inferred with statistical confidence. With this exception of 41, all the other data points averaged over 36 frequency bands lie in the fourth quadrant, consistent with the prediction of an offshore phase propagation for these incoming waves. The ellipse orientation at 51 deviates the most from the local isobaths and that at 3W1 the least, with 31 and 42 somewhere in between, again consistent with the model predictions shown in Fig. 4.3. Thompson and Luyten (1975) found that near site D, the ellipse orientation deviates more from the local isobaths toward higher frequencies which they attributed to a single propagating topographic Rossby wave. There is some indication of a similar trend here for 42 and 51, although without statistical confidence, it is by no means conclusive. Incidentally, it is interesting to notice that the data points of 42 averaged over 6 frequency bands mimic almost exactly those of 51 between periods of 3 to 10 days with a 15 to 20 degrees rotation toward the local isobaths. Whether this is of any statistical significance is not clear.

Another major prediction of the model concerns the phase lag θ_{Tv} of temperature T relative to the onshore velocity v which determines the direction of the heat flux generated by these waves. Our earlier discussions show that the quadrant in which θ_{Tv} lies depends on the relative importance of several competing mechanisms. For example, in an inviscid model, θ_{Tv} lies in the fourth quadrant over the slope region because of the effect of the rigid surface and the presence of the finite bottom slope, but over the continental rise, it lies in the third quadrant because the effect of the baroclinic fringe waves dominates. Near the slope-rise junction and above the mid-depth, it varies greatly between short and long waves, and the coherence between T and v is expected to be low. In a viscous model where an Ekman friction layer is present at the bottom, θ_{Tv} lies in the third quadrant within the dominant influence of this friction. If none of the above effects is important, θ_{Tv} is approximately -90^{o}, and the heat flux is negligible. The θ_{Tv} of the same numerical run as that of Fig. 4.3 is plotted in Fig. 4.5. From this figure, we make the following predictions.

1) At 51, θ_{Tv} is approximately -90^{o} with probably a slight veering into the third quadrant due to the influence of

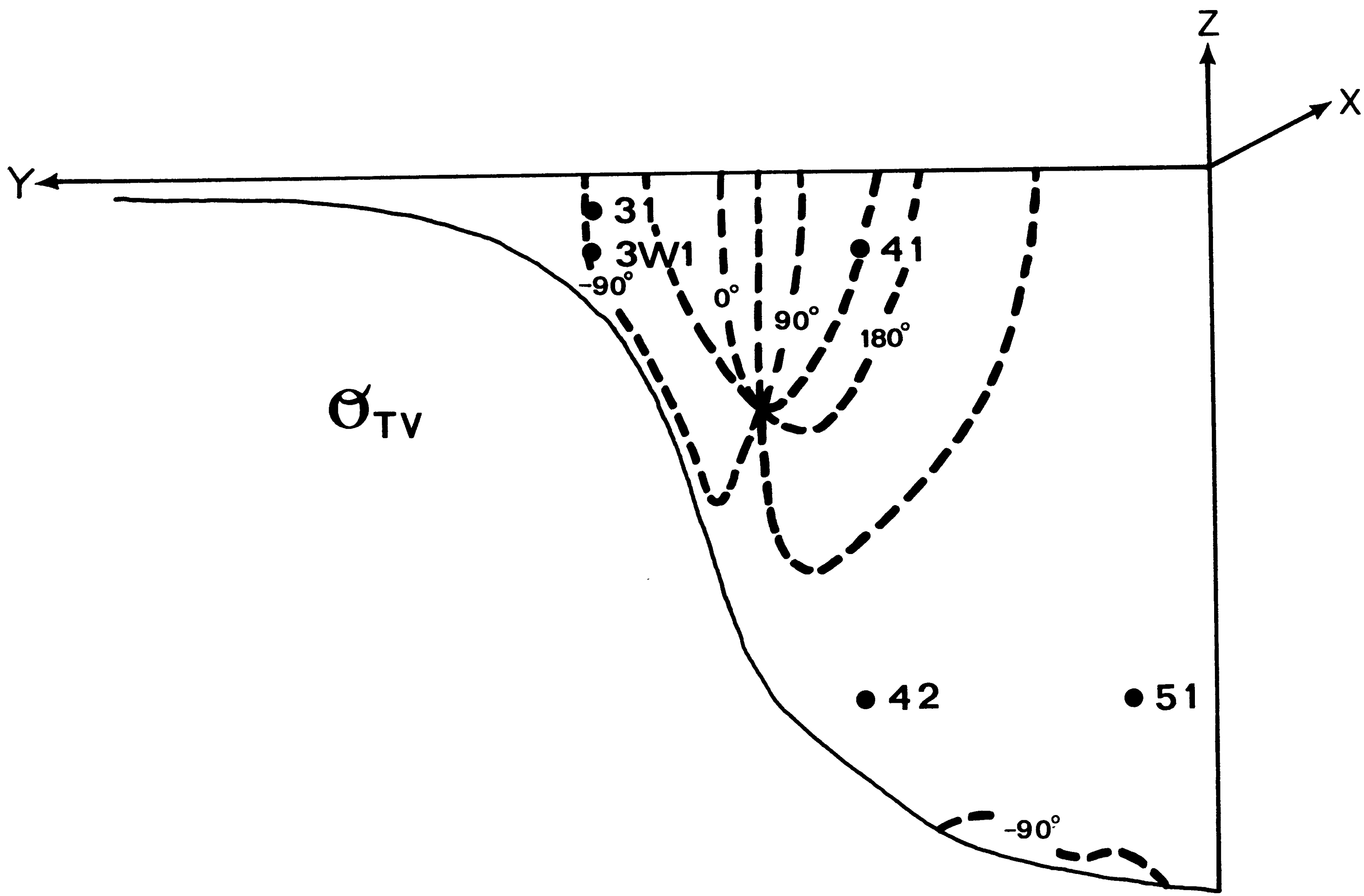

Figure 4.5. Same as Fig. 4.3 but for the phase lag θ_{TV} of temperature T relative to the onshore flow V.

both the baroclinic fringe waves and the bottom friction.

2) At 42, θ_{Tv} lies in the third quadrant because of the effect of the baroclinic fringe waves.

3) At 41, θ_{Tv} can vary greatly between short and long waves, and the coherence between T and v is expected to be low.

4) at 3W1, θ_{Tv} lies either in the third or fourth quadrant depending on whether it is dominated by the influence from the bottom friction or the rigid surface. The coherence between T and v is again expected to be low.

5) At 31, θ_{Tv} mostly lies in the fourth quadrant due to the dominant influence from the rigid surface.

The observed θ_{Tv} is plotted in Fig. 4.6a-b in a similar fashion as in Fig. 4.4. As is expected, the coherence between T and v is low at 3W1 and 41, and no preferred quadrant in which θ_{Tv} lies can be inferred with statistical confidence. Incidentally, the θ_{Tv} at these two instruments agree with the values shown in Fig. 4.5. At 31 and 42, the coherence between T and v is higher, and θ_{Tv} lies in the quadrant predicted by the model. At 51, the comparison, however, is less satisfactory. Since the heat flux at 51 is very small because of the weak temperature signal there, it is more subject to contamination by the other motions which might cause this discrepancy.

The stream function of the cross-shelf mean flow for the same numerical run is plotted in Fig. 4.7. Since the normalization factor is 1 if $|u| = 1$ at the bottom at $y = 0$ for the

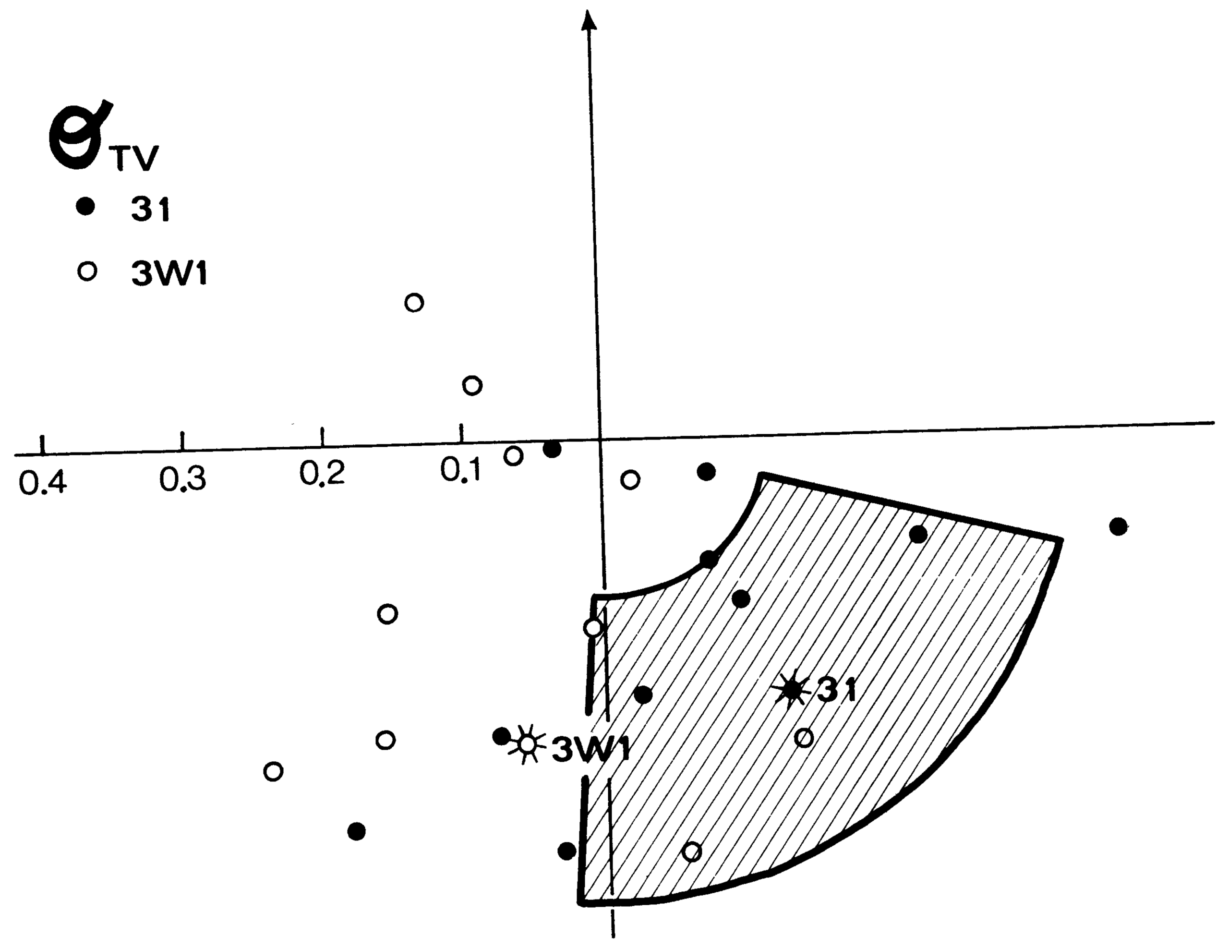

Figure 4.6a. Same as Fig. 4.4a, but for the observed θ_{TV}. The axis has no geometrical meaning.

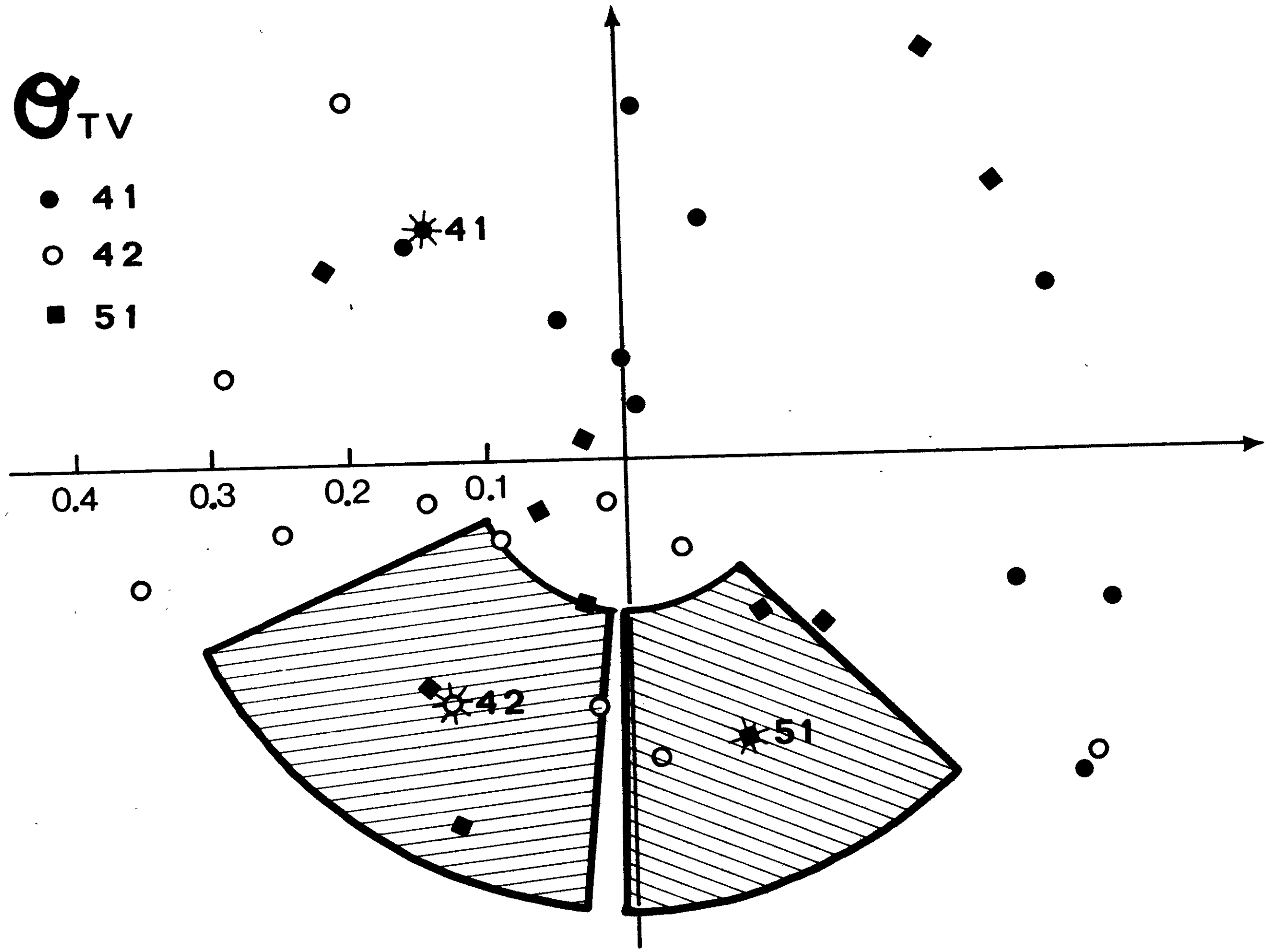

Figure 4.6b. Same as Fig. 4.6a, but for the data at NE41, 42, and 51.

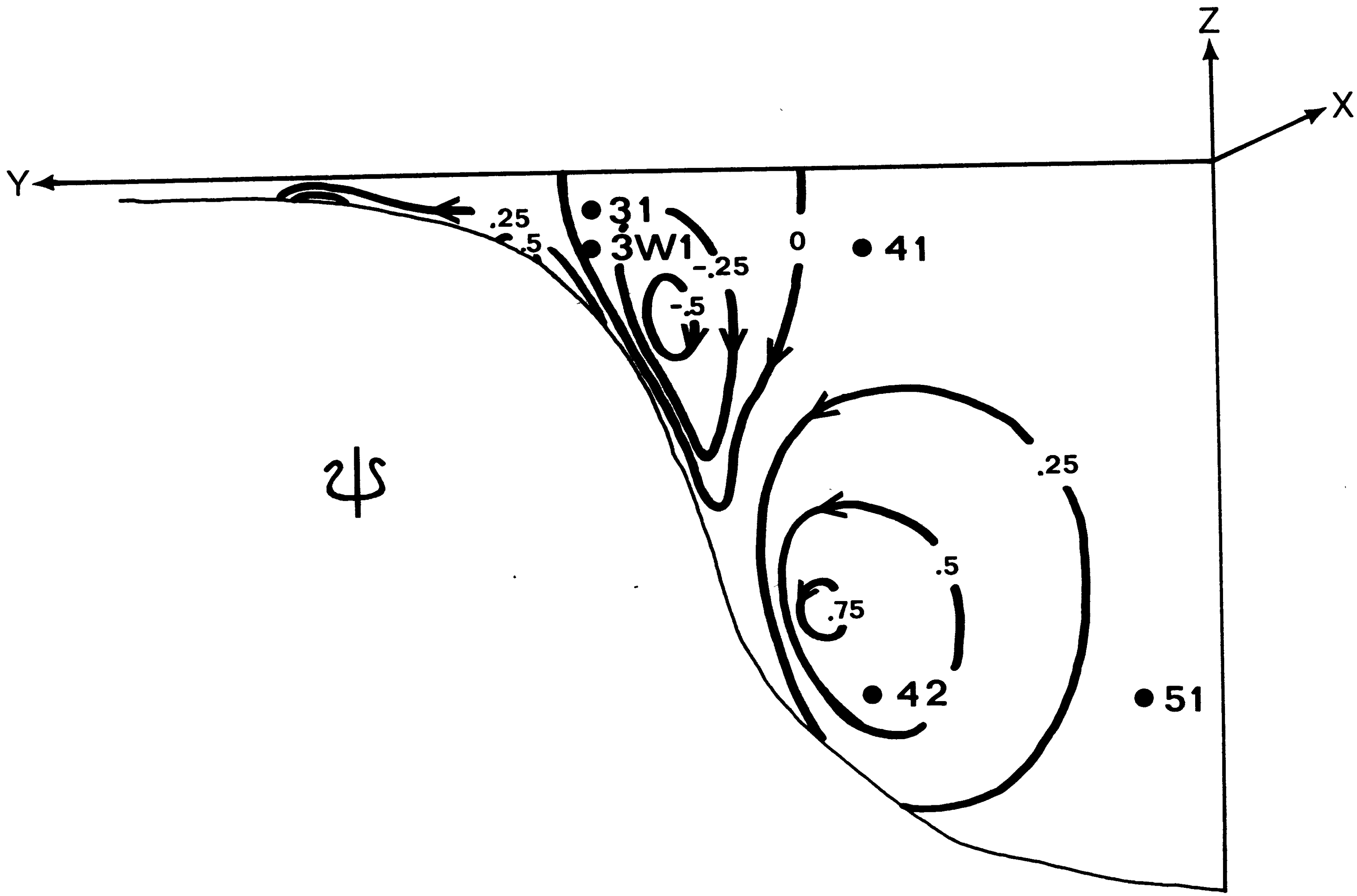

Figure 4.7. Same as Fig. 4.3, but for the stream function of the cross-shelf mean flow. The magnitude has been normalized so that $|u| = 1$ at the bottom at $y = 0$ for the incoming wave.

incoming wave, in the dimensional unit,

$$(\overline{v}^*, \overline{w}^*) \sim (\overline{v}, \tfrac{H}{L}\overline{w}) \cdot \epsilon V$$
$$\sim (-\overline{\psi}_z, \tfrac{H}{L}\overline{\psi}_y) \cdot \epsilon V,$$

where ϵ is the Rossby number, and V is the longshore velocity scale. For motions of a period between 3 and 10 days, the velocity fluctuation is typically of the order 1 cm/sec at 51. With L = 45 km, f = .94 x 10^{-4} $\sec^{-1}$, ϵ is then approximately 2.4 x 10^{-3}, and hence

$$\epsilon V \sim 2.4 \times 10^{-3} \text{ cm/sec.}$$

From the figure, $(\overline{v},\overline{w}) \lesssim O(10)$, therefore,

$$\overline{v}^* \lesssim 2.4 \times 10^{-2} \text{ cm/sec,}$$
$$\overline{w}^* \lesssim 1.4 \times 10^{-3} \text{ cm/sec (with H = 2.7 km),}$$

which are too small to be significant.

The longshore mean flow is plotted in Fig. 4.8. Since the normalization factor is 33 if $|u| = 1$ at the bottom at $y = 0$ for the incoming wave, in the dimensional unit,

$$\overline{u}^* \sim \overline{u} \cdot \epsilon V \cdot (33)$$
$$\sim (0.08\ \overline{u}) \text{ cm/sec.}$$

The maximum value of $\overline{u}$ is about 10 from the figure, hence $\overline{u}^*$ has a maximum of about .8 cm/sec and is located near the shelf break. Since this magnitude is comparable to the fluctuation velocities, our theory breaks down.

The observed mean flow is shown by the arrows in Fig. 4.9, where the rectangles centered at the end of the arrows indicate the estimated 95% confidence limit. Dashed arrows are for

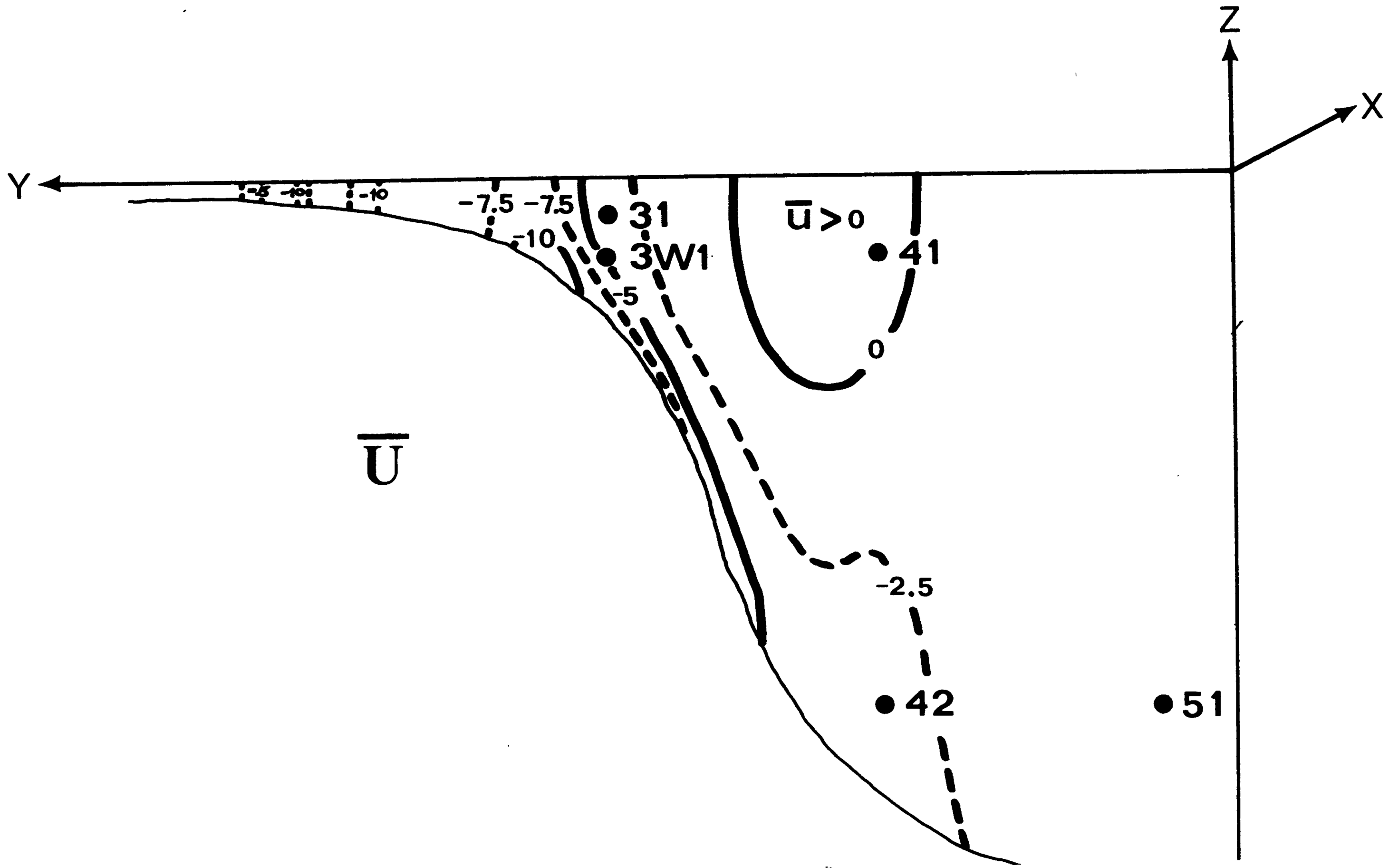

Figure 4.8. Same as Fig. 4.3, but for the longshore mean flow. $|\vec{u}|$ has been normalized to 1 at the bottom at $y = 0$ for the incoming wave. The normalization factor is 33 if $|u| = 1$ at the bottom at $y = 0$ for the incoming wave.

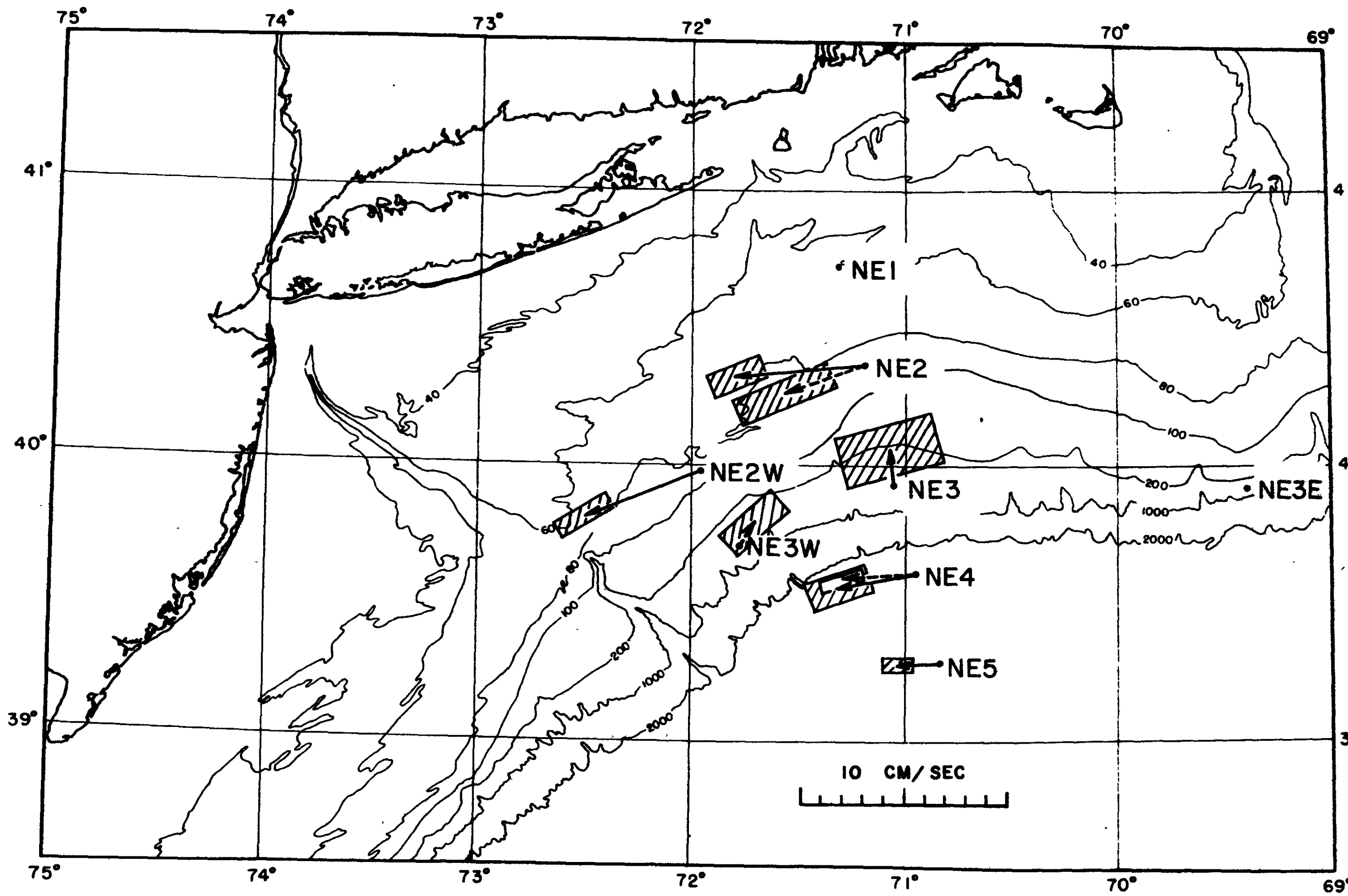

Figure 4.9. The observed mean flow of NESS76, where the rectangles centered at the end of the arrows indicate the 95% confidence limit. Dashed arrows are for deeper instruments.

deeper instruments. Although the westward mean flow observed at NE4 and NE5 is consistent with the model predictions, the magnitude of this mean flow is by no means smaller than the low frequency fluctuations which have magnitudes of a few cm/sec at most, hence it cannot be explained by the theory presented here.

4.2 Discussion

Despite the simplification of the model, the two major predictions that are the least scale-dependent compare reasonably well with the observations of NESS76. These comparisons can be made more conclusive if we have data near the bottom over the slope region that shows an offshore heat flux. The prediction of the formation of an amphidromic point near slope-rise junction for short waves can also be tested more critically if we have several instruments located at 41 but are displaced alongshore. Since the model predicts that the bottom trapping is intensified at lower frequencies, the amphidromic point can therefore be formed even for longer waves. By filtering out consecutively longer waves at lower frequency bands we can probably test this prediction.

From the comparisons made so far, it is suggestive that Thompson's conclusion about the dominance of linear topographic Rossby wave dynamics over the continental rise also holds over the continental slope for motions of the period between 3 and 10 days. The application of the model to the lower frequency bands is limited by the increased importance of baroclinic eddies which also become increasingly nonlinear. Toward the higher frequency bands, the contamination by the surface intensified motions can no loger be neglected. The uniqueness of our explanations of some observed features can be better established only after we have also examined these other motions.

Although the numerical solutions have been presented only for the case of a uniformly stratified ocean, this is not a limitation of the model. The effect of a slightly varied stratification in the vertical direction is not expected to change the qualitative results reported here and hence is not pursued in any length. Since at the present stage, a more detailed comparison with the model is mostly prevented from our inability to isolate the motions of different longshore scales, a more complicated model which takes into account the presence of mean flow, the shelf-slope front, etc., might be difficult to verify.

It is, of course, a different story in the laboratory where the longshore wavelength can be given by the wave maker, and the model predictions can be tested much more critically for its consistencies. In particular, the mean flow predicted by the theory assuming a weak interaction can also be tested. This is, however, a long-term project and should be left for the future.

REFERENCES

Friedrichs, K. O. (1948) Water waves on a shallow sloping beach. Communications on Pure and Applied Mathematics, 1, 109-134.

Kroll, J. and Niiler, P. P. (1976) The transmission and decay of barotropic topographic Rossby waves incident on a continental shelf. J. of Phys. Oceanogr., 6, 432-450.

Lindzen, R. S. and Kuo, H. L. (1969) A reliable method for the numerical integration of a large class of ordinary and partial differential equations. Mon. Wea. Rev., 96, 732-734.

McIntyre, M. E. (1977) Wave transport in stratified, rotating fluids. Lecture notes in Phys., 71, 290-314. Springer--Verleg.

Ou, H. W. and Bennett, J. R. (1979) A theory of the mean flow driven by long internal waves in a rotating basin, with application to Lake Kinneret. To appear in J. Phys. Oceanogr.

Pedlosky, J. (1974) Longshore currents, upwelling, and topography. J. Phys. Oceanogr., 4, 214-226.

Peters, A. S. (1952) Water waves over sloping beaches and the solution of a mixed boundary value problem for $-k^2 = 0$ in a sector. Communications on Pure and Applied Mathematics, 5, 87-108.

Reid, R. O. (1958) Effect of Coriolis force on edge waves, (1) investigation of the normal modes. J. of Mar. Res., 16, 109-144.

Rhines, P. B. (1969) Slow oscillations in an ocean of varying depth, Part 1, abrupt topography. J. Fluid Mech., 37, 161-189.

Rhines, P. B. (1970) Edge-, bottom-, and Rossby waves in a rotating stratified fluid. Geophys. Fluid Dyn., 1, 273-302.

Rhines, P. B. (1971) A note on long period motions at site D. Deep-Sea Res. 18, 21-26.

Smith, R. (1971) The ray paths of topographic Rossby waves. Deep-Sea Res., 18, 477-483.

Stoker, J. J. (1957) Water Waves. Interscience Publishers, Inc., New York. 567 pp.

Stokes, G. G. (1846) Rep. Brit. Ass., Part 1, p. 1; also Mathematical and Physical papers, 1, Cambridge Univ. Press, 167-168 (1880).

Suarez, A. A. (1971) The propagation and generation of topographic oscillations in the ocean. Ph.D. thesis, MIT-WHOI Earth Sciences. 130 pp.

Thompson, R. O. R. Y. (1971) Topographic Rossby waves at a site north of the Gulf Stream. Deep-Sea Res., 18, 1-19.

Thompson, R. O. R. Y. and Luyten, J. R. (1976) Evidence for bottom-trapped topographic Rossby waves from single moorings. Deep-Sea Res., 23, 629-635.

Thompson, R. O. R. Y. (1977) Observations of Rossby waves near Site D. Prog. Oceanog., 7, 1-28.

Ursell, F. (1952) Edge waves on a sloping beach. Proc. Roy. Soc., (A) 214, 79-97.

Wang, D. P. (1975) Coastal water response to the variable wind-theory and coastal upwelling experiment. Ph.D. thesis, University of Miami, 174 pp.

Wang, D. P. and Mooers, C. N. K. (1976) Coastal-trapped waves in a continuously stratified ocean. J. of Phys. Oceanogr., 6, 853-863.

APPENDIX A

REDUCTION OF THE ANALYTICAL SOLUTION

The analytical solution (2.17) can be simplified when $\omega = \pi/2n$ where n is an integer, as is derived in the following.

Peters (1952) has shown that with $h(\zeta)$ defined by

$$h(\zeta) = \frac{\zeta}{\zeta + ir}\, g(\zeta, r), \tag{A.1}$$

where $g(\zeta, r)$ is given by (2.18), then $I(\zeta) \equiv \ln h(\zeta)$ satisfies

$$I(\zeta e^{i\omega}, r) = -\frac{1}{\pi}\int_0^{\infty} \frac{\zeta}{v^2+\zeta^2} \ln\left[1+\left(\frac{r}{v}\right)^{2n}\right] dv$$

$$\text{for } -\frac{\pi}{2} < \arg \zeta < \frac{\pi}{2}. \tag{A.2}$$

Now, let $\omega = \pi/2n$, (A.2) becomes

$$I(\zeta e^{i\pi/2n}, r) = -\frac{1}{2\pi}\int_{-\infty}^{\infty} \frac{\zeta}{v^2+\zeta^2} \ln\left[1+\left(\frac{r}{v}\right)^{2n}\right] dv$$

$$= -\frac{1}{2\pi i}\int_{-\infty}^{\infty} \frac{1}{v - i\zeta} \ln\left[1+\left(\frac{r}{v}\right)^{2n}\right] dv$$

$$= -\frac{n}{\pi i}\int_{-\infty}^{\infty} \frac{\ln(v - i\zeta)}{v\left[1+\left(\frac{v}{r}\right)^{2n}\right]} dv \quad \text{(integration by parts)}$$

$$= -\frac{n}{\pi i}\int_{-\infty}^{\infty} \frac{\ln(ru - i\zeta)}{u(1+u^{2n})} \cdot du \quad (u \equiv v/r)$$

$$= n \ln(-i\zeta) + 2n \ast \sum_{k=1}^{n} \frac{\ln(r u_k - i\zeta)}{u_k \cdot \prod_{\substack{k'=1 \\ k' \neq k}}^{2n} (u_k - u_{k'})}, \quad \text{(residue theorem)} \tag{A.3}$$

where

$$u_k = e^{-\frac{i\pi}{2n}(2k-1)}, \qquad k = 1, \cdots, 2n.$$

Since

$$u_k \prod_{\substack{k'=1 \\ k' \neq k}}^{2n} (u_k - u_{k'}) = e^{-\frac{i\pi}{2n}(2k-1)} \prod_{\substack{k'=1 \\ k' \neq k}}^{2n} \left[e^{-\frac{i\pi}{2n}(2k-1)} - e^{-\frac{i\pi}{2n}(2k'-1)}\right]$$

$$= 2e^{-i\pi(2k-1)} \prod_{k'=1}^{n-1} \left(1 - e^{\frac{i\pi}{n}k'}\right)\left(1 - e^{-\frac{i\pi}{n}k'}\right)$$

$$= -8 \prod_{k'=1}^{n-1} \sin^2\left(\frac{\pi}{2n}k'\right)$$

$$= -2n,$$

(A.3) then implies

$$I(\xi e^{i\pi/2n}, r) = n \ln(-i\xi) - \sum_{k=1}^{n} \ln(r u_k - i\xi), \tag{A.4}$$

or

$$I(\xi, r) = \ln \frac{\xi^{n} e^{-i\frac{\pi}{2}(1+n)}}{\prod_{k=1}^{n}\left[r u_k + \xi e^{-i\frac{\pi}{2}(1+1/n)}\right]}, \tag{A.5}$$

or

$$\frac{g(\xi, r)}{\xi + ir} = \frac{\xi^{n-1} e^{-i\frac{\pi}{2}(1+n)}}{\prod_{k=1}^{n}\left[r u_k + \xi e^{-i\frac{\pi}{2}(1+\frac{1}{n})}\right]}$$

$$= \frac{\xi^{n-1}}{\prod_{k=1}^{n}(\xi - r\xi_k)}, \tag{A.6}$$

where

$$\xi_k = e^{i\pi\left(\frac{1}{2}+\frac{k}{n}\right)}.$$

Substituting (A.6) into (2.17), we finally obtain,

$$\chi_s = (i)^s \oint_{\Gamma_s} \frac{\xi^{2n-1} \exp\left(\tau\xi + \tau_1\tau_2\bar{\tau}/\xi\right) d\xi}{\prod_{k=1}^{n}(\xi - \tau_1\xi_k)(\xi - \tau_2\xi_k)}, \tag{A.7}$$

the evaluation of which can be considerably simplified because of the presence of simple poles of the integrand. Employing residue theorem, χ_1 can be further reduced to a summation of its residues while χ_2 still involves the contour integration which can be numerically integrated.

APPENDIX B

ASYMPTOTIC SOLUTION FOR SMALL S IN A WEDGE

As the derivation below follows very closely that of Friedrichs' (1952), we will only write down some key results and the corresponding equation number in the Friedrichs' paper (preceded by a capital F).

Let's define,

$$\chi_{\pm} = \int_{\Gamma_{\pm}} \frac{\zeta^{2n-1} e^{\eta\zeta + \tau_1\tau_2\bar{\eta}/\zeta}\, d\zeta}{\prod_{k=1}^{n} (\zeta - \tau_1 \zeta_k)(\zeta - \tau_2 \zeta_k)}, \qquad \text{(B.1),(F.3)}$$

where all the notations have been defined in (2.19) and Appendix A, then $\chi_{1,2}$ of (A.7) are simply given by,

$$\chi_1 = i(\chi_+ - \chi_-),$$
$$\chi_2 = \chi_+ + \chi_- . \qquad \text{(B.2),(F.8)}$$

In the limit, $n \to \infty$, (B.1) becomes,

$$\chi_{\pm} \sim -\int_{\Gamma_{\pm}} \zeta^{-1} (\tau_1\tau_2)^{-n} \left[\frac{\frac{1}{\zeta} + \frac{i}{\tau_1}}{\frac{1}{\zeta} - \frac{i}{\tau_1}} \cdot \frac{\frac{1}{\zeta} + \frac{i}{\tau_2}}{\frac{1}{\zeta} - \frac{i}{\tau_2}} \right]^{1/2} *$$

$$\exp\left[\eta\zeta + \tau_1\tau_2\bar{\eta}/\zeta - t_0 \cdot \left(H(\zeta,\tau_1) + H(\zeta,\tau_2)\right)\right] d\zeta, \qquad \text{(B.3),(F.22)}$$

where

$$H(\zeta,\tau) = \int_0^{1/\zeta} \tan^{-1}(\mu\tau) \frac{d\mu}{\mu} - \frac{\pi}{2} \ln \tau. \qquad \text{(B.4),(F.26)}$$

The saddle point $\tilde{\zeta}$ is given by,

$$\omega y' = \frac{1}{1-\tau_1\tau_2/\xi^2}\cdot\left[H'(\xi,\tau_1)+H'(\xi,\tau_2)\right], \qquad \text{(B.5), (F.44)}$$

or by setting $\tilde{\xi} \equiv i\lambda^{-1}$,

$$\omega y' = \frac{\lambda}{A}\left[\tanh^{-1}\lambda\tau_1 + \tanh^{-1}\lambda\tau_2\right], \qquad \text{(B.6), (F.46)}$$

where

$$A = 1 + \tau_1\tau_2\lambda^2, \qquad \text{(B.7)}$$

$$B = 1 - \tau_1\tau_2\lambda^2. \qquad \text{(B.8)}$$

The solution (B.3) can then be approximated by,

$$\chi_\pm \sim (\tau_1\tau_2)^{-n}\left(\frac{1}{\tau_1}\mp\lambda\right)\left(\frac{\frac{1}{\tau_2}\mp\lambda}{\frac{1}{\tau_2}\pm\lambda}\right)^{1/2}\cdot\left(\frac{2\pi\omega}{j(\lambda)}\right)^{1/2} *$$

$$\exp\left(\pm i\omega^{-1}K(\lambda) \pm i\pi/4\right), \qquad \text{(B.9), (F.52)}$$

where

$$j(\lambda) = \left(\frac{1}{\tau_1^2}-\lambda^2\right)\lambda K'(\lambda)\cdot\frac{A}{B}, \qquad \text{(B.10), (F.49)}$$

$$K(\lambda) = \frac{B}{A}\left(\tanh^{-1}\lambda\tau_1 + \tanh^{-1}\lambda\tau_2\right) + \int_0^{\lambda\tau_1}\tanh^{-1}u\cdot\frac{du}{u}$$

$$+\int_0^{\lambda\tau_2}\tanh^{-1}u\cdot\frac{du}{u} - \frac{\pi}{2}\ln\tau_1\tau_2. \qquad \text{(B.11), (F.48)}$$

In the far field, where $\omega y' \gg 1$, (B.9) becomes

$$\chi_+ \sim (\tau_1\tau_2)^{-n}\cdot 2\exp(-2C\omega y')(1-k^2)^{1/4}\cdot(2\pi\omega)^{1/2} *$$

$$\exp\left[i\left(\sqrt{1-k^2}\,y' + \omega^{-1}D + \pi/4\right)\right], \qquad \text{(B.12), (F.67)}$$

$$\chi_- \sim (\tau_1\tau_2)^{-n}\cdot 2\,(1-k^2)^{1/4}\cdot(2\pi\omega)^{1/2} *$$

$$\exp\left[-i\left(\sqrt{1-k^2}\,y' + \omega^{-1}D + \pi/4\right)\right], \qquad \text{(B.13), (F.68)}$$

where

$$C = \tau_1 + \tau_2,$$

$$D = \left(\frac{\tau_1-\tau_2}{\tau_1+\tau_2} + \frac{\tau_2^2-\tau_1^2}{2\tau_1^2}\right)\tan^{-1}\frac{\tau_2}{\tau_1} + \frac{\tau_2}{2\tau_1} - \frac{\pi}{2}\ln(\tau_1\tau_2).$$

Accordingly, (B.2) implies,

$$\chi_{1,2} \sim \mp 2(\tau_1\tau_2)^{-\pi}(1-k'^2)^{1/4}(2\pi\omega)^{1/2} *$$
$$\exp\left(-i\omega^{-1}D \pm i\pi/4\right)\cdot\exp\left(-i\sqrt{1-k'^2}\,y'\right). \qquad \text{(B.14),(F.69)}$$

The two solutions are sinusoidal and differ in phase by 90°.

We define the "local" cross-wedge wavelength as

$$\Lambda' = 2\pi\left(\frac{d}{dy'}\,\omega^{-1}K(\lambda)\right)^{-1} \qquad \text{(B.15),(F.31)}$$
$$= 2\pi\lambda/B, \qquad \text{(B.16),(F.32)}$$

then the local cross-wedge wave number is given by

$$\ell' = 2\pi/\Lambda'$$
$$= B/\lambda. \qquad \text{(B.17)}$$

The "local" amplitude can also be derived

$$A_m(\lambda) = \left[\left(\frac{1}{\tau_1}-\lambda\right)\left(\frac{\frac{1}{\tau_2}-\lambda}{\frac{1}{\tau_2}+\lambda}\right)^{1/2} + \left(\frac{1}{\tau_1}+\lambda\right)\left(\frac{\frac{1}{\tau_2}+\lambda}{\frac{1}{\tau_2}-\lambda}\right)^{1/2}\right] *$$
$$\left(\frac{2\pi\omega}{j(\lambda)}\right)^{1/2}. \qquad \text{(B.18),(F.12)}$$

From (B.14), we can then derive that

$$R_\Lambda \equiv \Lambda/\Lambda]_\infty$$
$$= \frac{\lambda\sqrt{1-k'^2}}{1-k'^2\lambda^2}, \qquad \text{(B.19)}$$

$$R_A \equiv A_m/A_m]_\infty$$
$$= \frac{(1-k'^2)^{1/4}}{2}\cdot\frac{\left(\frac{1}{\tau_1}-\lambda\right)\sqrt{\frac{\frac{1}{\tau_2}-\lambda}{\frac{1}{\tau_2}+\lambda}} + \left(\frac{1}{\tau_1}+\lambda\right)\sqrt{\frac{\frac{1}{\tau_2}+\lambda}{\frac{1}{\tau_2}-\lambda}}}{\sqrt{j(\lambda)}}. \qquad \text{(B.20)}$$

APPENDIX C

A THEORY OF MEAN FLOW GENERATION

Let the x, y and z-axis be oriented as in Fig. 2.1, and assume that all the nondimensional variables can be expanded in terms of the small Rossby number ε as,

$$p^* = p + \varepsilon \bar{p} + O(\varepsilon^2), \qquad \text{etc.,}$$

where p is the variable associated with the primary waves and $\bar{p}$ is the secondary mean field induced by these waves. With a similar scaling as that of (2.3), the non-dimensionalized governing equations for the O(1) fields are given by

$$\begin{aligned}
u_t - v &= - p_x - \alpha u, \\
v_t + u &= - p_y - \alpha v, \\
0 &= - p_z - \rho, \\
\rho_t - S^2 w &= 0, \\
u_x + v_y + w_z &= 0,
\end{aligned} \qquad (C.1)$$

and for the $O(\varepsilon)$ fields, given by

$$\begin{aligned}
\alpha \bar{u} - \bar{v} &= - \partial_y \overline{uv} - \partial_z \overline{uw}, \\
\alpha \bar{v} + \bar{u} &= - \bar{p}_y - \partial_y \overline{v^2} - \partial_z \overline{vw}, \\
0 &= - \bar{p}_z - \bar{\rho}, \\
- S^2 \bar{w} &= - \partial_y \overline{v\rho} - \partial_z \overline{w\rho}, \\
\bar{v}_y + \bar{w}_z &= 0,
\end{aligned} \qquad (C.2)$$

where a linear friction law with a small dimensionless friction coefficient α has been assumed. The introduction of some form of a friction is essential to the study of the mean flow in the equilibrium state (Ou and Bennett, 1979). The linear friction law is chosen here for simplicity.

Since the mean flow is non-divergent in the y-z plane, a stream function ψ can be defined,

$$(\bar{v},\bar{w}) = (-\psi_z, \psi_y). \tag{C.3}$$

As w and ρ are in quadrature from (C.1), the mean heat balance reduces to

$$\bar{w} = \frac{1}{S^2}\partial_y \overline{v\rho}, \tag{C.4}$$

which combined with (C.3), implies that

$$\psi = \frac{1}{S^2}\overline{v\rho}. \tag{C.5}$$

That is, required by the assumed heat balance and incompressibility, the mean flow in the y-z plane follows the contours of the constant heat flux. A similar result for a more general case has been derived by McIntyre (1977).

Assuming a solution of the form,

$$p \sim e^{i(kx-\sigma t)},$$

for the primary waves, we can derive that

$$\begin{aligned}
\alpha\bar{u} &= -\partial_y\overline{uv} - \partial_z\overline{uw} + \bar{v} && \text{(from (C.2))}\\
&= -\partial_y\overline{uv} - \partial_z\overline{uw} - \frac{1}{S^2}\partial_z\overline{v\rho} && \text{(from (C.3) and (C.5))}\\
&= -\partial_y\overline{uv} - \partial_z\overline{(u - iv/\sigma)\cdot w} && \text{(from (C.1))}\\
&= -\partial_y\overline{uv} - \partial_z\overline{(\tfrac{k}{\sigma}p - i\tfrac{\alpha}{\sigma}u)\cdot w} && \text{(from (C.1))}\\
&= -\partial_y\overline{uv} + \frac{k}{\sigma}\left[\partial_y\overline{pv} + \alpha\overline{(u^2+v^2)}\right]\\
&\quad + \frac{\alpha}{\sigma}\partial_z\overline{iu\cdot w} && \text{(from energy equation}\\
& && \text{derived from (C.1))}\\
&= \frac{\alpha}{\sigma}\left[\partial_y\overline{iu\cdot v} + \partial_z\overline{iu\cdot w} + k\overline{(u^2+v^2)}\right] && \text{(from (C.1))}\\
&= \frac{\alpha}{\sigma}\left[\overline{iu_y\cdot v} + \overline{iu_z\cdot w} + k\overline{v^2}\right], && \text{(from (C.1))}
\end{aligned}$$

or

$$\overline{u} = \frac{1}{\sigma}\left[\overline{i u_y v} + \overline{i u_z \cdot w} + \overline{k v^2}\right]. \qquad (C.6)$$

For small α, to a first order approximation, the right hand side of (C.6) can be calculated as if the waves are inviscid, and hence $\overline{u}$ does not depend on α.

An equation similar to the thermal wind relation can be easily derived,

$$\overline{\rho}_y = \partial_z(\overline{u} - F^y), \qquad (C.7)$$

where

$$F^y = -\partial_y \overline{v^2} - \partial_z \overline{vw}.$$

APPENDIX D

THE NUMERICAL MODEL

The numerical model is similar to that of Wang (1975), and the readers are referred to Wang for some of the details

The nondimensionalized governing equation in our coordinate system is given by,

$$P_{yy} - k^2 P + \frac{1-\sigma^2}{\delta^2} P_{zz} = 0, \qquad \text{(D.1)}$$

where

$$\delta \equiv \frac{N}{f} \cdot \frac{H}{L},$$

and the boundary conditions at the surface and the bottom are

$$P_z = 0 \quad \text{at } z = 0, \qquad \text{(D.2)}$$

and

$$P_z = -\frac{\delta^2}{1-\sigma^2} h_y \left(P_y - \frac{k}{\sigma} P\right) - \frac{i\delta^2}{2\sigma(1-\sigma^2)} E^{1/2} \nabla^2 P \quad \text{at } z = -h(y). \qquad \text{(D.3)}$$

As in Wang, we first map the domain of the variable bottom into one of a rectangle through the following transformation

$$(y, z) \rightarrow (y, \theta(y, z)), \qquad \text{(D.4)}$$

where

$$\theta \equiv -z / h(y), \qquad \text{(D.5)}$$

then θ spans the range between 0 and 1.

Let this rectangle be approximated by M x N uniformly spaced grid points, and i, j be the indeces of these grid points along the y and θ axis, respectively. The finite differenced appoximation of the transformed equations (D.1) through (D.3) can be written in a matrix form as

$$\mathbf{A}_i \vec{P}_{i-1} + \mathbf{B}_i \vec{P}_i + \mathbf{C}_i \vec{P}_{i+1} = \vec{D}_i, \tag{D.6}$$

where, according to the convention adopted from here on, all the bold letters represent matrices and the letters with an arrow on the top represent column vectors. In the above expression, $\vec{P}_i$ is a column vector composed of values of P_{ij} with j varies from 1 to N+1, and the expressions for $\mathbf{A}_i, \mathbf{B}_i, \mathbf{C}_i, \vec{D}_i$ can be trivially derived. The image points at j=N+1 are included for a easier implementation of the bottom boundary condition.

At the horizontal boundaries, the radiation conditions (3.2) through (3.5) can be written in a matrix form as

$$\vec{P}_1 = \mathbf{B}(\vec{I} + \vec{R}), \text{ etc.,} \tag{D.7}$$

where

$$\begin{aligned} \vec{I} &= [I_1, \cdots, I_N, 0]^T \\ \vec{R} &= [R_1, \cdots, R_N, P_{1,N+1}]^T \\ \vec{T} &= [T_1, \cdots, T_N, P_{M,N+1}]^T. \end{aligned} \tag{D.8}$$

Substituting (D.7) into (D.6), we obtain expressions at the end points as

$$\mathbf{A}_1' \vec{R} + \mathbf{B}_1' \vec{P}_2 = \vec{D}_1', \text{ etc.,} \tag{D.9}$$

where $\vec{R}$ and $\vec{T}$ now replace $\vec{P}_1$ and $\vec{P}_M$ as the unknowns. An extended version of Gaussian elimination (Lindzen and Kuo, 1969) can be used to solve (D.6) and (D.9), and $\vec{P}_1$, $\vec{P}_M$ can be retrieved later from (D.7).

BIOGRAPHICAL NOTE

Hsien Wang Ou was born in Taiwan in September, 1949. After graduating from the National Tsing Hua University in 1971 with a B.S. degree in physics, he served two years in the army in the air defense unit. Pursuing an interest in the field of oceanography, he went subsequently to the Florida State University in 1973 and received a M.S. degree in physical oceanography in 1975. He was then admitted to the Massachusetts Institute of Technology, Woods Hole Oceanographic Institution Joint Program in Oceanography.

Publications:

Hsueh, Y. and Ou, H. W. (1975) On the possibilities of coastal, mid-shelf, and shelf break upwelling. J. Phys. Oceanogr., 5, 670-682.

Ou, H. W. and Bennett, J. R. (1979) A theory of the mean flow driven by long internal waves in a rotating basin, with application to Lake Kinneret. To appear in J. Phys. Oceanogr.